

BOSTON UNIVERSITY  
GRADUATE SCHOOL OF ARTS AND SCIENCES

Dissertation

**SEARCH FOR INVISIBLE DECAYS OF THE HIGGS  
BOSON PRODUCED VIA VECTOR BOSON FUSION AT  
LHC WITH THE CMS DETECTOR RUN-II DATA**

by

**ALP AKPINAR**

B.Sc., Bogazici University, 2018

Submitted in partial fulfillment of the  
requirements for the degree of  
Doctor of Philosophy

2023

© 2023 by  
ALP AKPINAR  
All rights reserved

**Prior to having this page signed by the readers, please have  
it reviewed by the Mugar Library staff.**

Approved by

First Reader

---

Zeynep Demiragli, PhD  
Assistant Professor, Physics

Second Reader

---

James Rohlf, PhD  
Professor, Physics

*(Some inspiring quote will go here.)*  
*All things are difficult before they are easy.*  
- Dr. Thomas Fuller

## **Acknowledgments**

My acknowledgments will go here.

**SEARCH FOR INVISIBLE DECAYS OF THE HIGGS  
BOSON PRODUCED VIA VECTOR BOSON FUSION AT  
LHC WITH THE CMS DETECTOR RUN-II DATA**

**ALP AKPINAR**

Boston University, Graduate School of Arts And Sciences, 2023

Major Professor: Zeynep Demiragli, PhD  
Assistant Professor, Physics

**ABSTRACT**

There is multiple astrophysical evidence which support the presence of dark matter (DM), which stands out as the one of the open questions in the Standard Model (SM) of Particle Physics. One avenue to look for DM production is using particle colliders such as the Large Hadron Collider (LHC), where the production of DM can be detected as events with large missing transverse momentum ( $p_T^{miss}$ ). This thesis documents a search for new DM particles using proton-proton collision data from LHC, which is recorded by the Compact Muon Solenoid (CMS) detector, at a center of mass energy of 13 TeV. In this search, the target signature is a Higgs boson, produced via Vector Boson Fusion (VBF) process, decaying into a pair of DM particles, resulting in two energetic jets and large  $p_T^{miss}$  in the final state. To estimate the background processes, multiple control regions are defined and a simultaneous fit to data over all regions is performed. The data for this search was collected in 2017 and 2018, during Run II of the LHC. A full result corresponding to an integrated luminosity of  $137\text{fb}^{-1}$  is also obtained by statistically combining this analysis result with the already published 2016 analysis. No excess of events is observed, compared

to the expected SM backgrounds. The results are interpreted in the context of Higgs-portal models, where upper bounds are set to  $BR(H \rightarrow inv.)$ , the branching ratio for the SM Higgs boson decaying to invisible DM particles.

# Contents

<b>1</b>	<b>Theoretical Background</b>	<b>1</b>
<b>2</b>	<b>Experimental Apparatus</b>	<b>2</b>
2.1	The Large Hadron Collider . . . . .	2
2.2	The CMS Detector . . . . .	4
2.2.1	Overall Layout . . . . .	4
2.2.2	Tracking System . . . . .	6
2.2.3	Electromagnetic Calorimeter . . . . .	8
2.2.4	Hadron Calorimeter . . . . .	10
2.2.5	Muon System . . . . .	10
2.2.6	Trigger System . . . . .	12
<b>3</b>	<b>Data Analysis Strategy</b>	<b>13</b>
3.1	Physics objects . . . . .	13
3.1.1	Jets . . . . .	14
3.1.2	Missing transverse momentum and recoil . . . . .	16
3.1.3	Leptons . . . . .	18
3.1.4	Photons . . . . .	23
3.2	Reweighting of simulated events . . . . .	29
3.2.1	Trigger efficiency reweighting . . . . .	29
3.2.2	Pileup reweighting . . . . .	39
3.2.3	Lepton identification efficiency reweighting . . . . .	43
3.2.4	Lepton veto efficiency reweighting . . . . .	48

3.2.5	Reweighting For HF Noise Cuts . . . . .	50
3.2.6	Reweighting for ECAL pre-firing . . . . .	52
3.2.7	Higher-order reweighting . . . . .	52
3.3	Data-quality issues . . . . .	59
3.3.1	Forward HCAL (HF) Noise . . . . .	59
3.3.2	Missing HE-15/16 sectors in 2018 . . . . .	69
3.4	Event selection . . . . .	75
3.4.1	Signal region selection . . . . .	75
3.4.2	Single Muon Control Region . . . . .	85
3.4.3	Single Electron Control Region . . . . .	90
3.4.4	Double Muon Control Region . . . . .	95
3.4.5	Double Electron Control Region . . . . .	100
3.4.6	Photon Control Region . . . . .	105
3.5	Signal extraction strategy . . . . .	110
3.5.1	Binned likelihood fit . . . . .	110
3.5.2	Systematic uncertainties . . . . .	117
<b>4</b>	<b>Results</b>	<b>127</b>
4.1	Combined likelihood fit . . . . .	127
4.2	Combinations . . . . .	134
4.2.1	Combination with VTR category . . . . .	134
4.2.2	Combination with 2016 dataset . . . . .	134
4.3	Interpretations . . . . .	138
4.3.1	Invisible branching fraction of SM Higgs boson . . . . .	138
4.3.2	Upper bound on DM-nucleon interactions . . . . .	139
<b>5</b>	<b>Outlook</b>	<b>142</b>
	<b>Curriculum Vitae</b>	<b>147</b>

# List of Tables

3.1	The $p_T^{miss}$ filters recommended by the JME POG [1]. The recommendations apply to both 2017 and 2018. Except for the bad super cluster filter (“EE badSC”), all filters are applied both in data and simulation (MC). . . . .	18
3.2	Requirements used to define veto electrons in the barrel region ( $ \eta  < 1.479$ ). . . . .	21
3.3	Requirements used to define tight electrons in the barrel region ( $ \eta  < 1.479$ ). . . . .	21
3.4	Requirements used to define veto electrons in the endcap region ( $ \eta  > 1.479$ ). . . . .	22
3.5	Requirements used to define tight electrons in the endcap region ( $ \eta  > 1.479$ ). . . . .	22
3.6	Loose photon identification criteria for photons in the barrel. These photons must also have $p_T > 15 \text{ GeV}$ . . . . .	24
3.7	Loose photon identification criteria for photons in the endcap. These photons must also have $p_T > 15 \text{ GeV}$ . . . . .	24
3.8	Tight photon identification criteria. The criteria are only given for the barrel region since endcap photons are not taken into account. . . . .	24

3.9	Summary of higher-order corrections applied to simulated samples. For each boson production process, separate samples and corrections are available for the EWK and QCD production modes. “MC order” reflects the perturbative order used in the generation of the simulation sample, while the further columns represent corrections applied on a per-event level in the analysis process. . . . .	55
3.10	Summary of the signal region selection requirements. Leading and subleading jets refer to the highest and second-highest $p_T$ jets in the event. . . . .	77
3.11	Experimental and theoretical sources of systematic uncertainties in the $V + \text{jets}$ transfer factors. The second column highlights on which ratio specifically a given source of uncertainty acts. The subscript SR (CR) refers to the process yield in the SR (corresponding CRs). The impact on $M_{jj}$ is given in the 3rd column, either as a single value (if no dependence on $M_{jj}$ is observed) or as a range of impact on low to high $M_{jj}$ values. . . . .	126
4.1	Expected event yields in each $M_{jj}$ bin for the different background processes in the VBF signal region, with the 2017 samples. The background yields and the corresponding uncertainties are obtained after performing a combined fit across all of the CRs and SR. The expected signal contributions for a Higgs boson, produced in the non-VBF and VBF modes, decaying to invisible particles with a branching fraction of $\mathcal{B}(H \rightarrow \text{inv}) = 1$ , and the observed event yields are also reported. .	132

4.2	Expected event yields in each $M_{jj}$ bin for the different background processes in the VBF signal region, with the 2018 samples. The background yields and the corresponding uncertainties are obtained after performing a combined fit across all of the CRs and SR. The expected signal contributions for a Higgs boson, produced in the non-VBF and VBF modes, decaying to invisible particles with a branching fraction of $\mathcal{B}(H \rightarrow \text{inv}) = 1$ , and the observed event yields are also reported. . .	133
4.3	Uncertainty breakdown in $\mathcal{B}(H \rightarrow \text{inv})$ . The sources of uncertainty are separated into different groups. Observed and expected results are quoted for the full combination of 2016, 2017, and 2018 data. The expected results are obtained using an Asimov dataset [2] with $\mathcal{B}(H \rightarrow \text{inv}) = 0$ . . . . .	137
4.4	The 95% CL upper limits on $(\sigma_H/\sigma_H^{\text{SM}})\mathcal{B}(H \rightarrow \text{inv})$ , assuming an SM Higgs boson with a mass of 125.38 GeV. The observed and median expected results are shown, along with the 68% and 95% interquartile ranges for each category and for the combinations. . . . .	139

# List of Figures

2.1	Diagram of the CERN accelerator complex, showing the LHC and the chain of other accelerator rings. Each ring boosts the energy of accelerated particles before injecting it into the next ring in the sequence. The diagram is taken from [3]. . . . .	3
2.2	Sectional view of the CMS detector. The LHC beams travel in opposite directions along the central axis of the CMS cylinder colliding in the middle of the CMS detector [4]. . . . .	5
2.3	Comparison of the layouts between the original pixel detector (bottom) and the Phase-1 upgraded pixel detector (top) [5]. . . . .	7
2.4	Schematic cross section through the CMS tracker. Notice that the pixel detector is shown as the 2016 version. The image is taken from [6].	8
2.5	Layout of the CMS electromagnetic calorimeter showing the arrangement of crystal modules, supermodules and endcaps, with the preshower in front [6]. . . . .	9
2.6	Longitudinal view of the CMS detector showing the locations of the hadron barrel (HB), endcap (HE), outer (HO) and forward (HF) calorimeters [6]. . . . .	11
3.1	Subleading AK4 jet $\eta$ distribution in single muon control region with JER corrections applied (left) and without JER corrections applied (right). . . . .	15

3.2	Template fits used to determine the photon purity in the 2017 dataset. The fits are shown in bins of photon $p_T$ , increasing from left to right and top to bottom. The “nominal” binning scheme is used. . . . .	27
3.3	Template fits used to determine the photon purity in the 2018 dataset. The fits are shown in bins of photon $p_T$ , increasing from left to right and top to bottom. The “nominal” binning scheme is used. . . . .	28
3.4	Photon impurity as a function of photon $p_T$ for 2017 (left) and 2018 (right). The measured values for different binning choices are shown in the blue shaded lines and markers. The nominal result is interpolated using an exponential function fit, which is shown in the red solid line. The gray band represents a 25% uncertainty around the interpolated nominal result. . . . .	29
3.5	Comparison of binning schemes used to define a systematic uncertainty on the purity measurement. In all cases, the $200 < p_T < 300 \text{ GeV}$ bin of the 2017 data set is shown. The binning choices are very fine and fine (top row), nominal (middle row) and coarse and very coarse (bottom row). . . . .	30
3.6	MET trigger efficiencies for data and MC, for events where the two VBF jets are both central (top) and where at least one jet is forward (bottom). Left column shows results with 2017 dataset, while the right column shows the results with 2018 dataset. To each efficiency curve, a sigmoid function with three parameters are fitted: $f(x, a, b, c) =$ $\frac{c}{1+e^{-a(x-b)}}$ . Resulting data/MC scale factors are shown in the bottom ratio pad for each case. The black line represents the ratio of two best- fit sigmoid functions, which is used as the correction factor to MC as a function of recoil. . . . .	33

3.7 Efficiency of the HLT_Photon200 trigger in data and $H_T$ -binned $\gamma+\text{jets}$ MC for 2017 (top) and 2018 (bottom) as a function of photon $p_T$ . The orange and blue lines respectively represent sigmoid function fits to the turn-on in data and MC, with the fit function and best-fit parameter values given in the respectively colored labels. The bottom panel shows the ratio of the values measured in data over those in MC using orange markers. The solid black line corresponds to the ratio of the sigmoid fits to data and MC. . . . .	36
3.8 Efficiency of the OR of the three triggers used to select electron events for 2017 (top) and 2018 (bottom) as a function of the electron transverse momentum. The efficiency is shown for multiple regions of absolute electron pseudorapidity. In each plot, the upper panel shows the efficiency in data, while the lower panel shows the ratio of the efficiency in data and that in simulation. . . . .	38
3.9 Distribution of the true number of PU events in data and simulation for 2017 (left) and 2018 (right). The distributions for data are extracted assuming a minimum bias cross section of 69.2 mb. . . . .	40
3.10 Distribution of the number of vertices in $W \rightarrow \mu\nu$ events in data and simulation before pileup re-weighting (left) and after pileup reweighting (right). The Monte Carlo is normalized to the luminosity of 41.53 and $59.7 \text{ fb}^{-1}$ , respectively for 2017 and 2018. . . . .	41
3.11 Distribution of the event energy density $\rho$ in $W \rightarrow \mu\nu$ events in data and simulation before pileup re-weighting (left) and after pileup reweighting (right). The Monte Carlo is normalized to the luminosity of 41.53 and $59.7 \text{ fb}^{-1}$ , respectively for 2017 and 2018. . . . .	42

3.12 Scale factors for the reconstruction efficiency of electrons starting from a super cluster for 2017 (left) and 2018 (right), for electrons with $p_T > 20 \text{ GeV}$ (top) and $p_T < 20 \text{ GeV}$ (bottom). . . . .	44
3.13 Scale factors for the identification efficiency of tight (left) and veto (right) electrons are shown for 2017 (top) and 2018 (bottom). The scale factors are provided in bins of electron $p_T$ and $\eta$ . . . . .	45
3.14 Scale factors for tight (left) and veto (right) muon identification are shown for 2017 (top) and 2018 (bottom). The scale factors are provided in bins of muon $p_T$ and $\eta$ . . . . .	46
3.15 Scale factors for tight (left) and veto (right) muon isolation are shown for 2017 (top) and 2018 (bottom). The scale factors are provided in bins of muon $p_T$ and $\eta$ . . . . .	47
3.16 The impact of the veto weight corrections on $W(\ell\nu)+\text{jets}$ process in the signal region. The correction with the nominal lepton veto weight and the uncertainties of the veto weight are shown, and the event yield ratio with the hard lepton veto case is plotted. The top row corresponds to the tau veto, middle row to electron veto, and last row corresponds to muon veto. Left and right columns represent 2017 and 2018 datasets, respectively. . . . .	49
3.17 HF scale factors and their statistical uncertainties as a function of jet $p_T$ and $\eta$ , for 2017 (left) and 2018 (right). For the phase space with statistical limitations (i.e. $SF = 0$ ), the scale factor in the closest $[p_T, \eta]$ bin is applied to the HF jet. . . . .	51
3.18 The $M_{jj}$ distributions with the nominal prefiring weights and its variations are shown for $W + \text{jets}$ simulation in single lepton CRs (top), and $Z + \text{jets}$ simulation in double lepton CRs (bottom). . . . .	53

3.19 The $M_{jj}$ distributions with the nominal prefire weights and its variations are shown for $\gamma +$ jets simulation in the photon CR (top left), $W(\ell\nu) +$ jets (top right), $Z(\nu\nu) +$ jets (bottom left) and VBF $H \rightarrow inv.$ (bottom right) in the signal region. . . . .	54
3.20 LO-to-NLO theory scale factors binned in the generator-level boson $p_T$ and $M_{jj}$ , shown photon production. The k factors are derived within the generator-level VBF selection described in the text. The uncertainties quoted in each bin are the statistical uncertainties due to the finite size of the simulated samples. . . . .	57
3.21 EWK NLO scale factors for DY, W and photon production as a function of $p_{T,V}$ . . . . .	57
3.22 QCD NLO scale factors for EWK DY, W production of $p_{T,V}$ and $M_{jj}$ . . . . .	58
3.23 Two dimensional distribution of $\sigma_{i\eta i\eta}$ and $\sigma_{i\phi i\phi}$ in the noise-enriched region, split by the $ \eta $ of the jet. The first plot shows $2.99 <  \eta  < 3.25$ interval, the second one shows $3.25 <  \eta  < 4$ and the last one shows $4 <  \eta  < 5.2$ . The red lines on the plots indicate the cuts applied on these variables. . . . .	63
3.24 Two dimensional distribution of $\sigma_{i\eta i\eta}$ and $\sigma_{i\phi i\phi}$ in the physics-enriched region, split by the $ \eta $ of the jet. The first plot shows $2.99 <  \eta  < 3.25$ interval, the second one shows $3.25 <  \eta  < 4$ and the last one shows $4 <  \eta  < 5.2$ . The red lines on the plots indicate the cuts applied on these variables. . . . .	64
3.25 Two dimensional distribution of central and adjacent strip sizes in the noise enriched region, split by the $ \eta $ of the jet. The first plot shows $2.99 <  \eta  < 3.25$ interval, the second one shows $3.25 <  \eta  < 4$ and the last one shows $4 <  \eta  < 5.2$ . . . . .	65

3.26 Two dimensional distribution of central and adjacent strip sizes in the physics enriched region, split by the $ \eta $ of the jet. The first plot shows $2.99 <  \eta  < 3.25$ interval, the second one shows $3.25 <  \eta  < 4$ and the last one shows $4 <  \eta  < 5.2$ . . . . .	66
3.27 HF noise estimate in 2017 (top) and 2018 (bottom) data. The plots on the left column show the data and total MC yields in the HF noise control region, scaled by the jet-based transfer factor, while the plots on the right show the resulting noise estimation in the signal region, which correspond to the difference of data and MC yields in the left-hand side plot. . . . .	68
3.28 $\Delta\phi(p_{T,miss}^{miss}, p_T^{miss})$ distribution for the closure test on the HF noise estimate. Events plotted here pass the VBF signal region selection, and have the leading jet in $3 <  \eta  < 3.25$ range, where the HF noise contribution is highest. It can be observed, especially at high $\Delta\phi(p_{T,miss}^{miss}, p_T^{miss})$ , the agreement between data and background yields is good after the residual HF noise estimation is taken into account. To account for residual differences, a 20% flat uncertainty is assigned to the HF noise template. . . . .	70
3.29 Effects of an electron veto in the affected detector region (single electron control region 2018). Plots on the top show the $\eta$ and $\phi$ of the highest $p_T$ electron in the event without any veto, while plots on the bottom show the $\eta$ and $\phi$ of the electron with the veto. . . . .	72
3.30 Leading (left) and subleading (right) jet $\phi$ distributions in the signal region from the 2018 dataset. The bands in the ratio plots represent the statistical uncertainties in the MC. . . . .	73
3.31 $\phi_{p_T^{miss}}$ distribution in the signal region from the 2018 dataset. . . . .	74

3.32 Recoil distribution, $M_{jj}$ distribution, $\Delta\eta_{jj}$ and $\Delta\phi_{jj}$ distribution in the VBF signal region, using 2017 dataset. . . . .	79
3.33 Leading and subleading jets $p_T$ and $\eta$ in the VBF signal region, using 2017 dataset. . . . .	80
3.34 Most central (left) and most forward jets (right) $\eta$ of the VBF pair in the VBF signal region, using 2017 dataset. . . . .	81
3.35 Recoil distribution, $M_{jj}$ distribution, $\Delta\eta_{jj}$ and $\Delta\phi_{jj}$ distribution in the VBF signal region, using 2018 dataset. . . . .	82
3.36 Leading and subleading jets $p_T$ and $\eta$ in the VBF signal region, using 2018 dataset. . . . .	83
3.37 Most central (left) and most forward jets (right) $\eta$ of the VBF pair in the VBF signal region, using 2018 dataset. . . . .	84
3.38 Comparison between 2017 data and Monte Carlo simulation in the single muon control region for the recoil, $M_{jj}$ distribution, $\Delta\eta_{jj}$ and $\Delta\phi_{jj}$ distributions for the two leading AK4 jets. . . . .	86
3.39 Comparison between 2017 data and Monte Carlo simulation in the single muon control region for the $p_T$ and $\eta$ distribution of the reconstructed muon. . . . .	87
3.40 Comparison between 2018 data and Monte Carlo simulation in the single muon control region for the recoil, $M_{jj}$ distribution, $\Delta\eta_{jj}$ and $\Delta\phi_{jj}$ distributions for the two leading AK4 jets. . . . .	88
3.41 Comparison between 2018 data and Monte Carlo simulation in the single muon control region for the $p_T$ and $\eta$ distribution of the reconstructed muon. . . . .	89

3.42 Comparison between 2017 data and Monte Carlo simulation in the single electron control region for the recoil, $M_{jj}$ distribution, $\Delta\eta_{jj}$ and $\Delta\phi_{jj}$ distributions for the two leading AK4 jets. . . . .	91
3.43 Comparison between 2017 data and Monte Carlo simulation in the single electron control region for the $p_T$ and $\eta$ distribution of the reconstructed electron. . . . .	92
3.44 Comparison between 2018 data and Monte Carlo simulation in the single electron control region for the recoil, $M_{jj}$ distribution, $\Delta\eta_{jj}$ and $\Delta\phi_{jj}$ distributions for the two leading AK4 jets. . . . .	93
3.45 Comparison between 2018 data and Monte Carlo simulation in the single electron control region for the $p_T$ and $\eta$ distribution of the reconstructed electron. . . . .	94
3.46 Comparison between 2017 data and Monte Carlo simulation in the double muon control region for the recoil, $M_{jj}$ distribution, $\Delta\eta_{jj}$ and $\Delta\phi_{jj}$ distributions for the two leading AK4 jets. . . . .	96
3.47 Comparison between 2017 data and Monte Carlo simulation in the double muon control region for the $p_T$ and $\eta$ of the leading muon (top), dimuon mass and minimum $\Delta\phi$ between 4 leading jets and recoil (bottom). . . . .	97
3.48 Comparison between 2018 data and Monte Carlo simulation in the double muon control region for the recoil, $M_{jj}$ distribution, $\Delta\eta_{jj}$ and $\Delta\phi_{jj}$ distributions for the two leading AK4 jets. . . . .	98
3.49 Comparison between 2018 data and Monte Carlo simulation in the double muon control region for the $p_T$ and $\eta$ of the leading muon (top), dimuon mass and minimum $\Delta\phi$ between 4 leading jets and recoil (bottom). . . . .	99

3.50 Comparison between 2017 data and Monte Carlo simulation in the double electron control region for the recoil, $M_{jj}$ distribution, $\Delta\eta_{jj}$ and $\Delta\phi_{jj}$ distributions for the two leading AK4 jets. . . . .	101
3.51 Comparison between 2017 data and Monte Carlo simulation in the double electron control region for the $p_T$ and $\eta$ of the leading electron (top), dielectron mass and minimum $\Delta\phi$ between 4 leading jets and recoil (bottom). . . . .	102
3.52 Comparison between 2018 data and Monte Carlo simulation in the double electron control region for the recoil, $M_{jj}$ distribution, $\Delta\eta_{jj}$ and $\Delta\phi_{jj}$ distributions for the two leading AK4 jets. . . . .	103
3.53 Comparison between 2018 data and Monte Carlo simulation in the double electron control region for the $p_T$ and $\eta$ of the leading electron (top), dielectron mass and minimum $\Delta\phi$ between 4 leading jets and recoil (bottom). . . . .	104
3.54 Comparison between 2017 data and Monte Carlo simulation in the photon control region for the recoil distribution, the $M_{jj}$ distribution, $\Delta\eta_{jj}$ distribution and $\Delta\phi_{jj}$ distribution for the two leading AK4 jets. $M_{jj}$ and recoil distributions include the QCD estimate calculated from the photon purity measurement, as described in Sec. 3.1.4. . . . .	106
3.55 Comparison between 2017 data and Monte Carlo simulation in the photon control region for the $p_T$ and $\eta$ of the leading photon. . . . .	107
3.56 Comparison between 2018 data and Monte Carlo simulation in the photon control region for the recoil distribution, the $M_{jj}$ distribution, $\Delta\eta_{jj}$ distribution and $\Delta\phi_{jj}$ distribution for the two leading AK4 jets. $M_{jj}$ and recoil distributions include the QCD estimate calculated from the photon purity measurement, as described in Sec. 3.1.4. . . . .	108

3.57 Comparison between 2018 data and Monte Carlo simulation in the photon control region for the $p_T$ and $\eta$ of the leading photon. . . . .	109
3.58 Transfer factors between $Z$ and $W$ control regions as a function of the dijet mass. Results for both 2017 (left) and 2018 (right) datasets are shown. Plots on the top row show the ratios between the electron regions, while the plots on the bottom show the ratios between muon regions. The bands show the theoretical and experimental systematic uncertainties on the ratios. . . . .	115
3.59 Transfer factors for $Z(ee)/\gamma + jet$ (top) and $Z(\mu\mu)/\gamma + jets$ (bottom) processes. Results with 2017 datasets are shown on the left column, and 2018 results are shown on the right column. The bands show the experimental systematic uncertainties on the ratios. . . . .	116
3.60 Theoretical uncertainties on $W/Z$ (top) and $\gamma/Z$ (bottom) transfer factors. Uncertainties are calculated as a function of $M_{jj}$ . Uncertainties for QCD ratios are shown on the left column, while uncertainties for EWK ratios are shown on the right column. . . . .	119
3.61 Uncertainty due to the L1 prefire reweighting as a function of $M_{jj}$ . The uncertainty is computed from VBF $H \rightarrow inv.$ signal sample by varying the prefiring weight within its uncertainty. This uncertainty is applied as a shape uncertainty to all $H \rightarrow inv.$ signals considered in the analysis. . . . .	121
3.62 All single-bin JES/JER uncertainties on QCD Z(SR)/Z(CR) ratio for 2017 (left) and 2018 (right). The black dot shows the JER uncertainty, and the others show up and down variation from all 11 JES sub-sources. All jet energy scale and resolution uncertainties cancel to within less than 1%. . . . .	122

3.63 All single-bin JES/JER uncertainties on QCD Z(SR)/ $\gamma$ ratio for 2017 (left) and 2018 (right). The black dot shows the JER uncertainty, and the others show up and down variation from all 11 JES sub-sources. All jet energy scale and resolution uncertainties cancel within up to 2%.	123
3.64 Relative sample JEC uncertainties calculated with strong Z( $\nu\nu$ ) + jets (top) and VBF $H \rightarrow \text{inv.}$ signal (bottom). Left column shows the 2017 results, while the right column shows the 2018 results. The fitted uncertainties, shown in solid lines, are used as the final uncertainty shapes. . . . .	124
4.1 Comparison between data and background estimation in VBF SR (top) and $\gamma$ + jets CR (bottom), before and after the simultaneous fit. The fit includes the data in all CRs and the signal region. The resulting distributions are shown separately for 2017 (left) and 2018 (right). In the ratio pads, ratios of data and background estimation are shown before (red) and after (blue) the fit. The gray band indicates the post-fit uncertainty. Finally, the distribution of the difference between data and post-fit background prediction relative to the quadrature sum of the uncertainties in the prediction and in data is shown in the lowest panel. . . . .	129
4.2 Same as Fig. 4.1 but with dilepton CRs. The other backgrounds include top quark and diboson processes. . . . .	130
4.3 Same as Fig. 4.1 but with single lepton CRs. The other backgrounds include top quark and diboson processes. . . . .	131

- 4.4 The observed  $M_{jj}$  distribution in the VBF signal region compared to the postfit backgrounds, with the 2016, 2017, and 2018 datasets. The signal processes are scaled by the fitted value of  $\mathcal{B}(H \rightarrow \text{inv})$ , shown in the legend. The background contributions are estimated from the fit to the data described in Sec. 3.5.1 (S+B fit). Total background estimated from a fit assuming  $\mathcal{B}(H \rightarrow \text{inv}) = 0$  (B-only fit) is also shown. The last bin of each distribution integrates events above the bin threshold divided by the bin width. Figure taken from [7]. . . . . 136
- 4.5 Observed and expected 95% CL upper limits on  $(\sigma_H/\sigma_H^{\text{SM}})\mathcal{B}(H \rightarrow \text{inv})$  for all three data-taking years, together with the  $1\sigma$  (green) and  $2\sigma$  (yellow) uncertainty bands on the expected upper limits. The combination of 2016-2018 is also shown. These results assume a SM Higgs boson with a mass of 125.38 GeV. Figure taken from [7]. . . . . 138
- 4.6 The 90% CL upper limits on the spin-independent DM-nucleon scattering cross section in Higgs-portal models, assuming a scalar (dashed orange) or fermion (dashed red) DM candidate. Limits are computed as functions of  $m_{\text{DM}}$  and are compared to those from the Xenon1T [8], Cressst-II [9], CDMSlite [10], LUX [11], Panda-X 4T [12], and DarkSide-50 [13] experiments, which are shown as solid lines. Figure taken from [7]. 141

## List of Abbreviations

ALICE	.....	A Large Ion Collider Experiment
ATLAS	.....	A Toroidal LHC Apparatus
BR	.....	Branching ratio
BSM	.....	Beyond the Standard Model of Particle Physics
CERN	.....	European Council for Nuclear Research
CMS	.....	Compact Muon Solenoid
CR	.....	Control region
DM	.....	Dark matter
ECAL	.....	Electromagnetic calorimeter
HCAL	.....	Hadronic calorimeter
HF	.....	Forward hadronic calorimeter
JME	.....	JetMET physics object group
LHC	.....	Large Hadron Collider
LHCb	.....	Large Hadron Collider beauty experiment
LO	.....	Leading order
MC	.....	Monte Carlo simulation
MET	.....	Missing transverse energy
NLO	.....	Next-to-leading order
POG	.....	Physics object group
PF	.....	Particle flow algorithm
PU	.....	Pileup
SF	.....	Scale factor
SM	.....	Standard Model of Particle Physics
SR	.....	Signal region
VBF	.....	Vector boson fusion

## **Chapter 1**

# **Theoretical Background**

Discussion about Standard Model, astronomical dark matter observations and motivation for  $H \rightarrow \text{inv.}$  searches will go here.

## Chapter 2

# Experimental Apparatus

### 2.1 The Large Hadron Collider

The Large Hadron Collider (LHC), located near Geneva, Switzerland, is a superconducting circular particle accelerator, consisting of a 27-kilometer ring of superconducting magnets. For the majority of the time, protons are used as the accelerated particles, but in addition to protons, Xe and Pb ions are also used for heavy ion studies. For the context of this thesis, data from only the proton collisions are being considered.

Two sets of proton bunches travel along the circular tunnel in opposite directions, being accelerated to near the speed of light, then collide at the experiment sites. The four large experiments located at the LHC ring are CMS, ATLAS, LHCb and ALICE. CMS and ATLAS are multi-purpose detectors, while LHCb focuses on heavy hadron physics, and ALICE focuses on heavy ion physics. The center-of-mass energy for the proton-proton collision for Run II is 13 TeV. This energy is further increased to 13.6 TeV in more recent runs of the LHC, corresponding to Run III.

Protons are accelerated through a chain of accelerators before they reach LHC, which is shown in Fig. 2.1. Each machine boosts the energy of protons before injecting it into the next machine in the sequence. Linear Accelerator 4 (LINAC4) is the source of protons, accelerating  $H^-$  ions to 160 MeV to prepare them to enter the Proton Synchotron Booster (PSB). During the injection to PSB, the two ions are stripped from the  $H^-$  ions, leaving only the protons. These protons are accelerated to 2

GeV for injection to Proton Synchotron (PS), which increases the beam energy to 26 GeV. The proton beam is then sent to Super Proton Synchotron (SPS), where it is accelerated to an energy of 450 GeV. Finally, the proton beam is transferred to the two beam pipes of the LHC. Here, it takes 20 minutes for the protons to reach their maximum energy of 6.5 TeV.

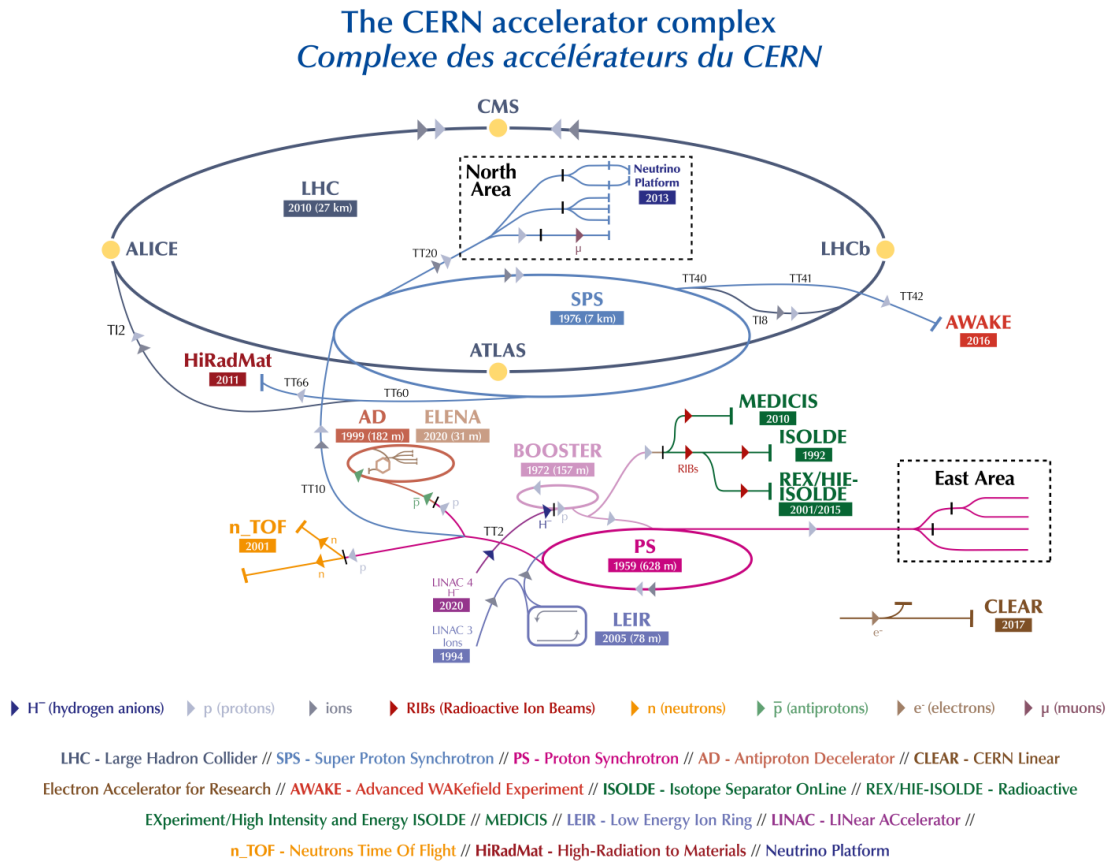


**Figure 2·1:** Diagram of the CERN accelerator complex, showing the LHC and the chain of other accelerator rings. Each ring boosts the energy of accelerated particles before injecting it into the next ring in the sequence. The diagram is taken from [3].

The LHC had a successful Run I between 2010 and 2013, where the center-of-mass energy for proton-proton collisions was 8 TeV. This first run was marked by the discovery of the Higgs boson by ATLAS and CMS experiments in 2012. After a long

shutdown, the center-of-mass energy was increased to 13 TeV, and the LHC operated from 2016 to 2018 for Run II data taking. During Run II, the instantenous luminosity was about  $1 \times 10^{34} \text{ cm}^{-2}\text{s}^{-1}$ , corresponding to around 25 proton-proton collisions per bunch crossing. The integrated luminosity corresponding to Run II data taken by the CMS experiment is measured to be  $137 \text{ fb}^{-1}$ , with 1.6% overall uncertainty [14–16].

## 2.2 The CMS Detector

The CMS detector is a multi-purpose detector, designed trigger on [17, 18] and detect muons, electrons, photons, charged and neutral hadrons [19–21]. To be able to identify this wide range of particles, the CMS detector uses a combination of signals from different sub-detectors. These signals are then used in the Particle-Flow (PF) algorithm to reconstruct the particles in the event. The sub-detectors in the CMS detector are:

- Tracking system
- Electromagnetic calorimeter (ECAL)
- Hadron calorimeter (HCAL)
- Muon system

CMS detector also uses a two-level trigger system [17, 18], to make physics-based decisions on the data being saved to disk, therefore reducing the output rate. In the following sub-sections, the functionality of these subsystems and the overall design of the CMS detector are discussed.

### 2.2.1 Overall Layout

The CMS detector has an overall length of 28.7 meters, and weighs 14000 tonnes. The cylindrical detector has a diameter of 15 meters, as shown in Fig. 2·2. The

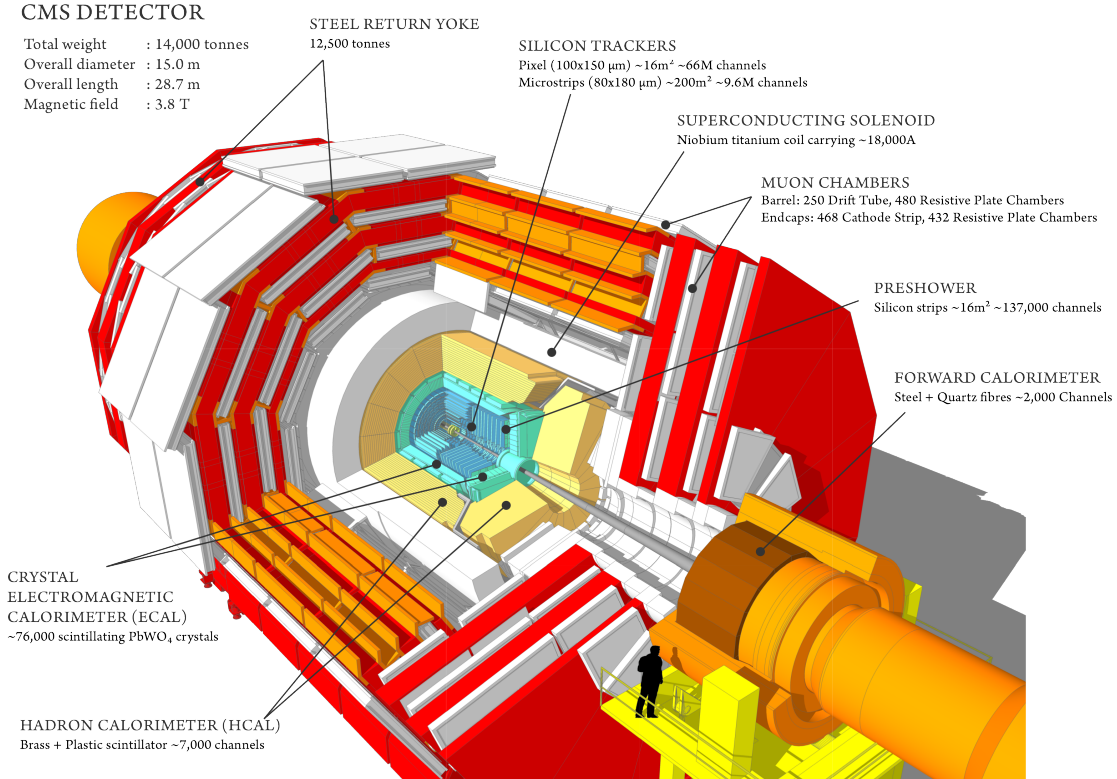


**Figure 2·2:** Sectional view of the CMS detector. The LHC beams travel in opposite directions along the central axis of the CMS cylinder colliding in the middle of the CMS detector [4].

CMS detector has a superconducting solenoid, which has an internal diameter of 7 meters, and creates a magnetic field of 3.8 T. This magnetic field curves the charged particles as they pass through the detector, hence enabling the measurement of their momentum from the radius of curvature of their tracks.

Within the solenoid volume are a silicon pixel and strip tracker, a lead tungstate crystal electromagnetic calorimeter (ECAL), and a brass and scintillator hadron calorimeter (HCAL), each composed of a barrel and two endcap sections. Forward calorimeters are installed in the high pseudo-rapidity range to extend the coverage of the detector. Outside of the solenoid volume, a muon detection system is installed, where muons are measured in gas-ionization detectors embedded in the steel

flux-return yoke.

In the CMS detector, the right-handed coordinate system is used. The x-axis points to the center of the LHC ring, the y-axis points up, and the z-axis point along the beam in the counter-clockwise direction. Due to the cylindrical symmetry of the detector geometry, the angular coordinates of  $\eta$  and  $\phi$  are often used to describe event kinematics.  $\phi$  is the azimuthal angle, defined to be 0 along the x-axis, and  $\frac{\pi}{2}$  along the y-axis.  $\eta$  is the psuedo-rapitiy, which depends on the angle from the z-axis,  $\theta$ , with the following equation:  $\eta = -\ln[\tan(\frac{1}{\theta})]$ . This way,  $\eta$  equals to 0 along the z-axis, directly perpendicular to the beam-axis, and  $|\eta| \rightarrow \infty$  as the  $\theta \rightarrow \frac{\pi}{2}$ , i.e. perpendicular to the beam axis. Most detector coverage extends to until  $|\eta| = 5$ .

### 2.2.2 Tracking System

The innermost layer of the CMS detector is the tracking system. This tracking system consists of a silicon pixel detector and a silicon strip detector, referred to as the inner tracker and the outer tracker, respectively. Both are used to reconstruct tracks of charged particles, under the influence of the 3.8 T magnetic field generated by the solenoid. The inner pixel detector has higher granularity, therefore it can reconstruct tracks more accurately near the beam pipe, where the track density is higher.

Tracks of charged particles are crucial objects for CMS, because they allow measuring the momenta and the electrical charges of particles. These particles include electrons, muons, taus and charged hadrons. The identification of tracks also allow to reconstruct the proton-proton collision vertices in the event. This enables the identification of the primary vertex in the event with the highest sum of  $p_{T,track}^2$ . Thus, the rest of the vertices can be identified as pile-up (PU), and charged particles from these PU vertices can be rejected in object reconstruction. Track reconstruction also allows to identify b-quarks by identifying displaced vertices.

The CMS inner tracker was upgraded during the year-end technical stop of the

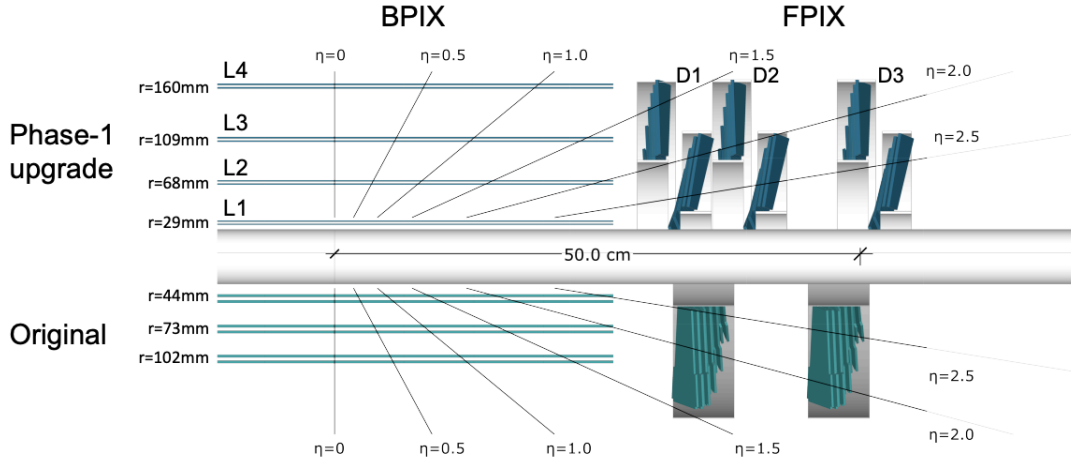


**Figure 2·3:** Comparison of the layouts between the original pixel detector (bottom) and the Phase-1 upgraded pixel detector (top) [5].

LHC in 2016/2017, referred to as the Phase-1 upgrade [5], in order to handle the instantaneous luminosity that exceeds the previously designed maximum value of  $1 \times 10^{34} \text{ cm}^{-2}\text{s}^{-1}$ . Utilizing the new beam pipe with smaller radius installed during the LHC Long Shutdown 1 (LS1), the Phase-1 pixel detector sits closer to the beam center, with 4 barrel layers (L1-L4) at radii of 29, 68, 109, and 160 mm, compared to the original three layers at 44, 73, and 102 mm. There is also an additional endcap disk on each end closer to the collision point. Therefore, there are now three disks at each end with distances of 291, 396, and 516 mm from the center of the detector, compared to the original three layers at 345 and 465 mm. This new layout is optimized to have 4-hit coverage for tracks within  $|\eta| < 2.5$ . The original and the upgraded pixel detector layouts are shown in Fig. 2·3.

Outside of the pixel detector, the silicon strip tracker is installed, which consists of three subsystems: the Tracker Inner Barrel and Disks (TIB/TID), the Tracker Outer Barrel (TOB), and the the Tracker EndCaps (TEC). Their radii range from 20 cm to 116 cm and are up to 282 cm away from the detector center in the z direction. The layout of the silicon strip tracker, together with the 2016 version of the pixel detector,

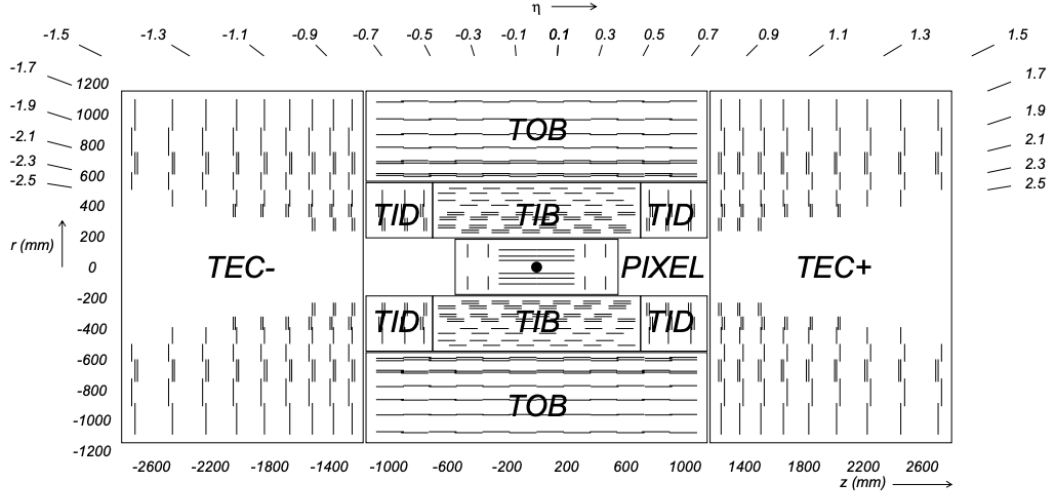


**Figure 2·4:** Schematic cross section through the CMS tracker. Notice that the pixel detector is shown as the 2016 version. The image is taken from [6].

is shown in Fig. 2·4.

### 2.2.3 Electromagnetic Calorimeter

The electromagnetic calorimeter (ECAL) is installed on the second layer of the detector, outside the inner and outer tracking systems. It is made of 61200 lead tungstate ( $PbWO_4$ ) crystals mounted in the barrel (EB), and 7324 of those crystals in each of the 2 endcaps (EE). The  $PbWO_4$  crystals make a radiation-resistant high-granularity calorimeter, due to its high density and short radiation length. The EB section covers the pseudo-rapidity range of  $|\eta| < 1.479$ , and the two EE sections cover  $1.479 < |\eta| < 3.0$ .

The energy of particles, primarily electrons and photons, are measured through the scintillation effect. Photons emitted from the scintillation are collected by the avalanche photodiodes (APD) in the barrel and vacuum phototriodes (VPT) in the EE. Two pre-shower detectors are placed on the inner side of the EEs, which helps to distinguish high-energy photons from pions, which can decay into a pair of closeby

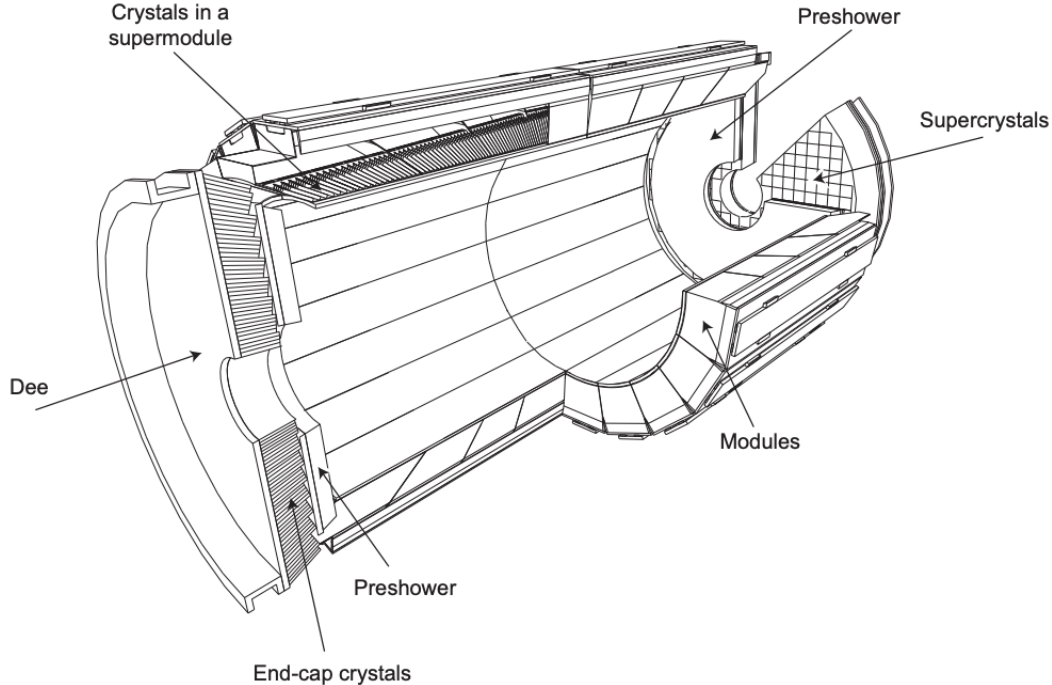


**Figure 2·5:** Layout of the CMS electromagnetic calorimeter showing the arrangement of crystal modules, supermodules and endcaps, with the preshower in front [6].

low-energy photons. The preshower is a sampling calorimeter made of two planes on each end. Each plane has a layer of lead radiators to produce electromagnetic showers from incoming photons and electrons, and a silicon strip detector to measure the energy and shower profile. The silicon strips are placed with a width of 2 mm, and are oriented in perpendicular directions between two layers, giving a much finer granularity than EE and EB.

The crystals in the barrel section are contained by 1 mm wall of aluminum, which constitutes a submodule. 400 or 500 submodules are assembled into a module, and every four of each constitute a supermodule. The crystals in the EE are organized in units of identically shaped  $5 \times 5$  crystals called supercrystals. Each EE is divided into two halves (Dees). The structure of the ECAL is shown in Fig. 2·5.

### 2.2.4 Hadron Calorimeter

The hadron calorimeter (HCAL) is designed to measure the energy of hadrons, which is specifically important for reconstructing and measuring the energy of hadron jets. The HCAL is composed of several parts:

- A barrel part (HB), which sits between the ECAL and the magnet coil, covering the range of  $|\eta| < 1.3$ .
- An endcap part (HE), covering the range of  $1.3 < |\eta| < 3$ .
- Forward hadron calorimeters (HF), which are placed close to the beam pipe to capture outgoing particles with small angles, covering up to  $|\eta| < 5$ .

Due to the limited space between the ECAL and the magnet coils, additional hadron calorimeters (HO) are placed outside of the magnet coils to help contain hadron showers. The layout of the HCAL detector is shown in Fig. 2.6.

The majority of HCAL is a sampling calorimeter made of alternating absorbing layers of brass and plastic scintillating layers. The forward calorimeter HF utilizes a different design, which consists of a steel absorber and quartz fibers that generate Cherenkov light, in order to operate in a much harsher radiation environment, compared to other parts of the calorimeter.

### 2.2.5 Muon System

Muon detection is of great importance to the CMS, since it is a powerful tool for recognizing signatures of interesting physics processes. Muons also have the potential to be reconstructed with a larger resolution since they are less affected by radiative losses in the tracker material, compared to electrons.

The muon system is installed in the psuedo-rapidity range of  $|\eta| < 2.4$ , consisting of drift tubes (DTs), cathode strip chambers (CSCs) and resistive plate chambers

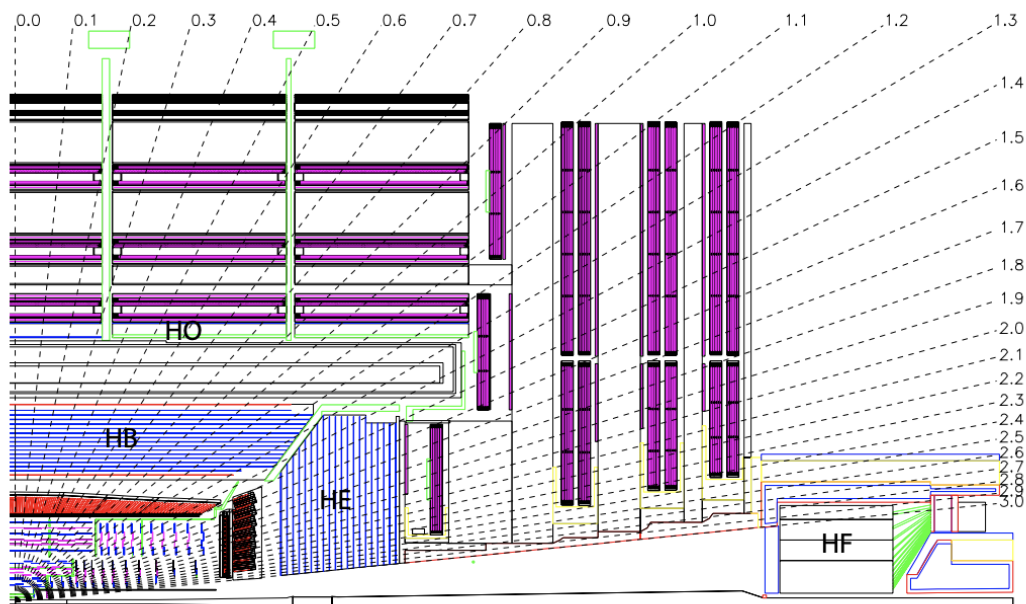


**Figure 2.6:** Longitudinal view of the CMS detector showing the locations of the hadron barrel (HB), endcap (HE), outer (HO) and forward (HF) calorimeters [6].

(RPCs). The DTs are placed in the barrel and cover the  $|\eta| < 1.2$  range, where the particle rate and the local magnetic field strength are low. CSCs, due to their fast response time, fine segmentation, and radiation resistance, are used in the endcap, covering  $0.9 < |\eta| < 2.4$ . RPCs are inserted into both barrel and endcaps to provide redundant trigger system with a time resolution of 1 ns, which is much shorter than the bunch crossing interval of 25 ns.

### 2.2.6 Trigger System

With a bunch crossing of 25 ns, collecting and saving all collision events at a rate of 400 MHz is unsustainable, due to limitations in both storage space and data transfer rates. Storing all the events at this rate is also unnecessary, since interesting events with high-energy physics objects occur at a much lower rate.

To select the events of interest and reduce the rate of data being saved, a two-tiered trigger system is being used in the CMS experiment. The first-level trigger (L1), is composed of custom hardware processors, which uses event information from the calorimeters and the muon system to select events at a rate of 100 kHz within a fixed latency of about  $4 \mu\text{s}$  [17]. The second level, known as the high-level trigger (HLT), consists of processors running a version of the full event reconstruction software optimized for fast processing, and reduces the event rate to around 1 kHz before data storage [18].

# Chapter 3

## Data Analysis Strategy

### 3.1 Physics objects

A global event reconstruction using the Particle Flow (PF) algorithm [22] is carried out in order to identify each particle in the event. PF algorithm accomplishes this by combining detector hit information from all different sub-detectors within the CMS. The specific information used to determine the energy and momentum of a particle depends on the identity of the particle: Whether it is a photon, muon, electron, neutral hadron or charged hadron. Photons are identified as ECAL energy clusters that are not linked to any charged particle tracks. Electrons are identified as a primary charged particle track, potentially together with ECAL energy clusters that are consistent with either the extrapolation of this track or possible bremsstrahlung photons emitted when the electron passes through the tracker material. Muons are identified as consistent charged particle tracks in both the central tracker and the muon system, as well as potential energy clusters in the calorimeters that are consistent with the tracks. Tracks that are not already assigned to electrons or muons, together with calorimeter energy deposits, are identified as charged hadrons. Finally, neutral hadrons are identified using leftover HCAL and ECAL clusters after the identification of charged hadrons.

During event reconstruction, a primary proton-proton collision vertex is selected as the vertex containing the largest sum of  $p_T^2$  from associated tracks [23]. This way, charged particles can be filtered out if their tracks originate from a non-primary

vertex, hence reducing the pileup (PU) in the event.

In the following subsections, details of how different physics objects are reconstructed will be discussed. To aid the discussion, signal region (SR) refers to the set of selections used to collect VBF  $H \rightarrow \text{inv.}$  signal events, and control regions (CR) refer to the set of selections used to measure dominant background yields.

### 3.1.1 Jets

A typical jet consists of a shower of hadrons generated by a single quark or gluon. In this analysis, jets are reconstructed by clustering reconstructed particles using the anti- $k_T$  algorithm [24]. Jets are clustered with a distance parameter of 0.4 and are referred to as AK4 jets.

Jet momentum is determined as the vector sum of all particle momenta in the jet, and is found from simulation to be within 5 to 10% of the true momentum over the full  $p_T$  spectrum and detector acceptance. An offset correction is applied to jet energies to take into account the contribution from additional proton-proton interactions within the same or nearby bunch crossings (pileup). Jet energy corrections are derived from simulation, and are confirmed with measurements of the energy balance in dijet, multijet,  $\gamma$ +jet, and  $Z(\ell\ell)$ +jet events [25]. For the analysis that will be explained in this thesis, the `Summer19UL17_V5` and `Summer19UL18_V5` versions of the jet energy corrections are used for the 2017 and 2018 datasets, respectively [26].

The AK4 jets used in this analysis are required to pass the loose identification criteria [27], and AK4 jets with  $p_T < 50 \text{ GeV}$  must pass the pileup identification (ID) criteria [28]. Pileup ID criteria aims to reduce the contribution from pileup by removing jets that contain a large number of energy from secondary vertices.

In addition to the pileup ID requirement, jet energy resolution (JER) corrections are applied to all AK4 jets. Application of this correction on all jets is observed to improve the jet modeling, especially at the region near  $|\eta| = 2.9$ . The effect

of JER corrections is shown in Fig. 3·1, where the  $\eta$  distribution is plotted for the second-highest  $p_T$  (subleading) jet in the event, with and without the JER corrections applied.

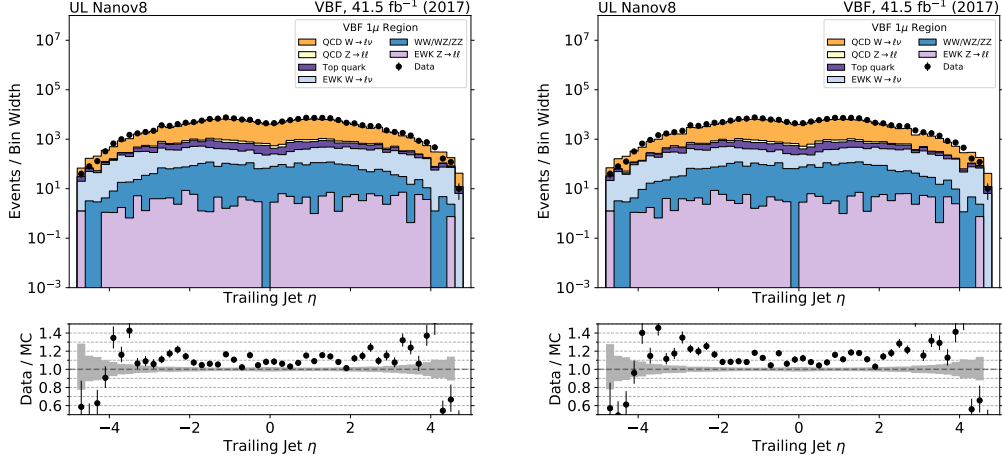


**Figure 3·1:** Subleading AK4 jet  $\eta$  distribution in single muon control region with JER corrections applied (left) and without JER corrections applied (right).

In addition, jet-lepton overlap cleaning is done by removing any AK4 PF jet that is within a cone of radius  $\Delta R = \sqrt{\Delta\eta^2 + \Delta\phi^2} = 0.4$  surrounding a lepton or a photon. Only lepton and photon candidates satisfying the object criteria described below are considered during the cleaning.

Lastly, if the leading or the subleading jet is found to be within the tracker coverage (i.e.  $|\eta| < 2.5$ ), the following requirement on the jet energy fractions are implemented to reduce the contributions from non-collision backgrounds:

- Charged hadron energy fraction  $> 0.1$
- Neutral hadron energy fraction  $< 0.8$

These additional requirements aid in rejecting mis-identified jets with spuriously low charged hadron fractions.

## b-tagged jets

Identifying jets that originate from a b-quark is important in this analysis, since a b-quark is not expected in the final state of the VBF  $H \rightarrow inv.$  signal, and vetoing events with b-jets allows to remove most of the backgrounds originating from top quark production.

In this analysis, jets with  $p_T > 20$  GeV and  $|\eta| < 2.4$  are identified as b-jets according to the DeepCSV algorithm [29]. A medium working point is adopted, corresponding to correctly identifying a b-jet with a probability of 80%, and misidentifying a light-flavor jet with a probability of 10%. This working point corresponds to the value of DeepCSV tagger to be greater than 0.4506 in 2017, and 0.4168 in 2018.

### 3.1.2 Missing transverse momentum and recoil

The vector  $\vec{p}_T^{miss}$  is defined as the imbalance in the transverse momentum of all particles that interact with the detectors. Due to momentum conservation in the plane transverse to the beam axis,  $\vec{p}_T^{miss}$  corresponds to the transverse momentum that is carried by undetected particles such as neutrinos. Practically,  $\vec{p}_T^{miss}$  is computed as the negative of the vectorial sum of transverse momenta of all Particle Flow (PF) candidates and is therefore also referred to as PF  $\vec{p}_T^{miss}$ . The magnitude of the  $\vec{p}_T^{miss}$  is referred to as  $p_T^{miss}$ .

Minimum energy thresholds in the calorimeters, inefficiencies in the tracker, non-linearity of the response of the calorimeter for hadronic particles can lead to an over- or underestimation of  $p_T^{miss}$ . The bias on the  $p_T^{miss}$  measurement is reduced by propagating the effect of the jet energy corrections introduced in section 3.1.1 according to

$$\vec{p}_T^{miss}(\text{corr}) = \vec{p}_T^{miss} - \sum_{\text{jets}} (\vec{p}_{\text{T,jet}}(\text{corr}) - \vec{p}_{\text{T,jet}}), \quad (3.1)$$

where the “corr” refers to the scale energy corrected measurements of the related objects.

This correction for  $\vec{p}_T^{\text{miss}}$  uses jet energy scale corrections for all corrected jets with  $p_T > 15 \text{ GeV}$  that have less than 90% of their energy deposited in the ECAL. Furthermore, if a muon is found in a jet, its 4-momentum is subtracted from the 4-momentum of the jet when performing the correction and is added back to a corrected object.

Since  $H \rightarrow \text{inv.}$  signal events in this analysis contain only jets and no other reconstructed candidates,  $\vec{p}_T^{\text{miss}}$  is equivalent to the total hadronic momentum in the event. For the leading  $Z(\nu\nu) + \text{jets}$  and  $W(\ell\nu) + \text{jets}$  backgrounds (described in Sec. 3.4.1), this corresponds to the transverse momentum of the  $Z$  or  $W$  boson. To mimic this behavior in the control regions of this analysis, the transverse momentum of the hadronic recoil  $\vec{U}$ , defined as the vectorial sum of the transverse momenta of all particles except the vector boson (or its decay products) is used. The variable is computed as

$$\vec{U} = \vec{p}_T^{\text{miss}} + \sum_{i \in \text{leptons, photons}} \vec{p}_T^i \quad (3.2)$$

where the sum takes into account the leptons and photons used to define the respective control region. All control regions defined in this analysis are described in Sec. 3.4. The uncertainty of  $\vec{p}_T^{\text{miss}}$  has a strong dependence on the event topology. Therefore, the uncertainty on  $\vec{p}_T^{\text{miss}}$  is often factorized into its components of jets, leptons and unclustered energy. Each sub-component is then varied within its scale and resolution uncertainty.

In addition to the events with genuine  $\vec{p}_T^{\text{miss}}$ , such as  $Z(\nu\nu) + \text{jets}$ , anomalous high- $\vec{p}_T^{\text{miss}}$  events can also appear due to various phenomena. In the ECAL, spurious deposits may appear due to particles striking sensors in the ECAL photodetectors,

or from real showers with non-collision origins such as those caused by beam halo particles. ECAL dead cells can cause real energy to be missed, again leading to a spurious imbalance. In the HCAL, spurious energy can arise due to noise in the hybrid photodiode and readout box electronics, as well as direct particle interactions with the light guides and photomultiplier tubes of the forward calorimeter. A number of filters has been developed by the POG/DPG groups to identify and suppress anomalous high  $p_T^{miss}$  events [1]. The recommended filters are listed in Tab. 3.1 and are applied in the analysis.

**Table 3.1:** The  $p_T^{miss}$  filters recommended by the JME POG [1]. The recommendations apply to both 2017 and 2018. Except for the bad super cluster filter (“EE badSC”), all filters are applied both in data and simulation (MC).

Filter	Name in input dataset	Applied in data (MC)
Primary vertex filter	Flag_goodVertices	✓(✓)
Beam halo filter	Flag_globalSuperTightHalo2016Filter	✓(✓)
HBHE noise filter	Flag_HBHENoiseFilter	✓(✓)
HBHEiso noise filter	Flag_HBHENoiseIsoFilter	✓(✓)
ECAL TP filter	Flag_EcalDeadCellTriggerPrimitiveFilter	✓(✓)
Bad PF Muon Filter	Flag_BadPFMuonFilter	✓(✓)
EE badSC noise filter	Flag_eeBadScFilter	✓(✗)
ECAL bad calibration filter update	Flag_ecalBadCalibFilter	✓(✓)

### 3.1.3 Leptons

#### Muons

Muons are reconstructed by combining information from silicon tracker detector and the muon system [20]. Requirements for a good-quality muon object include the fit

quality of the muon track, and its consistency with the primary vertex in the event. All muons considered in this analysis have  $p_T > 10 \text{ GeV}$  and  $|\eta| < 2.4$  (i.e. they are reconstructed within the tracker range).

Two types of muon identification are used for this analysis, loose and tight muons [30, 31]. Loose muon identification is used to identify muons in the signal region and veto them. Tight muon identification, on the other hand, has more strict quality conditions and are used to identify good quality muons in  $W(\mu\nu)$  and  $Z(\mu\mu)$  control regions.

Loose muon objects must pass the following requirements [30]:

- Candidate must be reconstructed as a PF muon
- Are either a Global or Tracker Muon

Tight muons pass all the requirements of loose muons, together with passing these additional muon quality requirements [31]:

- $p_T > 20 \text{ GeV}$
- Normalized  $\chi^2$  of the muon track fit  $< 10$
- At least one Muon Chamber hit must be included in the muon track fit
- Muon segments required in at least two muon stations
- The muon track must have transverse impact parameter  $d_{xy} < 2 \text{ mm}$  w.r.t. the primary vertex
- The longitudinal distance of the tracker track w.r.t. the primary vertex must be  $d_z < 5 \text{ mm}$
- Number of pixel hits  $> 0$

- Cut on number of tracker layers with hits  $> 5$

In addition to the requirements listed above, an energy isolation requirement is imposed on the muons. An isolation variable is computed based on the sum of energies of nearby PF candidates, within  $\Delta R < 0.4$  of the muon. This isolation variable is then used to select muons that are relatively isolated from other physical objects. This isolation variable is required to be less than 0.25 for loose muons, and less than 0.15 for tight muons.

## Electrons

Electrons are reconstructed using the information from the tracker and the ECAL detector [19]. All electrons considered in this analysis have  $p_T > 10 \text{ GeV}$  and  $|\eta| < 2.5$ .

Similar to the case of muons, two types of identification are used for electrons, which are labeled as veto and tight electrons. Veto electrons are used to identify electrons in the signal region and veto events containing such electrons. Tight electrons, which have tighter quality cuts, are used to identify electrons in  $W(e\nu)$  and  $Z(ee)$  control regions.

The quality requirements for veto and tight electron objects are different for electrons reconstructed in the barrel region ( $|\eta| < 1.479$ ) and in the endcap region ( $|\eta| > 1.479$ ). The details of the quality requirements are listed in Tables 3.2, 3.3, 3.4 and 3.5.

In addition to the requirements listed in the tables above, electrons are cross-cleaned against the muons within  $\Delta R < 0.3$ .

## Taus

Hadronically decaying  $\tau$  leptons are required to pass identification criteria using the DeepTau algorithm [32]. In addition,  $\tau$  candidates are required to be isolated from other activity in the event. The isolation requirement is computed by summing the

Quantity	Requirement
Full 5x5 $\sigma_{i\eta i\eta}$	$< 0.0126$
$ \Delta\eta_{\text{seed}} $	$< 0.00463$
$ \Delta\phi_{\text{In}} $	$< 0.148$
H/E	$< 0.05 + 1.16/E_{\text{SC}} + 0.0324\rho/E_{\text{SC}}$
Relative Isolation With EA	$< 0.198 + 0.506/p_T$
$ 1/E - 1/p $	$< 0.209$
Expected Missing Inner Hits	$\leq 2$
Pass conversion veto	yes

**Table 3.2:** Requirements used to define veto electrons in the barrel region ( $|\eta| < 1.479$ ).

Quantity	Requirement
Full 5x5 $\sigma_{i\eta i\eta}$	$< 0.0104$
$ \Delta\eta_{\text{seed}} $	$< 0.00255$
$ \Delta\phi_{\text{In}} $	$< 0.022$
H/E	$< 0.026 + 1.15/E_{\text{SC}} + 0.0324\rho/E_{\text{SC}}$
Relative Isolation With EA	$< 0.0287 + 0.506/p_T$
$ 1/E - 1/p $	$< 0.159$
Expected Missing Inner Hits	$\leq 1$
Pass conversion veto	yes

**Table 3.3:** Requirements used to define tight electrons in the barrel region ( $|\eta| < 1.479$ ).

Quantity	Requirement
Full 5x5 $\sigma_{inj\eta}$	< 0.0457
$ \Delta\eta_{seed} $	< 0.00814
$ \Delta\phi_{In} $	< 0.19
H/E	$< 0.05 + 2.54/E_{SC} + 0.183\rho/E_{SC}$
Relative Isolation With EA	$< 0.203 + 0.963/p_T$
$ 1/E - 1/p $	< 0.132
Expected Missing Inner Hits	$\leq 3$
Pass conversion veto	yes

**Table 3.4:** Requirements used to define veto electrons in the endcap region ( $|\eta| > 1.479$ ).

Quantity	Requirement
Full 5x5 $\sigma_{inj\eta}$	< 0.0353
$ \Delta\eta_{seed} $	< 0.00501
$ \Delta\phi_{In} $	< 0.0236
H/E	$< 0.0188 + 2.06/E_{SC} + 0.183\rho/E_{SC}$
Relative Isolation With EA	$< 0.0445 + 0.963/p_T$
$ 1/E - 1/p $	< 0.0197
Expected Missing Inner Hits	$\leq 1$
Pass conversion veto	yes

**Table 3.5:** Requirements used to define tight electrons in the endcap region ( $|\eta| > 1.479$ ).

$p_T$  of the charged PF candidates and PF photon candidates within an isolation cone of  $\Delta R = 0.5$ , around the tau candidate direction. The “VVLoose” isolation working point [33] is employed in this analysis for tau candidates with  $p_T > 20$  GeV within  $|\eta| < 2.3$ .  $\tau$  candidates within  $\Delta R = 0.4$  of an identified veto electron or loose muon are rejected.

### 3.1.4 Photons

Photon candidates are reconstructed from energy deposits in the ECAL using algorithms that constrain the clusters to the size and shape expected from a photon [34]. The identification of the candidates is based on shower-shape and isolation variables. For isolated photons, scalar sums of the  $p_T$  of PF candidates within a cone of  $\Delta R < 0.3$  around the photon candidate are required to be below the bounds defined. Only the PF candidates that do not overlap with the electromagnetic shower of the candidate photon are included in the isolation sums.

Similar to electrons and muons, two candidate definitions are employed for photons. Loose photons are used to reject events with reconstructed photons in the signal region. These photons are required to pass the EGamma POG loose identification criteria [35], have  $p_T > 15$  GeV and be within  $|\eta| < 2.5$ . The exact identification criteria for loose photons in barrel and endcap are summarized in Tables 3.6 and 3.7, respectively. Tight photons are used to identify photon objects in the dedicated photon control region. These photons are explicitly required to be in the barrel ( $|\eta| < 1.479$ ), and have  $p_T > 215$  GeV. The identification criteria for tight photons are summarized in Table 3.8.

### Photon purity

Photons are reconstructed from ECAL clusters, and can be discriminated from other sources of ECAL deposits due to the properties of the cluster, as well as their lack

Variable	Selection
	Barrel ( $ \eta  < 1.479$ )
Full 5x5 $\sigma_{inj\eta}$	$< 0.0106$
H/E	$< 0.04596$
charged hadron isolation	$< 1.694$
neutral hadron isolation	$< 24.032 + 0.01512 \times p_T + 2.259 \times 10^{-5} \times p_T^2$
photon isolation	$< 2.876 + 0.004017 \times p_T$
Conversion safe electron veto	Yes

**Table 3.6:** Loose photon identification criteria for photons in the barrel. These photons must also have  $p_T > 15 \text{ GeV}$ .

Variable	Selection
	Endcap ( $1.479 <  \eta  < 2.5$ )
Full 5x5 $\sigma_{inj\eta}$	$< 0.0272$
H/E	$< 0.0590$
charged hadron isolation	$< 2.089$
neutral hadron isolation	$< 19.722 + 0.0117 \times p_T + 2.3 \times 10^{-5} \times p_T^2$
photon isolation	$< 4.162 + 0.0037 \times p_T$
Conversion safe electron veto	Yes

**Table 3.7:** Loose photon identification criteria for photons in the endcap. These photons must also have  $p_T > 15 \text{ GeV}$ .

Variable	Selection
	Barrel
Full 5x5 $\sigma_{inj\eta}$	$< 0.01015$
H/E	$< 0.02197$
charged hadron isolation	$< 1.141$
neutral hadron isolation	$< 1.189 + 0.01512 \times p_T + 2.259 \times 10^{-5} \times p_T^2$
photon isolation	$< 2.08 + 0.004017 \times p_T$
Conversion safe electron veto	Yes

**Table 3.8:** Tight photon identification criteria. The criteria are only given for the barrel region since endcap photons are not taken into account.

of other associated signatures such as tracks or HCAL deposits. This discrimination is not perfect, however, and in some cases, non-photon objects will incorrectly be

identified as photons, which in this text are also referred to as “fake photons”. The leading source of fake photons is QCD production of multijet events, where a jet is misidentified as a photon. The QCD process is relevant mainly because of its large cross-section, which yields non-negligible contributions to the photon selection even if the per-jet probability of misreconstruction is small.

To estimate the fake contribution to the photon control region, a purity measurement is performed. The photon purity is defined as the fraction of reconstructed photons that is actually due to an isolated photon from the hard scattering event, as opposed to a fake. The purity is obtained from a template fit to the distribution of the  $\sigma_{i\eta i\eta}$  variable in data, where  $\sigma_{i\eta i\eta}$  variable represents the width of the ECAL shower in the  $\eta$  direction. Due to the different shower behavior of photons and hadrons, the  $\sigma_{i\eta i\eta}$  distribution shows characteristically different behavior between these two classes of reconstructed photons: Real photons show a large peak with a cut-off at around  $\sigma_{i\eta i\eta} \approx 0.01$ , while fake photons will have a smaller peak (stemming from actual photons inside jets), and an additional non-peaking bulk region at larger  $\sigma_{i\eta i\eta}$  (stemming from hadrons interacting in the ECAL). The inputs to the fit are defined as follows:

- Photons in data are selected by applying the same identification criteria as for the tight selection defined above, with the exception of the  $\sigma_{i\eta i\eta}$  requirement. By removing this requirement, the full  $\sigma_{i\eta i\eta}$  distribution can be observed.
- A real photon template is obtained from  $\gamma +$  jets Monte Carlo (MC) simulation. The same identification criteria are applied as in data.
- A fake photon template is obtained from data. In this case, the identification criteria are modified by requiring that at least one of the isolation criteria is not passed. Therefore, the photons in this template represent reconstructed photons inside jets, (i.e. “fake photons”).

The templates are derived in separate bins of the photon  $p_T$  and the measurement is performed separately for 2017 and 2018. Events are selected using the following criteria:

- At least one jet with  $p_T > 100$  GeV and  $|\eta| < 2.4$ , which is not overlapping with a photon of interest.
- The event must pass the HLT\_Photon200 trigger, which requires a photon with  $p_T > 200$  GeV to be reconstructed at the HLT level.
- The event must pass the offline MET filters, and have  $p_T^{miss} < 60$  GeV.

The fits are shown in Figs. 3·2 and 3·3. The resulting impurity values as a function of photon  $p_T$  are shown in Fig. 3·4. While the fits are performed in the range of  $0.04 < \sigma_{i\eta i\eta} < 0.15$ , the purity is evaluated only taking into account the contributions with  $\sigma_{i\eta i\eta} < 0.01$ , which is the requirement posed in the identification criteria used in the analysis (see Tab. 3.8). Overall, good fit performance is observed and the impurity is found to range between 1% and 4%, with a decreasing trend with increasing photon  $p_T$ . Residual differences between the best fit and the data appear because the template shapes do not match the data shapes perfectly. To take this effect into account, the measurement is repeated with four alternative binning schemes that range from being very fine to very coarse and are shown in Fig. 3·5. By varying the binning choice, the effect of shape differences can be amplified or mitigated, and its impact on the final impurity values can be tested. The spread of the resulting values per bin is found to be small and a 25% uncertainty is assigned to the impurity and thus the QCD background estimate. For application in the analysis, the nominal impurity values are interpolated using an exponential function fit.

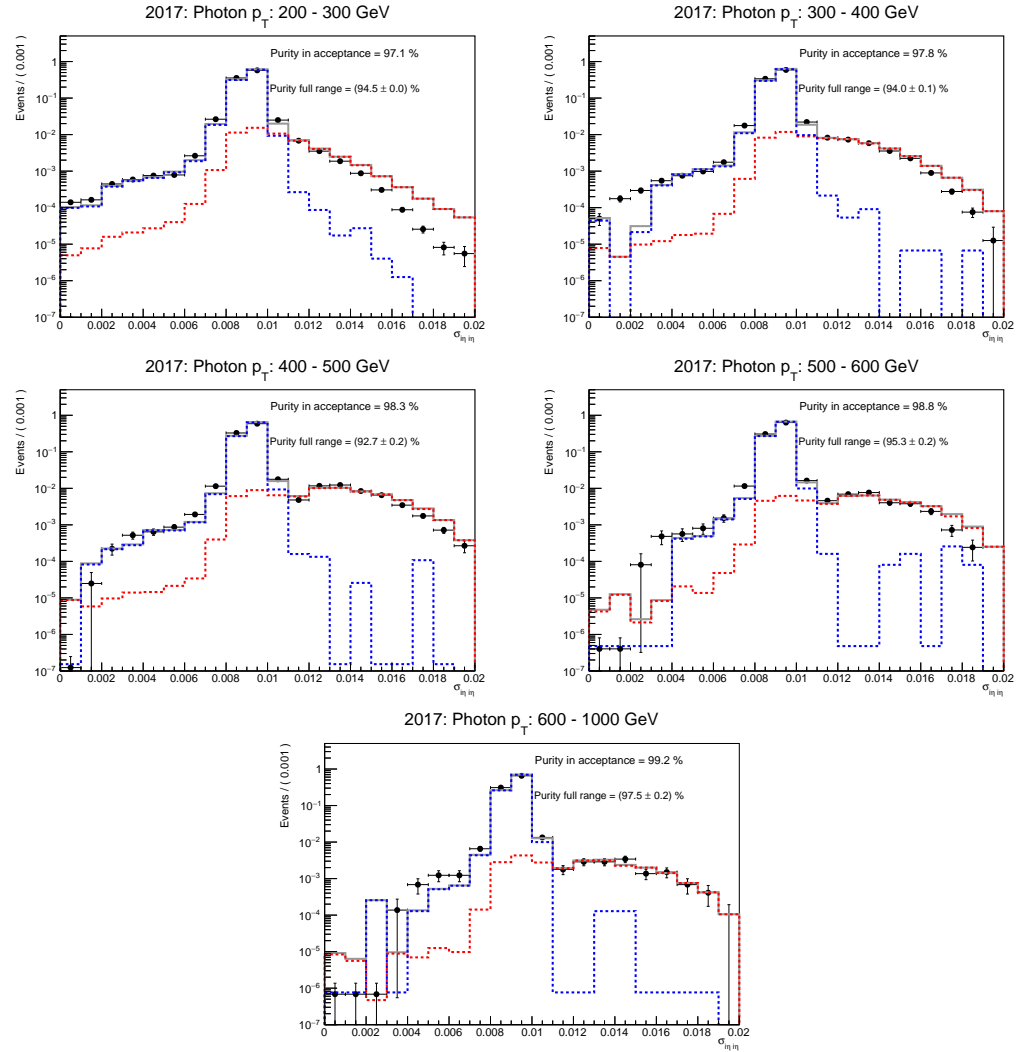


**Figure 3.2:** Template fits used to determine the photon purity in the 2017 dataset. The fits are shown in bins of photon  $p_T$ , increasing from left to right and top to bottom. The “nominal” binning scheme is used.

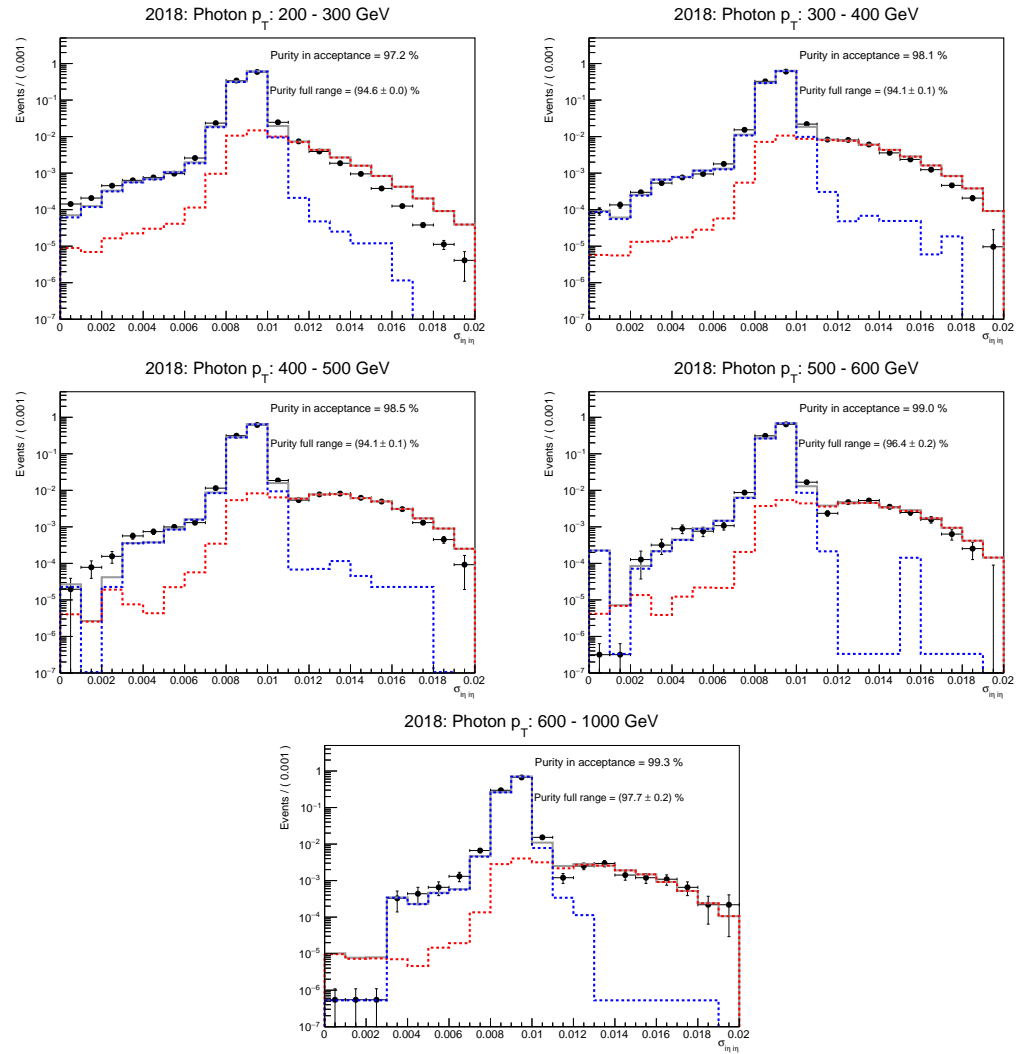


**Figure 3.3:** Template fits used to determine the photon purity in the 2018 dataset. The fits are shown in bins of photon  $p_T$ , increasing from left to right and top to bottom. The “nominal” binning scheme is used.

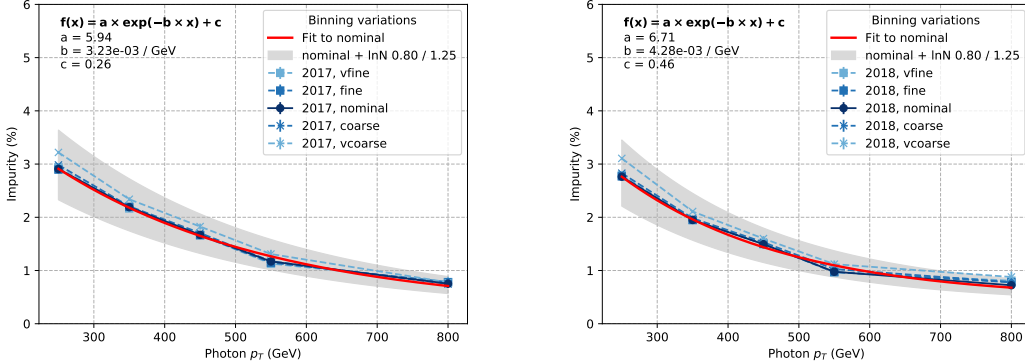


**Figure 3.4:** Photon impurity as a function of photon  $p_T$  for 2017 (left) and 2018 (right). The measured values for different binning choices are shown in the blue shaded lines and markers. The nominal result is interpolated using an exponential function fit, which is shown in the red solid line. The gray band represents a 25% uncertainty around the interpolated nominal result.

## 3.2 Reweighting of simulated events

Simulated signal and background samples can differ from collision data due to various effects. Therefore, reweighting of simulated events is necessary to correct simulated samples for these effects. The reweighting procedure for different types of effects are outlined in this section.

### 3.2.1 Trigger efficiency reweighting

#### $p_{T,no-\mu}^{miss}$ and $H_{T,no-\mu}^{miss}$ triggers

In this analysis, the collision data for signal region,  $W(\mu\nu)$  and  $Z(\mu\mu)$  control regions (see Sec. 3.4) are collected using high-level triggers that require  $p_{T,no-\mu}^{miss} > 120$  GeV and  $H_{T,no-\mu}^{miss} > 120$  GeV. The fact that muon momenta are subtracted from the  $p_T^{miss}$  and  $H_T^{miss}$  calculations allow these triggers to be used both for collecting data in signal region (high  $p_T^{miss}$ ), and muon control regions (high  $p_T$  muons). To simplify the discussion, this trigger will be referred to as the ‘‘MET trigger’’ in this text.

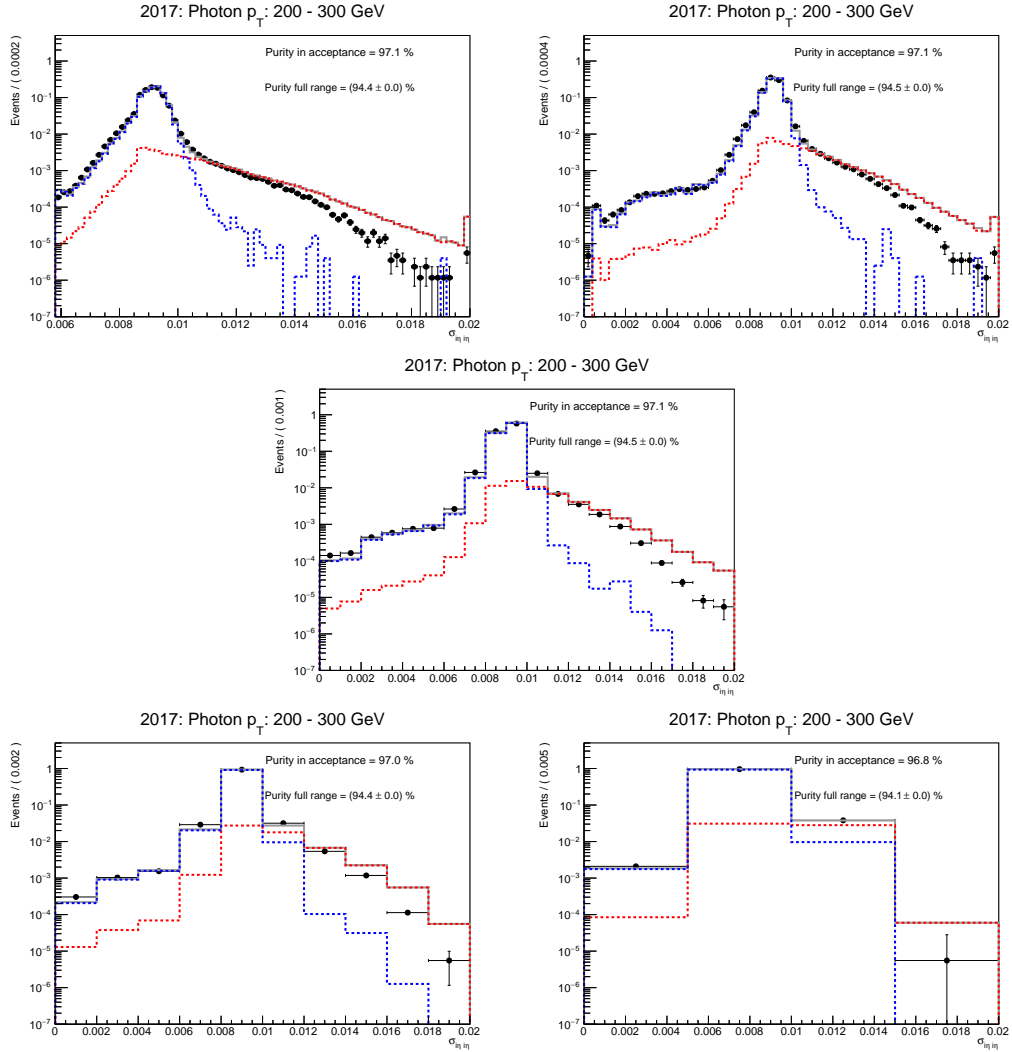


**Figure 3.5:** Comparison of binning schemes used to define a systematic uncertainty on the purity measurement. In all cases, the  $200 < p_T < 300 \text{ GeV}$  bin of the 2017 data set is shown. The binning choices are very fine and fine (top row), nominal (middle row) and coarse and very coarse (bottom row).

The efficiency of MET trigger is calculated as a function of the recoil, where recoil refers to the vectorial sum of the transverse momenta of all particles except the vector boson, as defined in Eq. 3.2. The efficiencies are computed separately for data and MC, and the ratio between those two measurements are used to derive scale factors to correct the MC. The efficiency measurement procedure is described below.

The performance of the  $p_{T,no-\mu}^{miss} + H_{T,no-\mu}^{miss}$  triggers is measured using  $W(\mu\nu) + \text{jets}$  events. The events are selected from the data by requiring the `HLT_IsoMu27` trigger for 2017, and `HLT_IsoMu24` for 2018. In addition, the offline muon is required to be tightly-identified as defined in Sec. 3.1.3, and have  $p_T > 40$  GeV. The same requirements are also applied when selecting events from MC. The full set of selections required is listed below:

1. Event must have exactly one tightly-identified muon with  $p_T > 40$  GeV.
2. Veto on additional leptons, photons, b jets,  $\tau_{had}$  candidates.
3.  $\Delta\phi(jet, p_T^{miss}) > 0.5$  for the four leading jets with  $p_T > 30$  GeV.
4. (Calo  $p_T^{miss}$ - PF  $p_T^{miss}$ ) / recoil  $< 0.5$
5. Leading AK4 jet with  $p_T > 80$  GeV, passing the tight jet ID.
6. Subleading AK4 jet with  $p_T > 40$  GeV.
7.  $\Delta\eta_{jj} > 1.0$
8.  $\Delta\phi_{jj} < 1.5$

To understand the dependence of the efficiencies on the jet kinematics, the efficiencies in data and MC are measured separately for two cases: Events where the two highest- $p_T$  jets are both in the central region of the detector (i.e.  $|\eta| < 2.5$ ), and events where at least one jet is in the forward region ( $|\eta| > 2.5$ ).

To smooth out the fluctuations in efficiencies for each case, a sigmoid function is fit to both data and MC efficiency curves. The sigmoid function has three parameters and is written in the form  $f(x, a, b, c) = \frac{c}{1+e^{-a(x-b)}}$ . The factors for correcting the MC simulation are then calculated as the ratio of the best-fit sigmoid curves for data and MC. The efficiencies and resulting SFs are shown in Fig. 3·6. From Fig. 3·6, it can be seen that the scale factors are mostly  $\simeq 1$  for the analysis phase space (i.e. Recoil  $> 250 \text{ GeV}$ ).

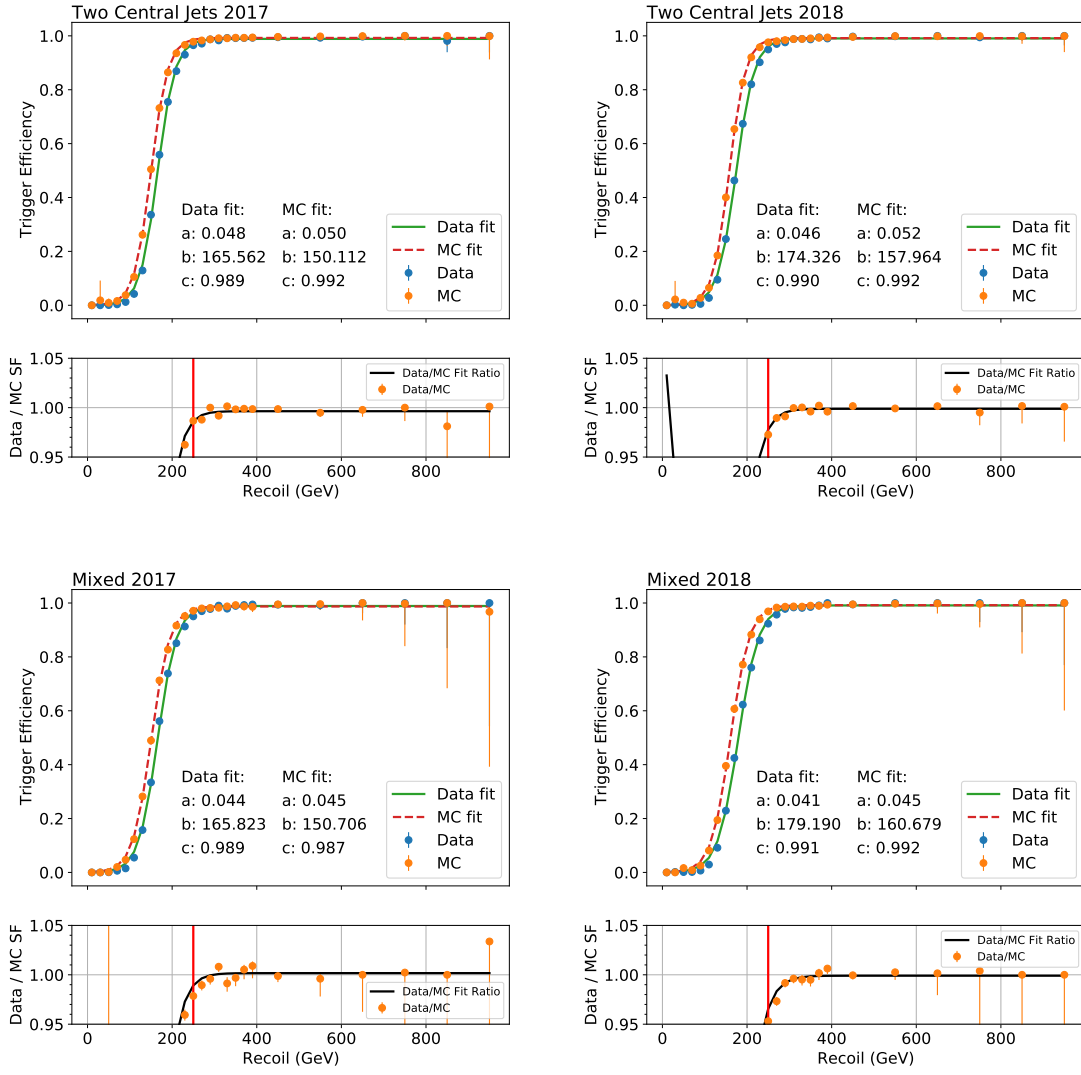


**Figure 3.6:** MET trigger efficiencies for data and MC, for events where the two VBF jets are both central (top) and where at least one jet is forward (bottom). Left column shows results with 2017 dataset, while the right column shows the results with 2018 dataset. To each efficiency curve, a sigmoid function with three parameters are fitted:  $f(x, a, b, c) = \frac{c}{1+e^{-a(x-b)}}$ . Resulting data/MC scale factors are shown in the bottom ratio pad for each case. The black line represents the ratio of two best-fit sigmoid functions, which is used as the correction factor to MC as a function of recoil.

## Photon trigger

The photon trigger efficiency is measured using events collected with HLT\\_PFHT1050 trigger, which was fully unprescaled in 2017 and 2018, meaning that all the events passing the trigger were saved to the disk.

Events are selected in the same way as for the photon control region in the analysis (see Sec. 3.4.6) except for the photon  $p_T$ , recoil,  $H_T$  and trigger requirements. To ensure an unbiased measurement, an offline  $H_T$  of at least 1.5 TeV is required, where  $H_T$  is calculated as:

$$H_T = \sum_{jet} p_T^{jet} \quad (3.3)$$

In Eq. 3.3, the sum runs over jets which pass the tight identification requirements and do not overlap with the selected photon within  $\Delta R < 0.4$ . The trigger efficiency  $\epsilon$  is then determined as:

$$\epsilon(\text{HLT\_Photon200}) = \frac{\text{Offline selection \&\& HLT\_PFHT1050 \&\& HLT\_Photon200}}{\text{Offline selection \&\& HLT\_PFHT1050}}$$

The resulting efficiency in data and  $\gamma+\text{jets}$   $H_T$ -binned simulation is shown in Fig. 3.7. In both data and simulation, the binned turn-on is fit using sigmoid functions, which are used to extract all further information. The trigger efficiencies in data and simulation are both found to be larger than 95% for photon  $p_T$  values of more than 230 GeV, which is used for the tight-identification requirement for photons reconstructed offline (see Sec. 3.1.4). The MC-to-data scale factor is evaluated as the ratio of the sigmoid functions in data and simulation and is found to be within 1% of unity consistent within an uncertainty of 1% with all individual points. In the analysis implementation, the scale factor is implemented as an event-by-event weight

based on the ratio of the sigmoid functions.

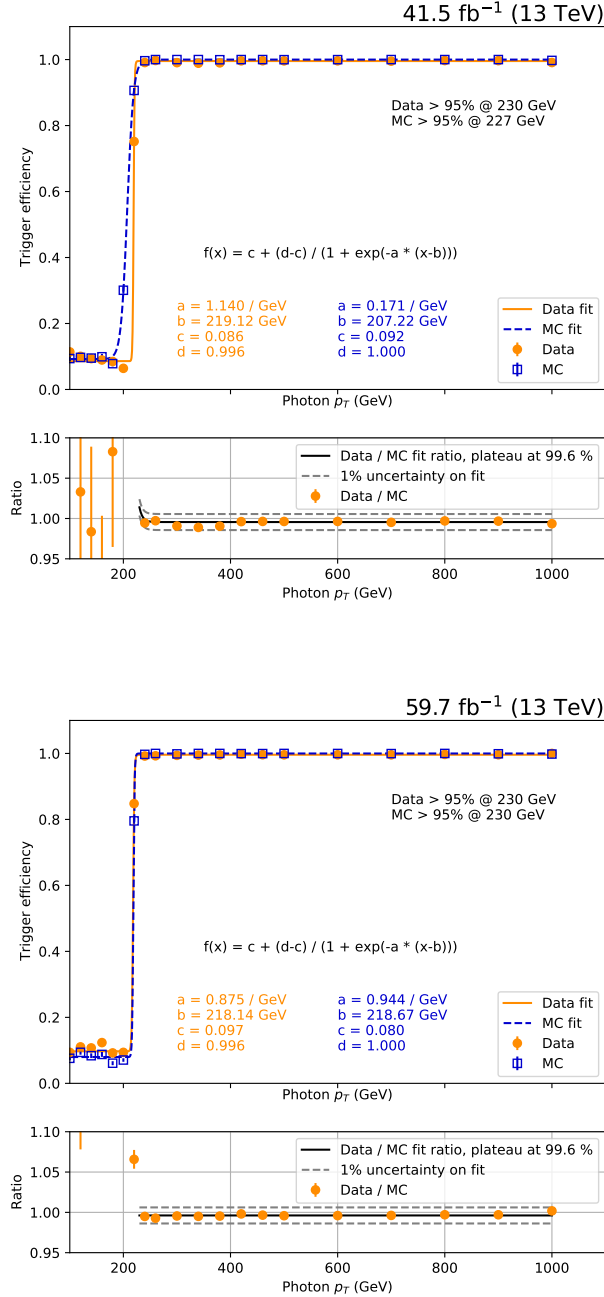


**Figure 3.7:** Efficiency of the HLT\_Photon200 trigger in data and  $H_T$ -binned  $\gamma+\text{jets}$  MC for 2017 (top) and 2018 (bottom) as a function of photon  $p_T$ . The orange and blue lines respectively represent sigmoid function fits to the turn-on in data and MC, with the fit function and best-fit parameter values given in the respectively colored labels. The bottom panel shows the ratio of the values measured in data over those in MC using orange markers. The solid black line corresponds to the ratio of the sigmoid fits to data and MC.

## Electron trigger

This analysis uses the logical OR of three triggers for the selection of events with electrons in the final state: `HLT_Ele35*` (`HLT_Ele32*`), `HLT_Ele115*` and `HLT_Photon200` for 2017 (2018) data. The OR of these three triggers is henceforth referred to as “the electron trigger”, to simplify the discussion. The higher-threshold triggers are advantageous in that they either do not contain isolation requirements (`HLT_Ele115`) or do not require a well-reconstructed track (`HLT_Photon200`), both of which enhance the selection efficiency at large electron  $p_T$ .

The efficiency of the electron trigger is measured in data and simulation using a “tag and probe” method. Tag electrons are required to pass a logical OR of all triggers considered here. Both the tag electron and the probe electron are required to pass the tight identification criteria used for the analysis selection (see Tables 3.3 and 3.5). In data, events are separated based on whether the probe electron passes the same trigger criteria as the tag. In both of these categories, separate fits to the distribution of the invariant mass of the tag-probe system are performed to extract the number of signal-like  $Z(ee)$  events in each category, and the efficiency is defined as the ratio of the number of passing signal events and the number of all signal events. The efficiency in simulation is measured in a Drell-Yan sample, and the signal event counts are defined by simply counting all events in the passing and failing categories. The MC-to-data scale factor is then defined as the ratio of the efficiency in data and that in simulation. The efficiency in data, as well as the scale factors are shown in Fig. 3.8. Note the appearance of steps in the efficiency at electron momenta of 115 and 200 GeV, which are a result of the addition of the high-momentum triggers to the logical OR expression.

As shown in the bottom panel of Fig. 3.8, the data to MC scale factors are derived from the two efficiency measurements from data and MC. Those correction factors

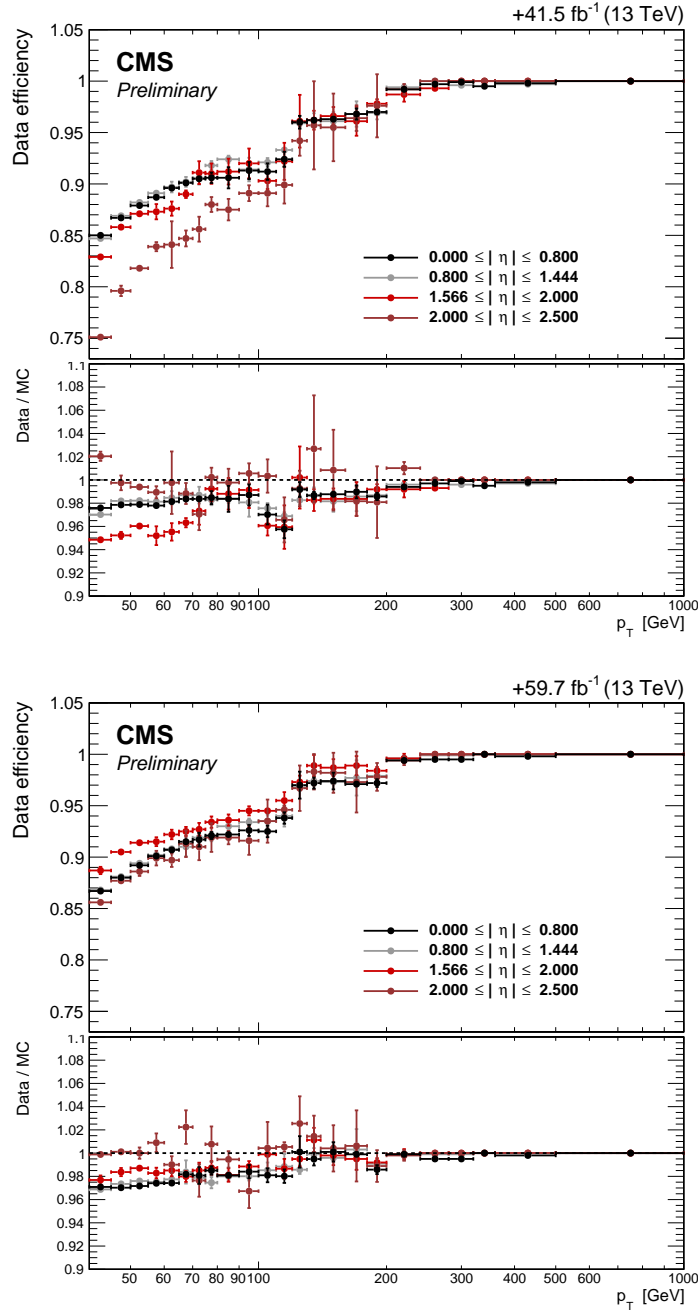


**Figure 3.8:** Efficiency of the OR of the three triggers used to select electron events for 2017 (top) and 2018 (bottom) as a function of the electron transverse momentum. The efficiency is shown for multiple regions of absolute electron pseudorapidity. In each plot, the upper panel shows the efficiency in data, while the lower panel shows the ratio of the efficiency in data and that in simulation.

are applied per-electron in the analysis to correct MC.

### 3.2.2 Pileup reweighting

The pileup (PU) conditions in the simulated samples are not identical to the ones observed in data, and a per-event reweighting is applied to remove the difference. The reweighting is performed by matching the true pileup distribution of each simulated sample with the pileup distribution in data. The pileup distribution in data is obtained through the pileupCalc tool, assuming a minimum bias cross section of  $69.2 \pm 4.6\%$  mb, following the recommendations in [36]. The true pileup distributions in data and simulation are shown in Fig. 3.9, which show the normalized number of events as a function of the number of reconstructed collision vertices. The distribution of the number of reconstructed vertices for  $W \rightarrow \mu\nu$  events before and after PU reweighting is shown in Fig. 3.10. The distribution of the event energy density  $\rho$  is shown in Fig. 3.11, again before and after PU reweighting. In terms of these two variables, it is observed that PU reweighting improves the agreement between data and MC.

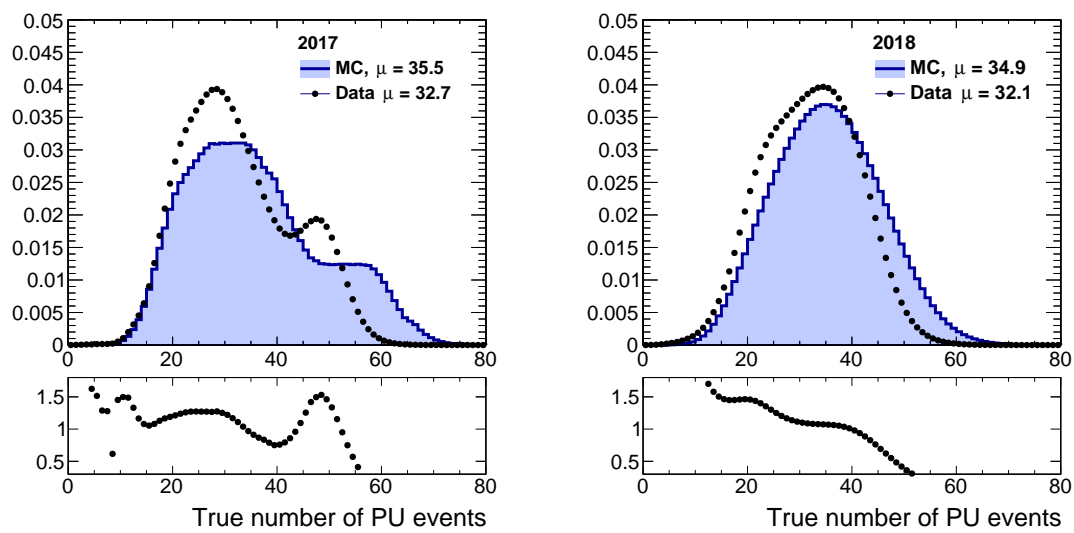


**Figure 3.9:** Distribution of the true number of PU events in data and simulation for 2017 (left) and 2018 (right). The distributions for data are extracted assuming a minimum bias cross section of 69.2 mb.

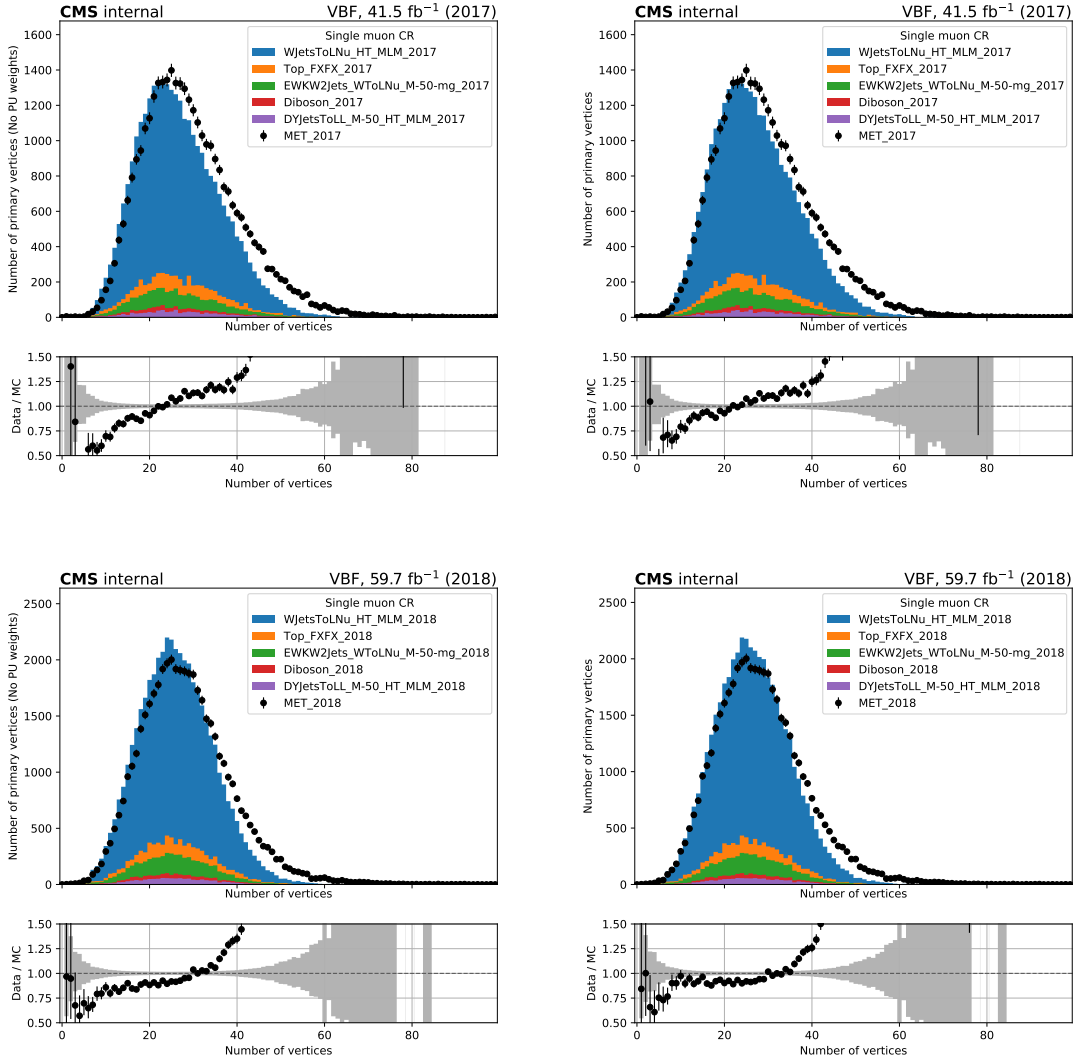


**Figure 3.10:** Distribution of the number of vertices in  $W \rightarrow \mu\nu$  events in data and simulation before pileup re-weighting (left) and after pileup reweighting (right). The Monte Carlo is normalized to the luminosity of 41.53 and 59.7  $\text{fb}^{-1}$ , respectively for 2017 and 2018.

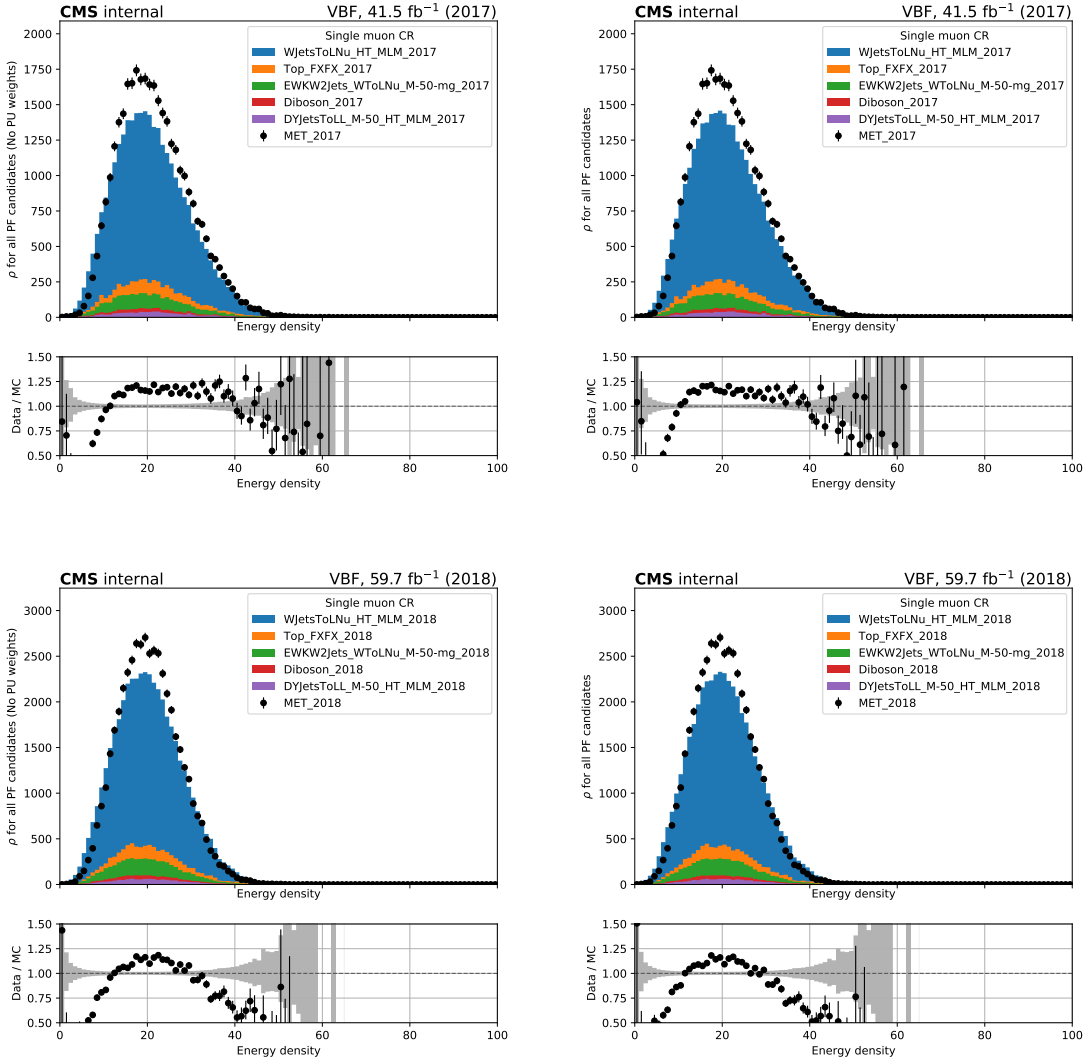


**Figure 3.11:** Distribution of the event energy density  $\rho$  in  $W \rightarrow \mu\nu$  events in data and simulation before pileup re-weighting (left) and after pileup reweighting (right). The Monte Carlo is normalized to the luminosity of  $41.53 \text{ fb}^{-1}$  and  $59.7 \text{ fb}^{-1}$ , respectively for 2017 and 2018.

### 3.2.3 Lepton identification efficiency reweighting

Data-to-MC scale factors are applied to events in the control regions to account for differences in the reconstruction, identification and isolation of leptons between data and MC. These data-to-MC scale factors are derived from the efficiencies that are measured for the electron and muon selections in bins of  $p_T$  and  $\eta$  in both data and MC. The muon reconstruction and identification scale factors are provided by the relevant POGs. Electron identification scale factors are measured using a tag-and-probe method, and the results are reviewed and approved by EGamma POG.

The reconstruction scale factors for electrons are shown in Fig. 3.12. The corresponding identification scale factors for veto and tight electrons are shown in Fig. 3.13, and include the effect of the isolation efficiency.

The identification scale factors for muons are shown in Fig. 3.14. Here, isolation scale factors are applied separately and are shown in Fig. 3.15. The corresponding corrections for muons are deemed negligible [37].

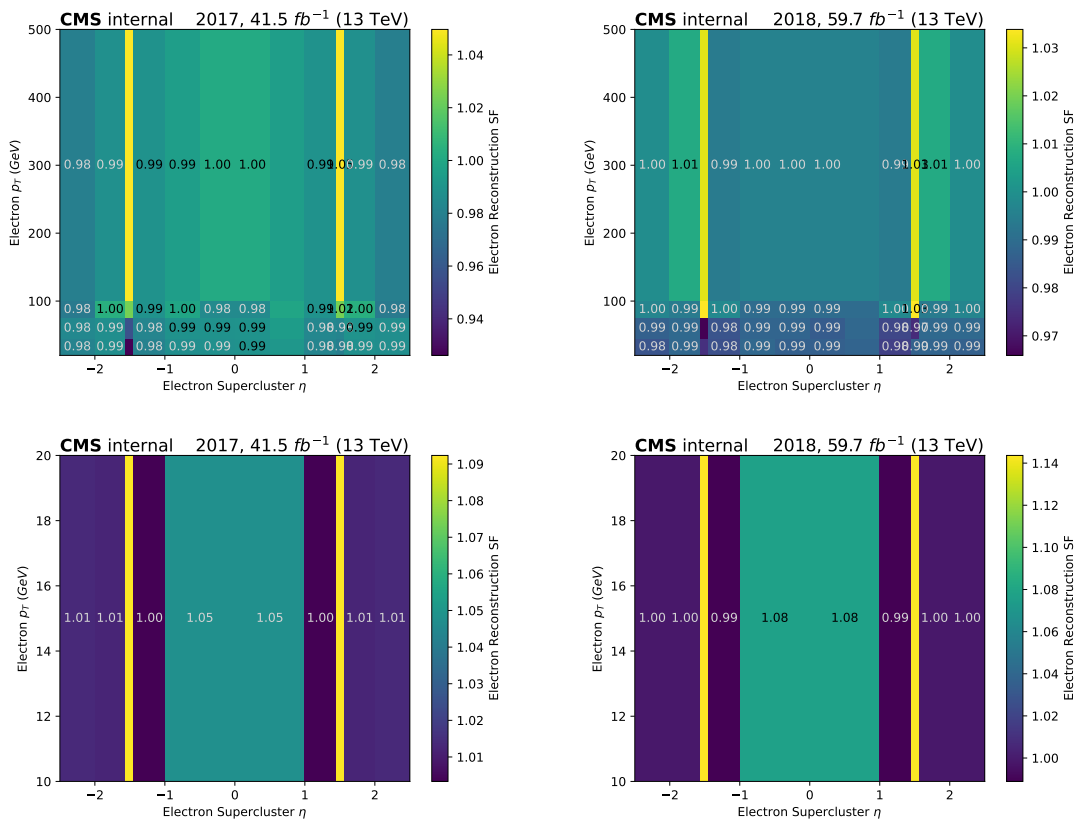


**Figure 3.12:** Scale factors for the reconstruction efficiency of electrons starting from a super cluster for 2017 (left) and 2018 (right), for electrons with  $p_T > 20$   $GeV$  (top) and  $p_T < 20$   $GeV$  (bottom).

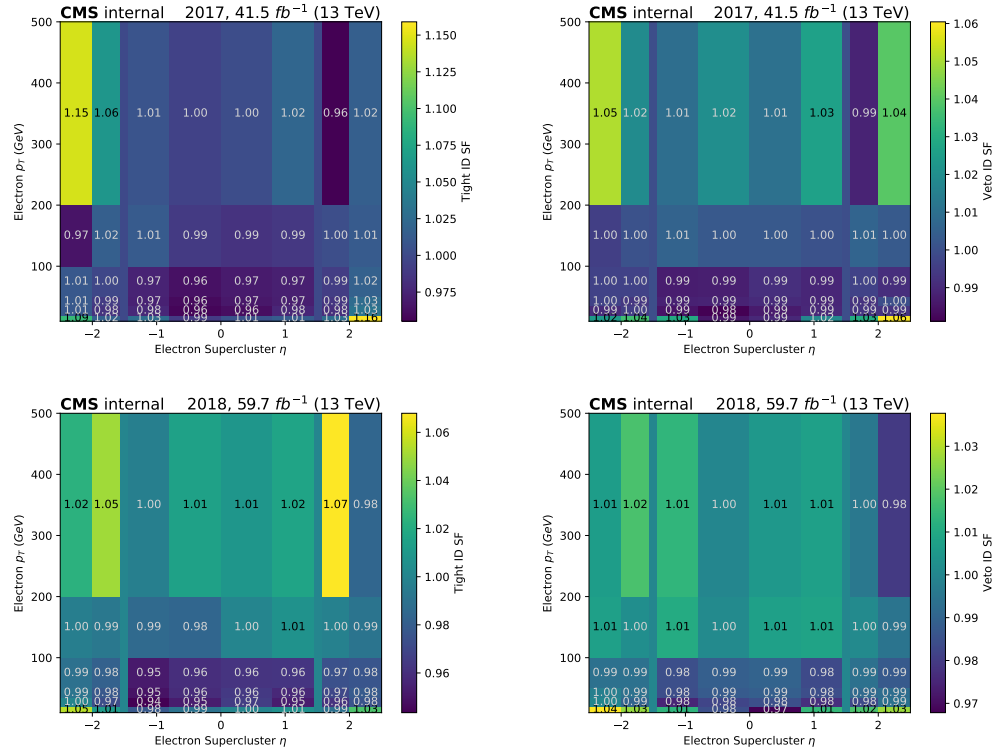


**Figure 3.13:** Scale factors for the identification efficiency of tight (left) and veto (right) electrons are shown for 2017 (top) and 2018 (bottom). The scale factors are provided in bins of electron  $p_T$  and  $\eta$ .

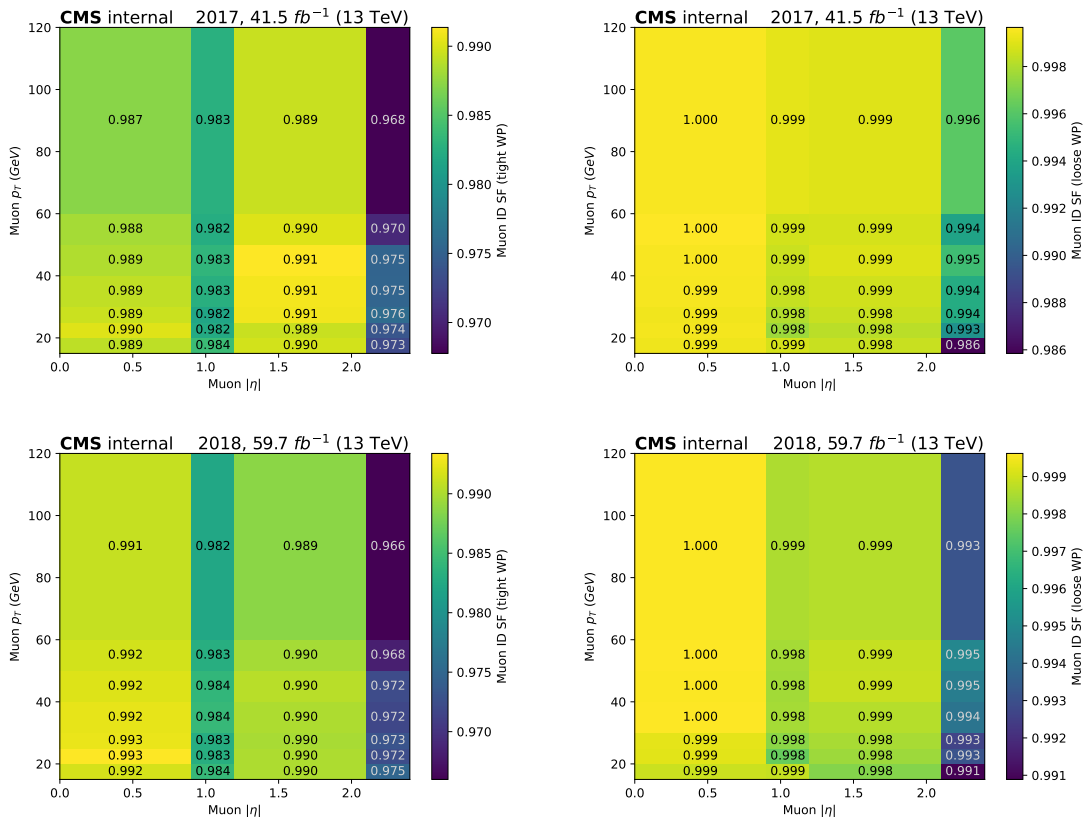


**Figure 3.14:** Scale factors for tight (left) and veto (right) muon identification are shown for 2017 (top) and 2018 (bottom). The scale factors are provided in bins of muon  $p_T$  and  $\eta$ .

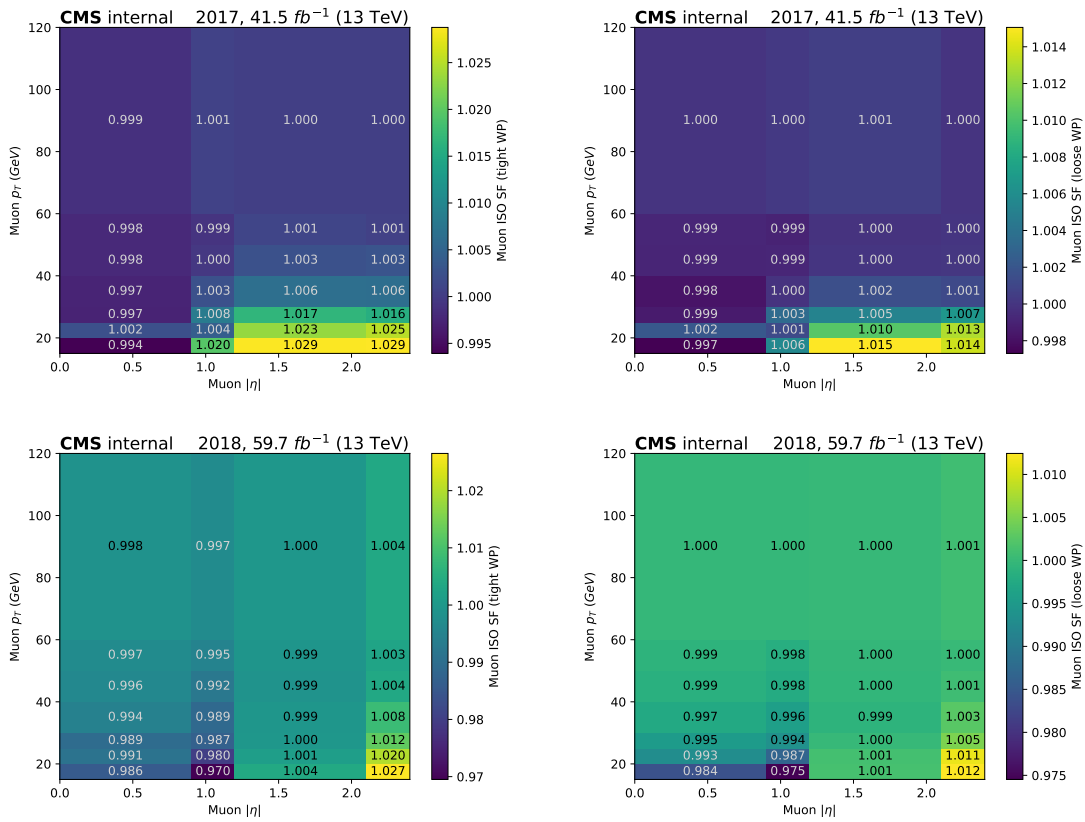


**Figure 3.15:** Scale factors for tight (left) and veto (right) muon isolation are shown for 2017 (top) and 2018 (bottom). The scale factors are provided in bins of muon  $p_T$  and  $\eta$ .

### 3.2.4 Lepton veto efficiency reweighting

To reduce contribution from  $W(\ell\nu) + \text{jet(s)}$  events in the analysis signal region (SR), events are rejected if they contain any identified charged lepton. However, due to finite efficiencies of the reconstruction and identification of these candidates,  $W(\ell\nu) + \text{jet(s)}$  events still contribute significantly. Furthermore, the differences in veto efficiency between data and MC need to be taken into account. For these purposes, the “veto-weight” method is used. In this method, simulated events in the SR are allocated a veto weight instead of being removed completely if they have charged lepton(s) in the final state. Such events with identified leptons can enter the SR with a veto weight dependent on the identification, isolation and reconstruction efficiency scale factors for the identified objects in the event. The veto weight  $\omega$  is calculated as:

$$\omega = \prod_{i \in \text{leptons}} (1 - SF_i) \quad (3.4)$$

where the product above runs over all identified veto leptons in the event (i.e. electrons, muons and taus).  $SF_i$  represents the total scale factor for the lepton  $i$ , which is the product of identification and isolation scale factors as described in Sec. 3.2.3. It can be observed that this method is equivalent to the ordinary method with hard-veto on events with leptons, as  $SF \approx 1$  for events with well identified leptons, making the event weight,  $\omega \approx 0$ , hence suppressing the contribution of the event in the SR.

The uncertainty on these veto weights are computed by varying the veto weights within their uncertainties and propagating the variation into the  $M_{jj}$  distribution in the SR. In Fig. 3.16, the impact of the veto weight corrections (compared to the hard lepton veto) on the  $W(\ell\nu) + \text{jets}$  process in the VBF signal region, and the uncertainty on the veto weights are shown. It can be observed that the correction coming from the veto weights is typically small ( $\ll 1\%$ ), and the uncertainties on the veto weights are small and uncorrelated with the invariant mass of two VBF jets,  $M_{jj}$ .

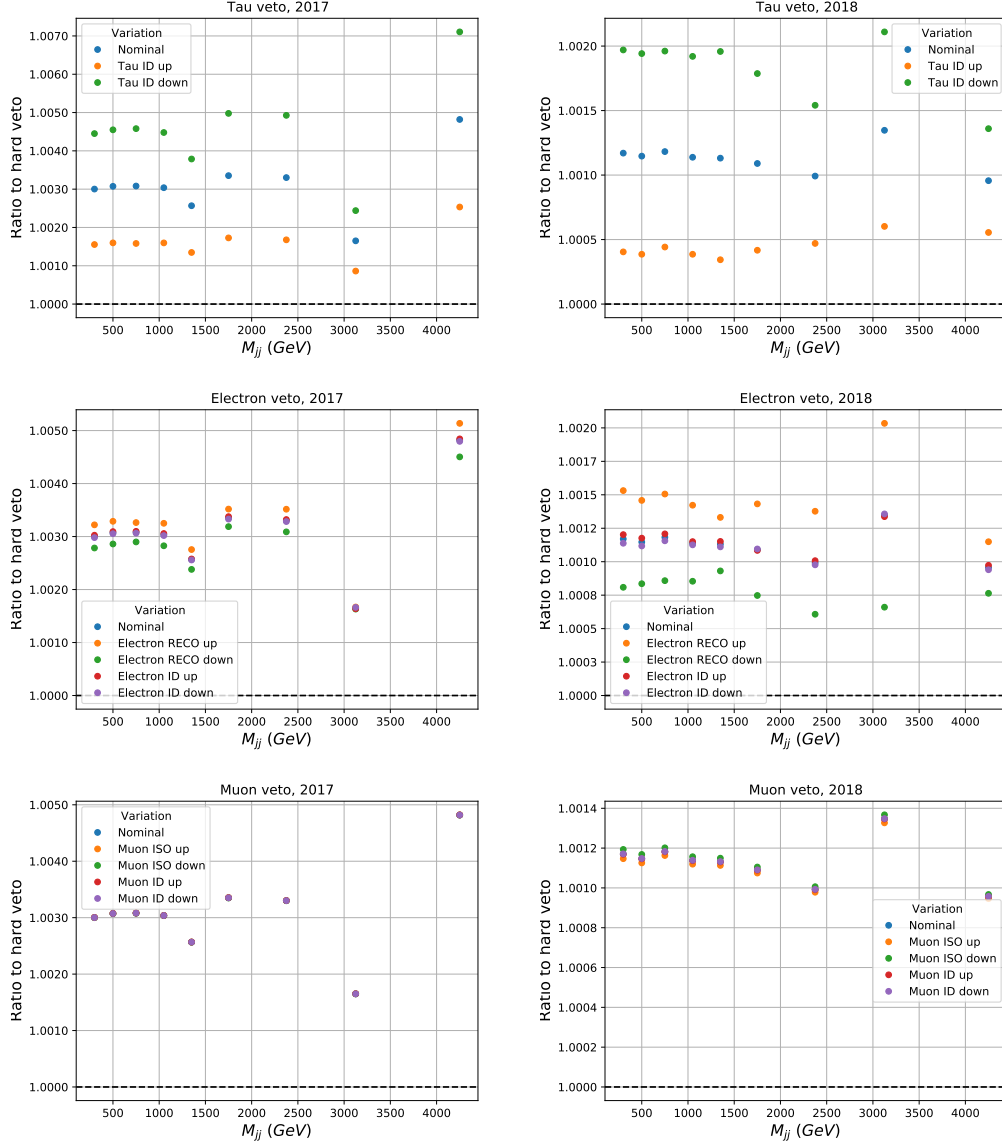


**Figure 3.16:** The impact of the veto weight corrections on  $W(\ell\nu) + \text{jets}$  process in the signal region. The correction with the nominal lepton veto weight and the uncertainties of the veto weight are shown, and the event yield ratio with the hard lepton veto case is plotted. The top row corresponds to the tau veto, middle row to electron veto, and last row corresponds to muon veto. Left and right columns represent 2017 and 2018 datasets, respectively.

### 3.2.5 Reweighting For HF Noise Cuts

As explained in Sec. 3.3.1, several cuts are implemented to reduce the contribution from mis-measured forward jets, reconstructed in the Forward HCAL (HF) detector (i.e.  $|\eta| > 3.0$ ). To account for the difference in the impact of these cuts in data and MC, a scale factor is applied to events in MC. These scale factors are derived by calculating the efficiency of these cuts on  $Z + jet$  and  $\gamma + jet$  events in data and MC, as a function of jet  $p_T$  and  $\eta$ , and taking the ratio of those two efficiencies.

The HF noise scale factors are applied for each HF jet in the event which would be taken into account for the HF cuts (i.e.  $p_T > 100$  GeV and  $\Delta\phi(j, p_T^{miss}) > 2.5$ ), as a function of  $p_T$  and  $\eta$  of the jet. The event weight is calculated by multiplying the individual jet weights:

$$\omega_{event} = \prod_{jet \in HF} \omega_{jet}(p_T, \eta) \quad (3.5)$$

The scale factors are shown in Fig. 3.17 for 2017 and 2018, together with the statistical uncertainties. For the statistically limited phase space, where  $SF = 0$ , the scale factor in the closest  $[p_T, \eta]$  bin is applied to the HF jet.

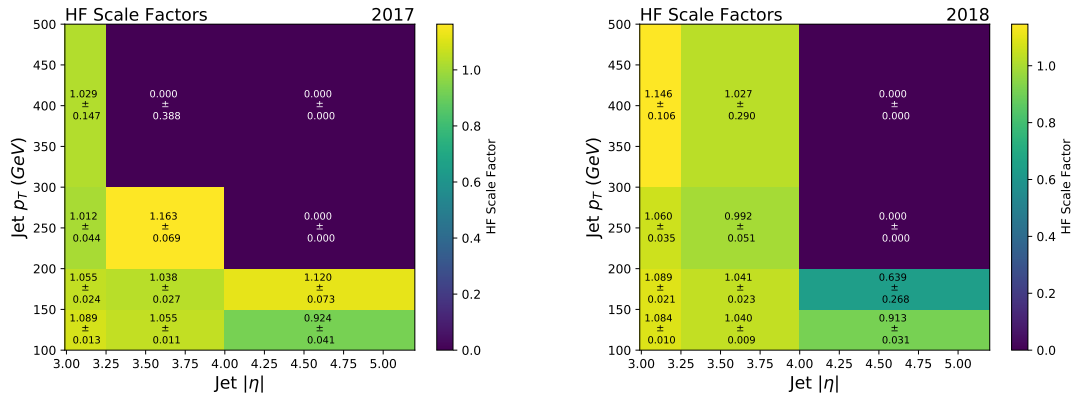


**Figure 3.17:** HF scale factors and their statistical uncertainties as a function of jet  $p_T$  and  $\eta$ , for 2017 (left) and 2018 (right). For the phase space with statistical limitations (i.e.  $SF = 0$ ), the scale factor in the closest  $[p_T, \eta]$  bin is applied to the HF jet.

### 3.2.6 Reweighting for ECAL pre-firing

Prefiring is a problem with the 2017 dataset that results from L1 trigger primitives in the ECAL endcap being incorrectly assigned to an earlier bunch crossing because of a timing issue. In most cases, the event to which the trigger primitives are now assigned to fail to pass the HLT selection and is discarded. This makes the event for which the trigger primitives were originally belonged to be discarded as well, which results in a loss of trigger efficiency. A solution has been developed by parametrizing the probability of a jet or photon in the event causing prefiring in terms of their  $p_T$  and  $\eta$ . In this analysis, the prefiring weights are applied based on the parametrization provided by the JME POG [38], and a central implementation provided in the NanoAOD-tools software is used [39]. In this implementation, a per-event prefiring weight is computed as:

$$\omega = 1 - P(\text{prefiring}) = \prod_{i=\text{photons,jets}} (1 - \epsilon_i^{\text{pref}}(p_T, \eta)) \quad (3.6)$$

where  $\epsilon_i^{\text{pref}}$  is the prefiring probability caused by a single photon or a jet.

The  $M_{jj}$  distributions with the nominal prefiring weight applied to simulation, together with the up and down variations of the prefiring weight are shown in Figs. 3.18 and 3.19. It can be observed that the uncertainty due to the prefiring weight increases with higher  $M_{jj}$ .

### 3.2.7 Higher-order reweighting

As will be detailed in Sec. 3.5.1, this analysis uses the ratios of  $V + \text{jets}$  distributions in signal and control regions to constrain the final background estimate for  $Z(\nu\nu) + \text{jets}$  and  $W(\ell\nu) + \text{jets}$  processes. As signal and control regions both have large statistical power, precise predictions of these ratios are necessary. To achieve this goal, next-to-leading-order (NLO) in QCD simulation samples are used for  $W(\ell\nu) + \text{jets}$  and

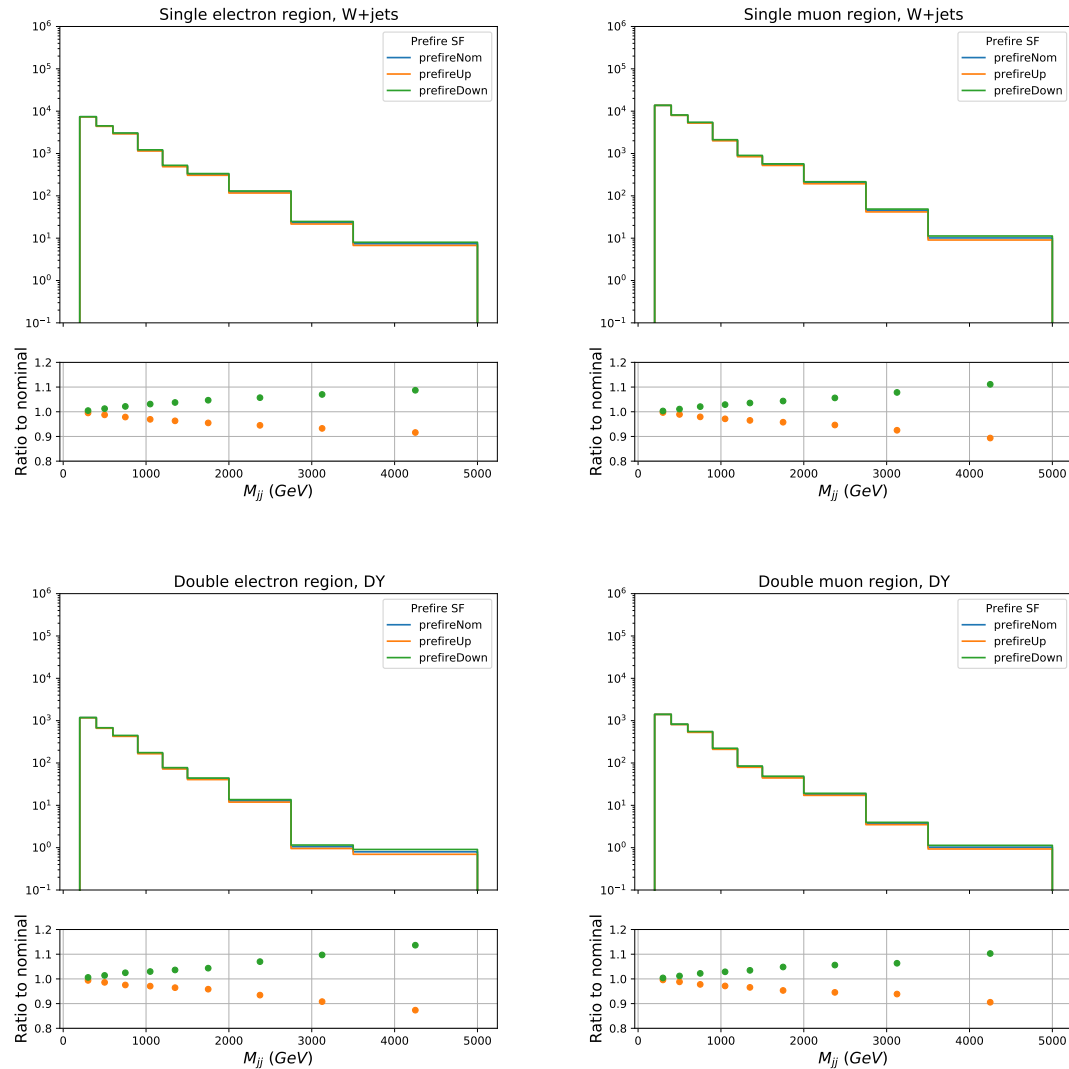


**Figure 3.18:** The  $M_{jj}$  distributions with the nominal prefireing weights and its variations are shown for  $W + \text{jets}$  simulation in single lepton CRs (top), and  $Z + \text{jets}$  simulation in double lepton CRs (bottom).

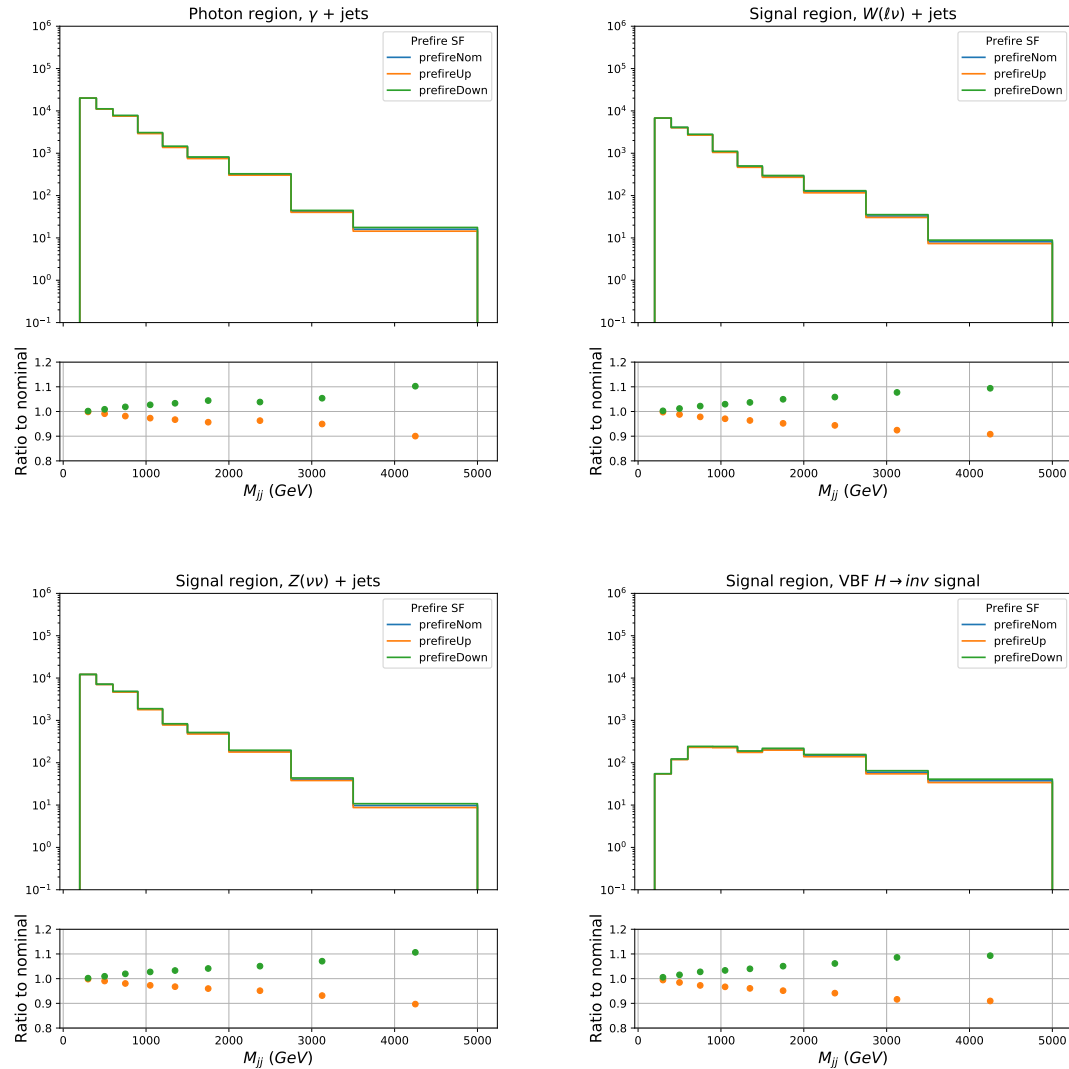


**Figure 3.19:** The  $M_{jj}$  distributions with the nominal prefiring weights and its variations are shown for  $\gamma + \text{jets}$  simulation in the photon CR (top left),  $W(\ell\nu) + \text{jets}$  (top right),  $Z(\nu\nu) + \text{jets}$  (bottom left) and VBF  $H \rightarrow \text{inv}$ . (bottom right) in the signal region.

$Z(\ell\ell) + \text{jets}$  backgrounds, and corrected with higher-order EWK corrections. To model the  $\gamma + \text{jets}$  background in photon control region, leading-order (LO) in QCD simulation samples are used instead, which are then reweighted using higher-order QCD and EWK corrections. These corrections are described in more detail in the following subsections. A concise overview of which corrections are applied to which processes is given in Tab. 3.9.

**Table 3.9:** Summary of higher-order corrections applied to simulated samples. For each boson production process, separate samples and corrections are available for the EWK and QCD production modes. “MC order” reflects the perturbative order used in the generation of the simulation sample, while the further columns represent corrections applied on a per-event level in the analysis process.

Boson	Production mode	MC order	NLO QCD	NLO EWK
Z	QCD	NLO	–	✓
	EWK	LO	✓	–
W	QCD	NLO	–	✓
	EWK	LO	✓	–
$\gamma$	QCD	LO	✓	✓
	EWK	LO	–	–

### Generator-level boson construction

All theory-based corrections of the  $W(\ell\nu) + \text{jets}$ ,  $Z(\ell\ell) + \text{jets}$ , and  $\gamma + \text{jets}$  backgrounds are parametrized as a function of the generator-level transverse momentum of the respective boson,  $p_{T,V}$ . For  $W(\ell\nu) + \text{jets}$  and  $Z(\ell\ell) + \text{jets}$  events, this quantity is calculated as follows:

1. If a boson is found in generator-level collection with `status = 62`, it's  $p_{T,V}$  is taken as the generator level  $p_{T,V}$ . (If multiple such entries are found, highest  $p_{T,V}$  is chosen.)

2. In the rare cases where the boson is not found in the generator-level collection, then the boson is defined as the four-vector sum of the selected leptons. Leptons are selected as described in the next two steps:
3. If there are electrons or muons that are not coming from a tau decay, these leptons are selected to compute  $p_{T,V}$ .
4. If the electrons or muons are found to be coming from a tau decay, or if there are no leptons in the event, the generator-level taus are chosen to compute  $p_{T,V}$ .

For  $\gamma + \text{jets}$  events, the photon at generator-level is selected by requiring the following:

- Photon needs to have  $status = 1$ , indicating that it is a final state particle (i.e. a particle that is not decayed further by the generator).
- Photon needs to have a prompt status flag.
- $|\eta| < 1.46$ , so that the photon is in the barrel region.

If there are multiple such photons, the one with highest  $p_T$  is selected.

### Photon scale factors

The photon scale factors are derived with a two-dimensional dependence on generator-level  $p_{T,V}$  and  $M_{jj}$ , and are shown for the MTR category in Fig. 3.20. These scale factors are applied to  $\gamma + \text{jets}$  events as a NLO correction, and the correction depends on the kinematics of the event.

### EWK NLO corrections to QCD V processes

Scale factors corresponding to NLO EWK corrections are obtained from Ref. [40] and applied as a function of the generator-level boson  $p_T$  to each event. The scale factors are shown in Fig. 3.21.

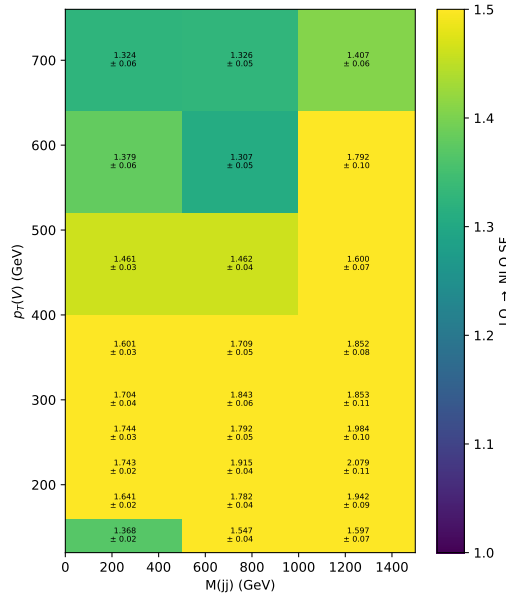


**Figure 3.20:** LO-to-NLO theory scale factors binned in the generator-level boson  $p_T$  and  $M_{jj}$ , shown photon production. The k factors are derived within the generator-level VBF selection described in the text. The uncertainties quoted in each bin are the statistical uncertainties due to the finite size of the simulated samples.

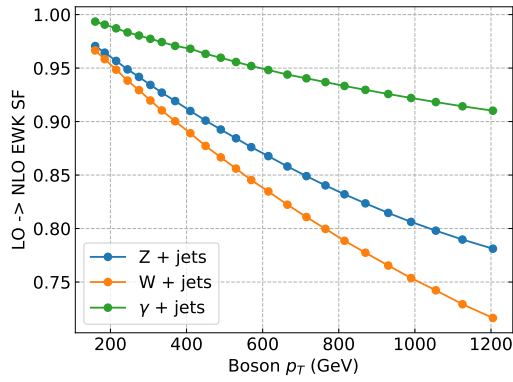


**Figure 3.21:** EWK NLO scale factors for DY, W and photon production as a function of  $p_{T,V}$ .

### QCD NLO corrections to EWK V processes

The QCD NLO corrections to VBF  $W + \text{jets}$  and  $Z + \text{jets}$  production have been calculated in Ref. [41] using the VBF@NLO program. They are parametrized in  $p_{T,V}$  and  $M_{jj}$  and are shown in Fig. 3.22.

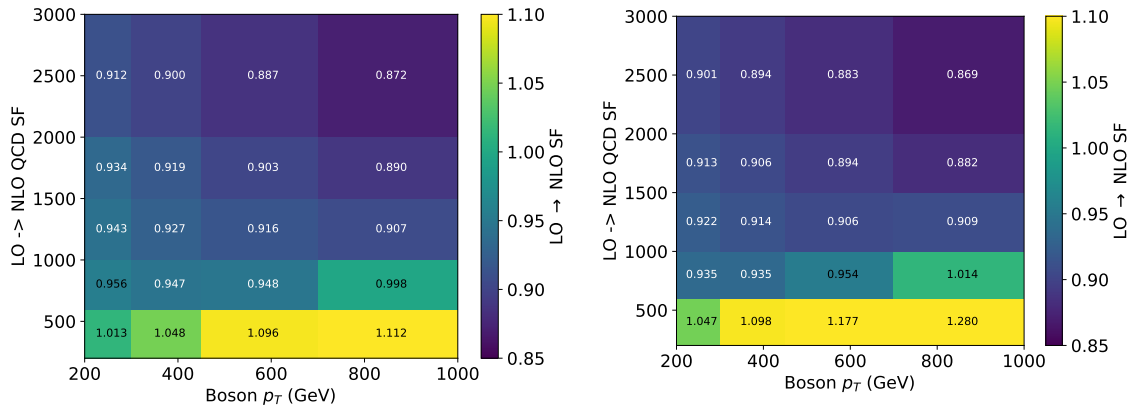


**Figure 3.22:** QCD NLO scale factors for EWK DY, W production of  $p_{T,V}$  and  $M_{jj}$ .

## NLO EWK Corrections on VBF Signal

Next to leading order (NLO) EWK corrections on VBF signal are computed using the HAWK generator [42]. The NLO corrections are computed in the VBF phase space, where events are selected based on the kinematics of the two final state VBF jets. These kinematic selections are described in Sec. 3.4. The correction is calculated as a function of the  $p_T$  of the Higgs boson, and is parametrized using the following fit function:

$$\epsilon_{EWK}(p_T^H) = (1 - 0.000372 * p_T^H - 0.0304)/0.95 \quad (3.7)$$

For each event in the VBF signal sample, this correction is applied based on the  $p_T$  of the Higgs boson found in the generator-level collection.

## 3.3 Data-quality issues

### 3.3.1 Forward HCAL (HF) Noise

The forward HCAL (HF) detector covers the most-forward rapidity range of HCAL ( $3 < |\eta| < 5$ ), as described in Sec. 2.2.4. Due to its very forward location and close proximity to the beam pipe, HF detector operates in a much harsher radiation environment. It should also be noted that the tracking detector, covering  $|\eta| < 2.5$  range, does not extend to this high rapidity phase space. Combination of these different factors makes it harder to reconstruct and cluster hadronic jets, and measure their energies accurately at the HF detector. Therefore, there is a sizable probability that the  $p_T$  of a jet reconstructed at high  $|\eta|$  being highly mismeasured. Such mismeasurements can lead to spurious  $p_T^{miss}$  in QCD multijet events (e.g.  $q\bar{q} \rightarrow q\bar{q}$ ), due to  $p_T$  of one of the final state jets being severely mismeasured. It should be noted that while the probability of such severe mismeasurement is relatively small, the very large cross section of QCD multijet processes in a p-p collider compensates for this, and the

number of events with spurious  $p_T^{miss}$  cannot be ignored. This becomes problematic for analyses that target  $p_T^{miss}$  (such as analyses targeting  $H \rightarrow inv.$  signature), since mismeasured QCD multijet events can pass the high  $p_T^{miss}$  requirement imposed on the analysis signal region. Hence, this effect needs to be taken into account.

It was observed that jets resulting from such mismeasurement present a distinguishable shape with respect to well-identified jets: Their shower shape is spread in  $\eta$  and narrow in  $\phi$ . Shower shape variables of HF jets ( $\sigma_{i\eta i\eta}$ ,  $\sigma_{i\phi i\phi}$ , HF central strip size) have therefore been introduced and added to the event content in the input datasets.  $\sigma_{i\eta i\eta}$  represents the shower width of the HF jet in  $\eta$  direction, and similarly,  $\sigma_{i\phi i\phi}$  represents the shower width in  $\phi$  direction. Their definitions can be found below:

$$\begin{aligned}\sigma_{i\eta i\eta} &= \sqrt{\frac{\sum_i \Delta\eta(i, jet)^2 \omega_i}{\sum_i \omega_i}} \\ \sigma_{i\phi i\phi} &= \sqrt{\frac{\sum_i \Delta\phi(i, jet)^2 \omega_i}{\sum_i \omega_i}}\end{aligned}\tag{3.8}$$

In Eq. 3.8, the sums run over all PF candidates with  $p_T > 3$  GeV, and  $\omega_i$  is the weight applied to PF candidate  $i$  within the jet, which is computed as follows:

$$\omega_i = \frac{p_T^i - p_T^{\text{PU offset}}}{\sum_i p_T^i - p_T^{\text{PU offset}}}\tag{3.9}$$

In Eq. 3.9,  $p_T^{\text{PU offset}}$  refers to the offset correction on the  $p_T$  of the particle due to pileup (PU). It is defined as follows:

$$p_T^{\text{PU offset}} = \frac{\text{jet L1 offset / gen vtx}}{\pi \times 0.4^2} \times \frac{N_{\text{reco vertices}}}{\epsilon^{\text{reco}}(\text{PU vtx})} \times S_{\text{HF tower}}\tag{3.10}$$

The other distinguishing variable, HF central strip size ( $CSS_{HF}$ ), is computed as follows:  $N_{cands}$  with  $p_T > 10$  GeV &  $|\Delta\phi(cand, jet)| < 0.05$ . It is a measure of the number of highly energetic particles reconstructed close to the jet centroid (i.e.

$|\Delta\phi(\text{cand}, \text{jet})| < 0.05$ ). In the event of spurious large energy deposits from a jet, one can expect larger number of energetic particles being reconstructed closer to the jet centroid, as a result of those energy deposits.

These variables are used to define a series of cuts rejecting most of the HF-related noise, while keeping a high efficiency on well-identified jets. The efficiency of the cuts on physics jets in data and simulation is measured and their ratio is used to correct the simulation. This procedure is described in Sec. 3.2.5. After the HF noise cuts are applied, the residual noise in the signal region is estimated using a data driven technique. The study and the definition of the HF noise cuts, and the residual HF noise estimation are discussed in the subsections below.

### Definition of HF Noise Cuts

In order to study the discriminating power of these variables directly in data, two regions enriched in “physics” jets and “noise” jets are defined. “Physics” jets refer to HF jets that are recoiling against a well-reconstructed physics object (in this study, a photon), and “noise” jets refer to HF jets that recoil against no visible physics object, hence creating  $p_T^{\text{miss}}$  in the event.

The physics-enriched region consists of events where a HF jet recoils against a photon. Jet and photon being back-to-back is ensured by a series of cuts on  $\Delta\phi(\gamma, \text{jet})$ , ratio of transverse momenta of the photon and the jet, and also the requirement of low  $p_T^{\text{miss}}$  in the event. The selections are listed below:

- Exactly one well identified photon (tight identification, as discussed in Sec. 3.1.4)
- Events passing a single photon trigger requiring  $p_T^\gamma > 110$  GeV
- $\Delta\phi(\gamma, \text{jet}) > 2.7$
- $0.5 < \frac{p_T(\gamma)}{p_T(\text{jet})} < 1.5$

- $p_T^{miss} < 50 \text{ GeV}$

The noise-enriched region includes events with exactly one high  $p_T$  HF jet and high  $p_T^{miss}$ . The aim here is to collect events with a mis-measured HF jet, such that it has very high  $p_T$ , but there is no other high  $p_T$  physics object in the event. The complete requirements for this region are listed below:

- Events passing a trigger based on  $p_T^{miss}$  and  $H_T^{\text{miss}}$ .
- $p_T^{miss} > 100 \text{ GeV}$
- Exactly one HF jet with  $p_T > 100 \text{ GeV}$
- No extra jet with  $p_T > 30 \text{ GeV}$
- No lepton with  $p_T > 10 \text{ GeV}$

The two regions outlined above are used to study the distribution of HF shower shape variables for well-identified jets, as opposed to events containing a mis-measured (“noisy”) jet. Mainly, two sets of cuts are studied and adopted in the analysis:

- Cuts on  $\sigma_{i\eta i\eta}$  and  $\sigma_{i\phi i\phi}$
- Cut on HF central strip size

Since the HF-related noise strongly peaks in the  $3 < |\eta| < 3.25$  region and the size of the HF towers is  $|\eta|$  dependent, possibly affecting the variables under study, three  $|\eta|$  regions are considered. Two dimensional distributions of  $\sigma_{i\phi i\phi}$  vs  $\sigma_{i\eta i\eta}$  are shown in Fig. 3·23 and Fig. 3·24, for the noise and physics enriched regions respectively. From Fig. 3·23, the skewness of the 2D distribution towards high  $\sigma_{i\eta i\eta}$  and low  $\sigma_{i\phi i\phi}$  can be observed, specifically for  $|\eta| < 4$ . This motivates the diagonal cut of  $\sigma_{i\eta i\eta} - \sigma_{i\phi i\phi} <$

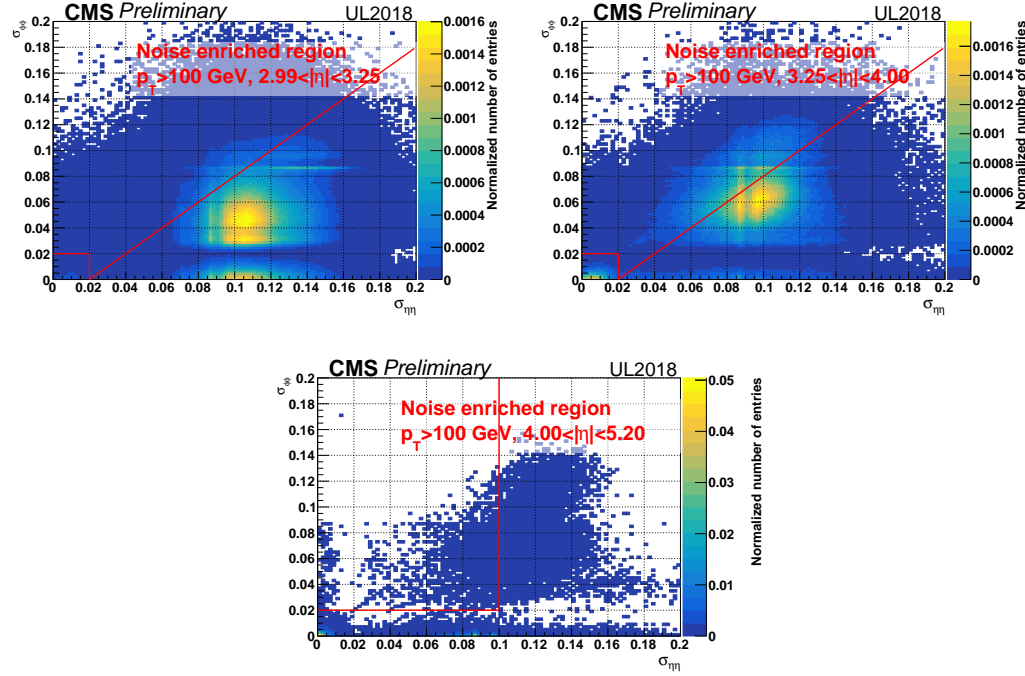


**Figure 3.23:** Two dimensional distribution of  $\sigma_{i\eta i\eta}$  and  $\sigma_{i\phi i\phi}$  in the noise-enriched region, split by the  $|\eta|$  of the jet. The first plot shows  $2.99 < |\eta| < 3.25$  interval, the second one shows  $3.25 < |\eta| < 4$  and the last one shows  $4 < |\eta| < 5.2$ . The red lines on the plots indicate the cuts applied on these variables.

0.02, cutting away a sizable number of noisy events while having much less impact in the physics-enriched region.

In the noise enriched region, there are also a large number of events observed within the region defined by  $\sigma_{i\eta i\eta} < 0.02$  and  $\sigma_{i\phi i\phi} < 0.02$ . These are thought to be interactions of halo muons in the HF detector and this region with very low  $\sigma_{i\eta i\eta}$  and  $\sigma_{i\phi i\phi}$  is therefore also vetoed.

For jets with  $|\eta| > 4$ , the requirement becomes  $\sigma_{i\eta i\eta} < 0.1$  and  $\sigma_{i\phi i\phi} > 0.02$ , as large numbers of noise events are observed at very low  $\sigma_{i\phi i\phi}$  and high  $\sigma_{i\eta i\eta}$ .

The second cut is applied on the HF central strip size ( $CSS_{HF}$ ) of the jet. The two-dimensional distributions of central and adjacent strip sizes for the noise enriched region are shown in Fig. 3.25, while the same distributions in the physics enriched

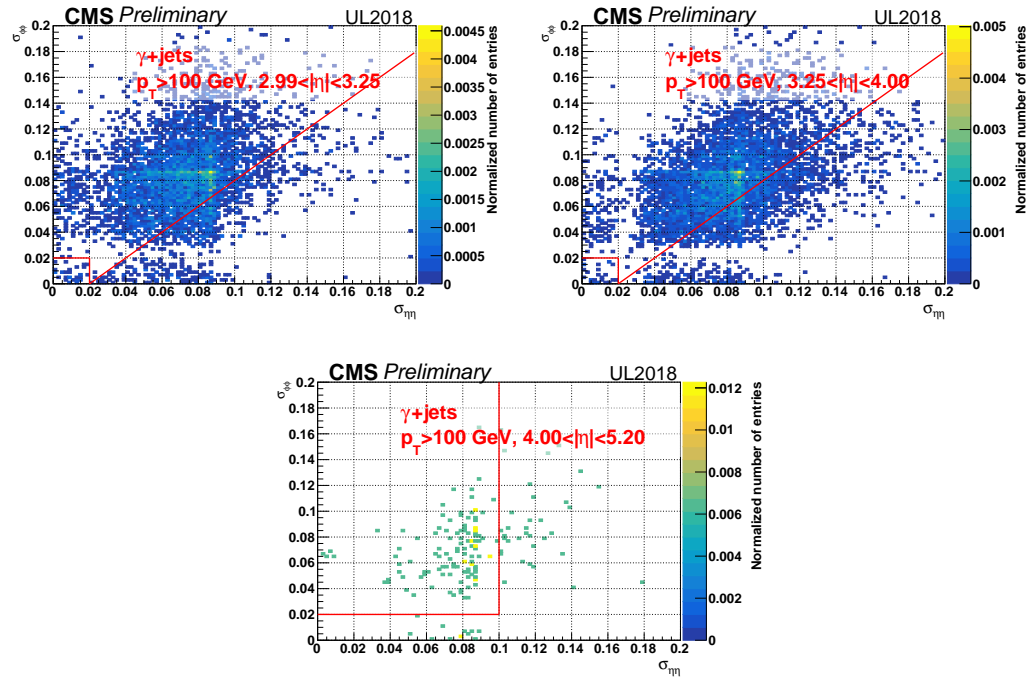


**Figure 3·24:** Two dimensional distribution of  $\sigma_{i\eta i\eta}$  and  $\sigma_{i\phi i\phi}$  in the physics-enriched region, split by the  $|\eta|$  of the jet. The first plot shows  $2.99 < |\eta| < 3.25$  interval, the second one shows  $3.25 < |\eta| < 4$  and the last one shows  $4 < |\eta| < 5.2$ . The red lines on the plots indicate the cuts applied on these variables.

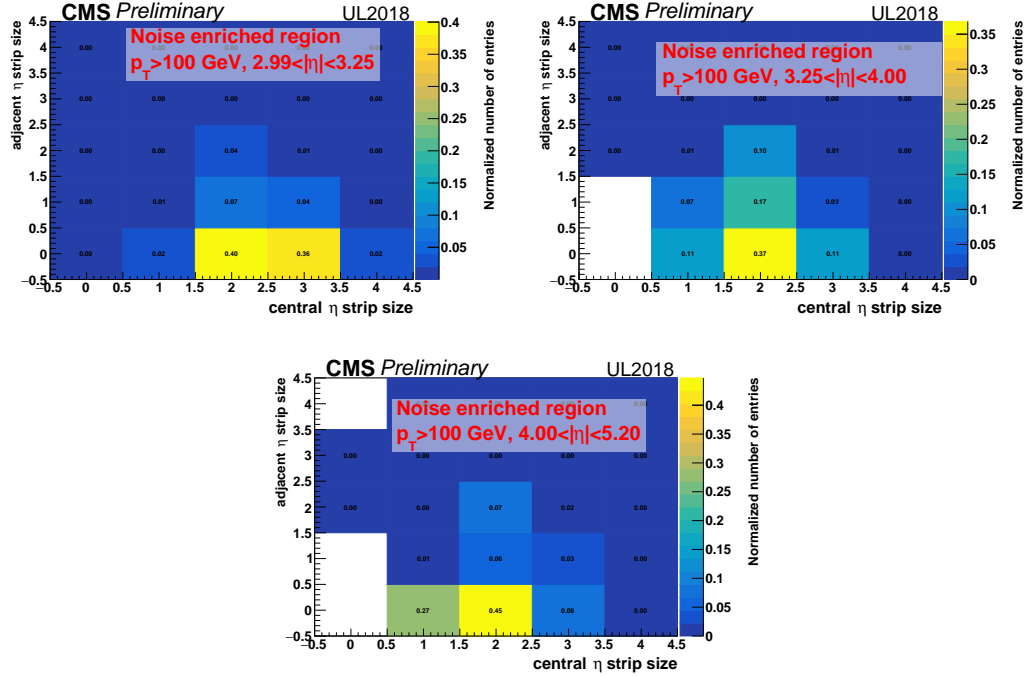


**Figure 3·25:** Two dimensional distribution of central and adjacent strip sizes in the noise enriched region, split by the  $|\eta|$  of the jet. The first plot shows  $2.99 < |\eta| < 3.25$  interval, the second one shows  $3.25 < |\eta| < 4$  and the last one shows  $4 < |\eta| < 5.2$ .

region are shown in Fig. 3·26. For the jets in noise enriched region with  $2.99 < |\eta| < 3.25$  (where the noise contribution is the highest), it can be observed that around 40% of jets have  $CSS_{HF} \geq 3$ , while in the physics enriched region, this fraction is very small,  $\mathcal{O}(1\%)$ . Therefore, a cut on the  $CSS_{HF}$  variable is adopted in the analysis, requiring  $CSS_{HF} < 3$  for HF jets that are back to back with  $p_T^{miss}$ .

In summary, the cleaning cuts applied to HF jets are:

- $2.99 < |\eta| < 4.0$ :  $\sigma_{i\eta i\eta} - \sigma_{i\phi i\phi} < 0.02$  condition is required. In addition, the corner region, defined as  $\sigma_{i\eta i\eta} < 0.02$  &  $\sigma_{i\phi i\phi} < 0.02$ , is also removed from the analysis.
- $|\eta| > 4.0$ :  $\sigma_{i\eta i\eta} < 0.1$  &  $\sigma_{i\phi i\phi} > 0.2$  condition is required.

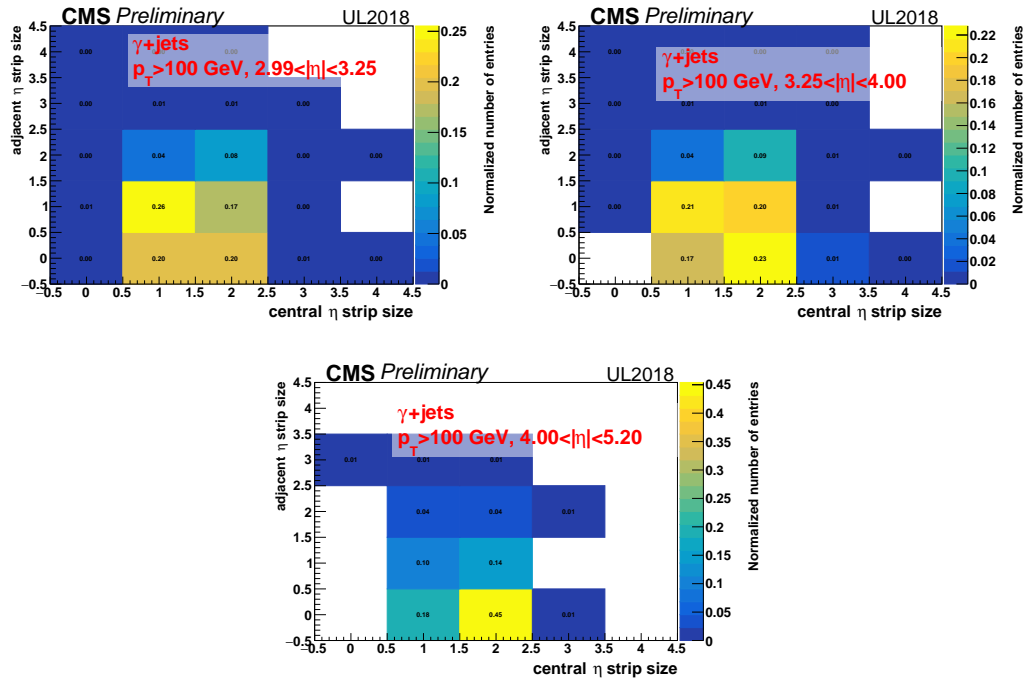


**Figure 3·26:** Two dimensional distribution of central and adjacent strip sizes in the physics enriched region, split by the  $|\eta|$  of the jet. The first plot shows  $2.99 < |\eta| < 3.25$  interval, the second one shows  $3.25 < |\eta| < 4$  and the last one shows  $4 < |\eta| < 5.2$ .

- $|\eta| > 2.99$ :  $CSS_{HF} < 3$  is required.

They are applied to all jets with  $p_T > 80 \text{ GeV}$  and  $|\eta| > 2.99$  that are back-to-back with  $p_T^{miss}$  (i.e.  $\Delta\phi(jet, p_T^{miss}) > 2.5$ ). If any such jet fails the cuts, the event is rejected.

### Residual HF Noise Estimation

In addition to the HF cleaning cuts explained in the previous subsection, a noise estimation is done to estimate the leftover noise contribution in the analysis signal region. For the noise estimation, a new control region is defined in which the HF shape cuts are inverted. Other than the HF shape cuts, the same cuts are required in this control region as in the VBF signal region, which are discussed in Sec. 3.4.1.

With the addition of this new control region (CR), the estimation is done in three steps. First, data and MC yields in this CR are computed ( $N_{data}$ ,  $N_{MC}$ ). The excess amount of data over MC in this control region gives the number of noise events:  $N_{noise}^{CR} = N_{data} - N_{MC}$ . Finally, the noise estimate in analysis signal region is calculated from  $N_{noise}^{CR}$  by using  $[p_T, \eta]$  dependent transfer factors, defined as the relative probability for a noise event to pass the HF shape cuts, relative to failing them. Putting it all together, the noise estimate in VBF signal region becomes the following:

$$N_{noise}^{SR} = \frac{P(\text{pass}|noise)}{P(\text{fail}|noise)} \times (N_{data}^{CR} - N_{MC}^{CR}) \quad (3.11)$$

In Eq. 3.11,  $P(\text{pass}|noise)$  refers to the probability of an event with a noisy HF jet to pass the HF shape cuts, and  $P(\text{fail}|noise)$  refers to the probability of such an event to fail the HF cuts. By definition,  $P(\text{pass}|noise) + P(\text{fail}|noise) = 1$ . It should also be noted that the  $N_{noise}^{SR}$  is calculated for each  $M_{jj}$  bin.

In Fig. 3.27, the HF noise estimation results are shown as a function of  $M_{jj}$ . Plots

on the left column show the data and total MC yields in the HF noise CR, already scaled by the transfer factor as defined above. Plots on the right column show the resulting HF noise estimation in the analysis signal region, which correspond to the difference of data and MC yields in the left-hand side plots. Plots on the top show the results with 2017 data, and plots on the bottom show results with 2018 data.

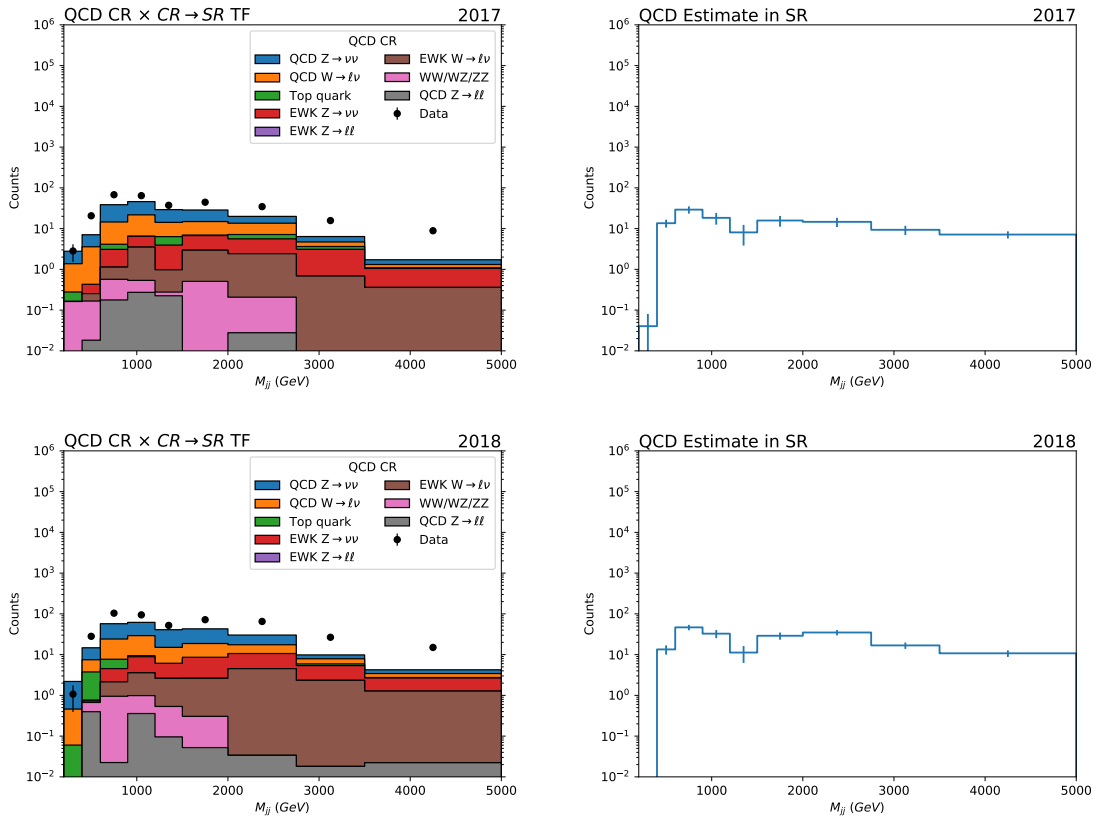


**Figure 3.27:** HF noise estimate in 2017 (top) and 2018 (bottom) data. The plots on the left column show the data and total MC yields in the HF noise control region, scaled by the jet-based transfer factor, while the plots on the right show the resulting noise estimation in the signal region, which correspond to the difference of data and MC yields in the left-hand side plot.

From Fig. 3.27, it can be observed that the HF noise estimate in the signal region is mostly flat as a function of  $M_{jj}$ , and can make a sizable contribution at higher  $M_{jj}$  values where most of the other background processes are suppressed.

To make sure that this noise estimation provides an accurate modeling of the data in the phase space where HF noise contribution is highest,  $3 < |\eta| < 3.25$ , a closure test was performed. A subset of events in VBF signal region were picked, which have the leading jet in the  $3 < |\eta| < 3.25$  range, and the data yields are compared to the expected background yields in this region, including the HF noise estimation. For these events, Fig. 3·28 shows the  $\Delta\phi(p_{T,trk}^{miss}, p_T^{miss})$  distribution, where  $p_{T,trk}^{miss}$  refers to the  $p_T^{miss}$  computed only relying on the tracks reconstructed by the tracker. The HF noise contribution to the background estimation is expected to be especially significant at high  $\Delta\phi$  values, since such events have a forward jet with  $|\eta| > 3$ , which is well outside the tracker range. Due to the presence of such jets, large  $\Delta\phi$  between the tracker-only  $p_T^{miss}$  and full  $p_T^{miss}$  is expected. It should also be noted that for this high  $\Delta\phi$  region, the VBF  $H \rightarrow inv.$  signal contribution is expected to be small, hence it would be expected that the data and background yields agree within a reasonable extent.

From Fig. 3·28, it can be observed, especially at high  $\Delta\phi(p_{T,trk}^{miss}, p_T^{miss})$ , the agreement between data and background yields is good after the residual HF noise estimation is taken into account. To account for residual disagreements between data and background estimation, a 20% flat uncertainty is assigned to the HF noise template.

### 3.3.2 Missing HE-15/16 sectors in 2018

During a large part of data-taking in 2018, a submodule of the HCAL was not functioning. As a result, no HCAL deposits have been recorded in the region of  $-3.0 < \eta < -1.3$  and  $-1.57 < \phi < -0.87$  for the affected portion of the recorded dataset. These missing HCAL deposits have the following consequences for this analysis:

- The jets that are affected will often be wrongly reconstructed as an electron.

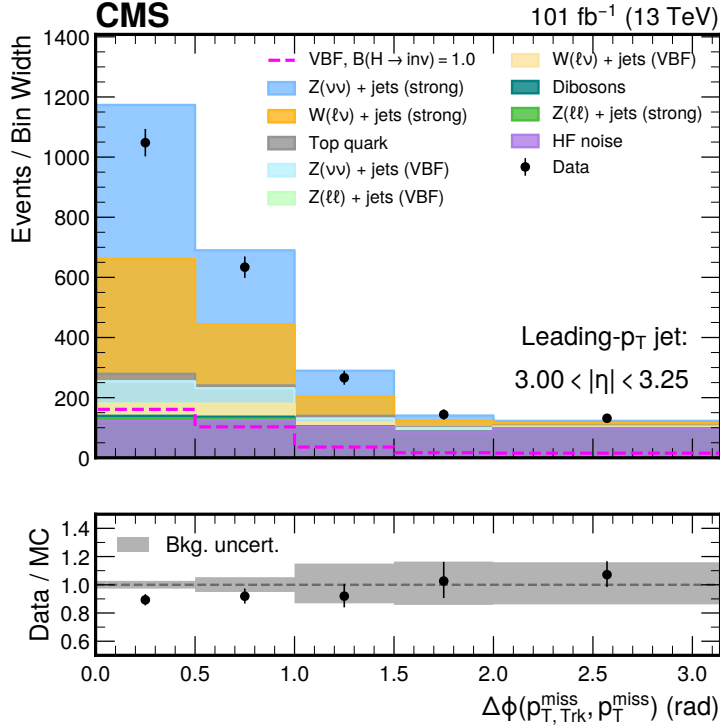


**Figure 3.28:**  $\Delta\phi(p_{T,\text{miss}}, p_T^{\text{miss}})$  distribution for the closure test on the HF noise estimate. Events plotted here pass the VBF signal region selection, and have the leading jet in  $3 < |\eta| < 3.25$  range, where the HF noise contribution is highest. It can be observed, especially at high  $\Delta\phi(p_{T,\text{miss}}, p_T^{\text{miss}})$ , the agreement between data and background yields is good after the residual HF noise estimation is taken into account. To account for residual differences, a 20% flat uncertainty is assigned to the HF noise template.

These mis-reconstructed electrons can pass the identification criteria imposed in the electron control regions, due to the lack of HCAL energy deposits. Therefore, such events with mis-reconstructed jets in this  $[\eta, \phi]$  region can contaminate the electron control regions.

- Affected jets will not be calibrated correctly, because the energy of the reconstructed jet is dependent on all the HCAL deposits. Such mis-calibration will result in anomalous  $p_T^{\text{miss}}$  in such events.

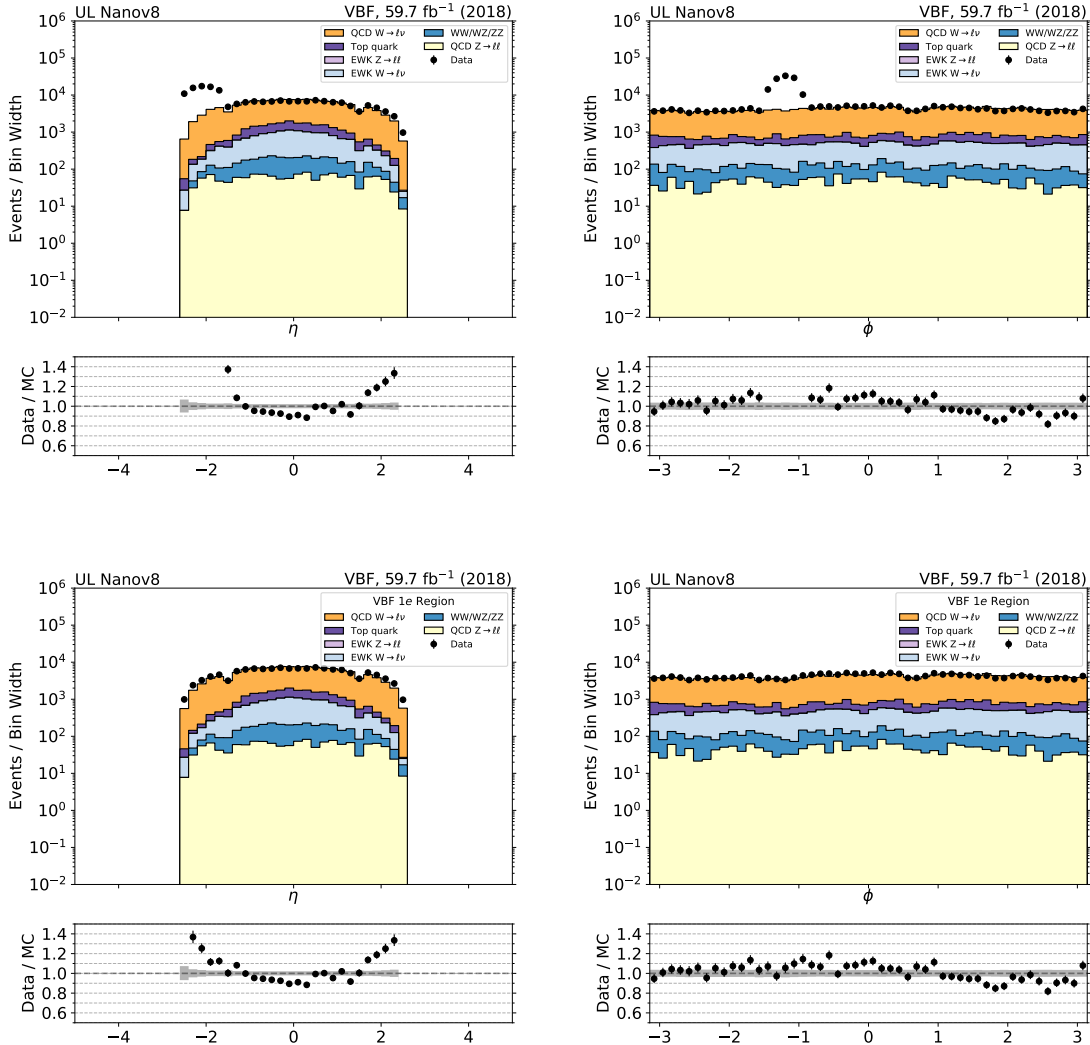
Therefore, it was found that the analysis regions that are most impacted by this problem are the signal region and single electron control region. Additional requirements were imposed on these two regions to reject mis-reconstructed events arising due to the missing HCAL deposits. The studies done to identify the impact on the analysis, and the requirements imposed are outlined below.

Figure 3.29 shows the impact of a veto on events having electrons reconstructed in the impacted  $[\eta, \phi]$  region. The alternative of "ignoring" electrons in that region, i.e. demoting them to jets and recalculating the leading jet pair and other relevant selection variables, leads to almost identical results: The source of these jets is QCD multijet events, hence very few of these events have another good electron to pass the selection for  $W \rightarrow e\nu$  events. Therefore, an event veto is imposed on the single electron control region, if the reconstructed electron is found to be within the impacted phase space.

The muon control regions are not affected from the missing HCAL deposits, thanks to the tight muon criteria imposed both in Z and W muon control regions.

The other impacted analysis region is the signal region. Figs. 3.30 and 3.31 show the distributions, in data and MC, of the leading and subleading jet  $\phi$  and the  $\phi$  of the  $p_T^{miss}$  vector ( $\phi_{p_T^{miss}}$ ), in the signal region in 2018. From Figs. 3.30 and 3.31, it can be observed that the agreement between data and MC is good except for the region where  $-1.8 < \phi_{p_T^{miss}} < -0.6$ . This is co-incident with the missing HCAL submodule. The same disagreement can be seen in the jet  $\phi$  distributions, on the opposite side in  $\phi$ , which arises due to the signal selection requirement that the jets and missing energy are not aligned. To mitigate this problem in the signal region, the following additional requirement is imposed on 2018 data:

- For events in data where the run number is smaller than 319077 (i.e. before the HCAL submodule malfunctioning) no additional requirement is imposed, since



**Figure 3.29:** Effects of an electron veto in the affected detector region (single electron control region 2018). Plots on the top show the  $\eta$  and  $\phi$  of the highest  $p_T$  electron in the event without any veto, while plots on the bottom show the  $\eta$  and  $\phi$  of the electron with the veto.

those events are not impacted by the problem. Out of the full  $59.7 \text{ fb}^{-1}$  of 2018 data, these events correspond to  $21.1 \text{ fb}^{-1}$  of integrated luminosity.

- For events in data where the run number is larger or equal to 319077, the event is discarded if it has  $-1.8 < \phi_{p_T^{\text{miss}}} < -0.6$ . These events correspond to a  $38.6 \text{ fb}^{-1}$  of integrated luminosity.

The usage of run number to identify if the event is impacted by the missing HCAL submodule allows to keep 100% of the data before the problem occurred. This effect is modeled in simulation by reweighting the set of events with  $-1.8 < \phi_{p_T^{\text{miss}}} < -0.6$  with the fraction of luminosity without impact. This weight corresponds to  $21.1/59.7 = 0.35$ . Therefore, about 35% of the events with  $-1.8 < \phi_{p_T^{\text{miss}}} < -0.6$  in simulation are kept in the analysis.

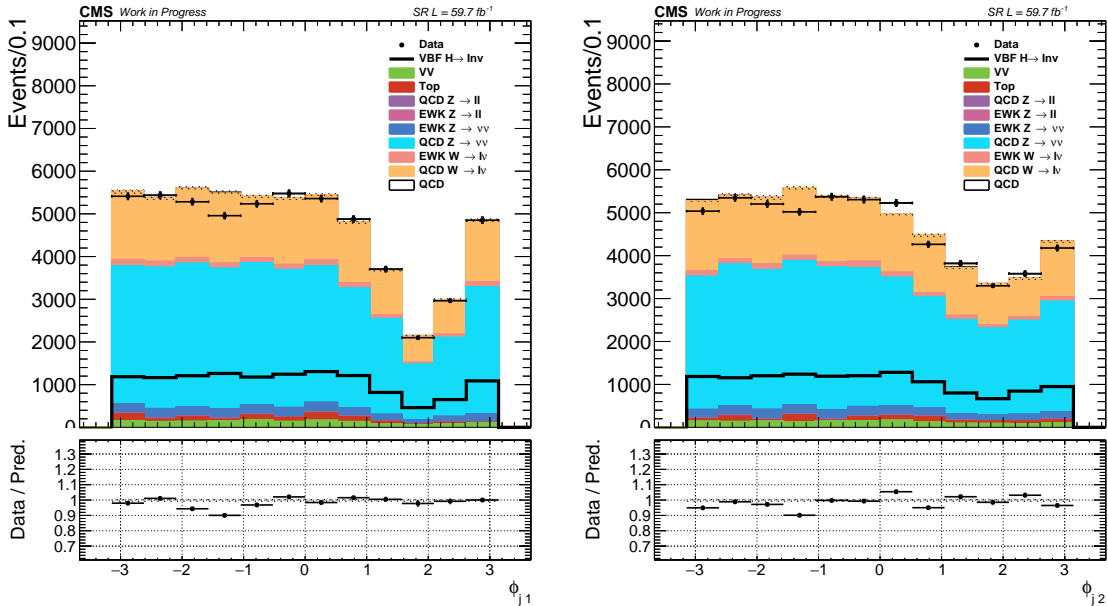


**Figure 3.30:** Leading (left) and subleading (right) jet  $\phi$  distributions in the signal region from the 2018 dataset. The bands in the ratio plots represent the statistical uncertainties in the MC.

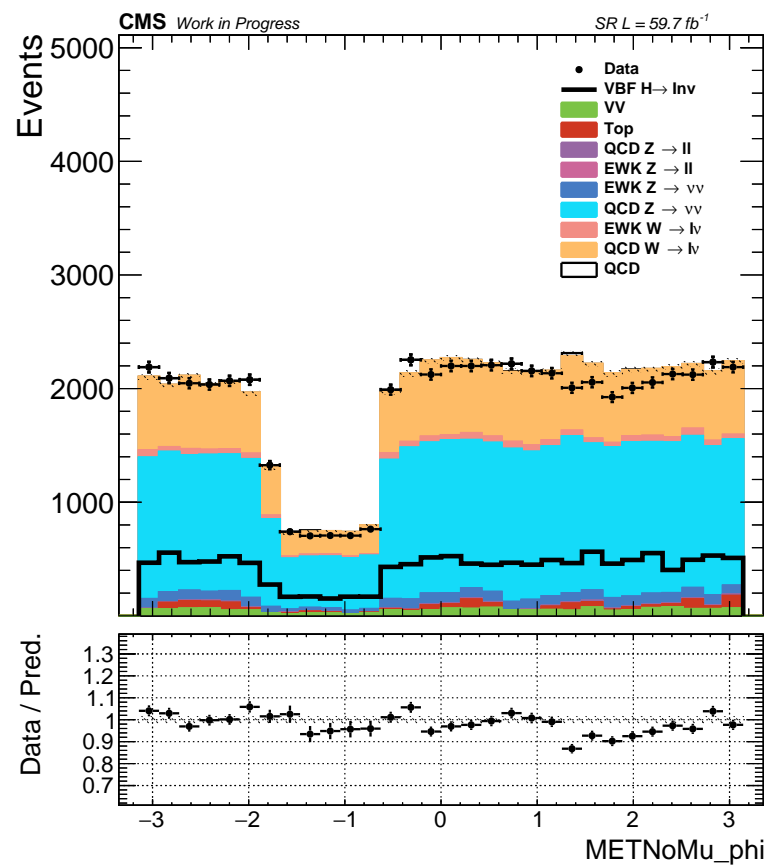


**Figure 3.31:**  $\phi_{p_T^{\text{miss}}}$  distribution in the signal region from the 2018 dataset.

## 3.4 Event selection

### 3.4.1 Signal region selection

Events in the VBF signal region are selected by using triggers which require  $p_{T,no-\mu}^{miss} > 120$  GeV and  $H_{T,no-\mu}^{miss} > 120$  GeV at HLT-level (described in Sec. 3.2.1). The  $p_{T,no-\mu}^{miss}$  corresponds to the magnitude of the vector  $p_{T,V}$  sum of all the particles reconstructed by the trigger algorithm, while the  $H_{T,no-\mu}^{miss}$  is computed as the magnitude of the vector  $p_{T,V}$  sum of jets with  $p_T > 20$  GeV and  $|\eta| < 5.0$ . The energy fraction attributed to neutral hadrons in these jets is required to be smaller than 90%. This requirement suppresses anomalous events with jets originating from detector noise. To be able to use the same triggers for selecting events in the muon control regions used for background prediction, muon candidates are not included in the  $p_{T,no-\mu}^{miss}$  and  $H_{T,no-\mu}^{miss}$  computation. The trigger efficiency is measured to be 96% for events passing the analysis selection for  $p_T^{miss} > 250$  GeV and becomes more than 99% efficient for events with  $p_T^{miss} > 350$  GeV. The performance of these triggers are further discussed in Sec. 3.2.1.

Candidate events are required to have  $p_T^{miss} > 250$  GeV. The leading AK4 jet in the signal event is required to have  $p_T > 80$  GeV and  $|\eta| < 4.7$ , and the subleading AK4 jet is required to have  $p_T > 40$  GeV and  $|\eta| < 4.7$ . Both leading jets are required to have neutral hadron fraction values of less than 80% and charged hadron fraction values of at least 10% to further reduce the possibility of noise contamination. In addition, the analysis employs various event filters to reduce events with large misreconstructed  $p_T^{miss}$  [43] originating from non-collision backgrounds. The filters are complemented by a requirement on the relative difference between the default PF  $p_T^{miss}$  value used in the analysis and the  $p_T^{miss}$  value reconstructed just from calorimeter deposits and muons. In an event with genuine  $p_T^{miss}$ , one would expect the two  $p_T^{miss}$  calculations to result in reasonably close values. Following this constraint, the following cut is

imposed on events:

$$\frac{\Delta p_T^{miss}(\text{PF, Calo})}{p_T^{miss}} < 0.5 \quad (3.12)$$

In Eq. 3.12,  $\Delta p_T^{miss}(\text{PF, Calo})$  refers to the absolute difference of  $p_T^{miss}$  values calculated using the full event information (PF) and calorimeter information only (Calo).

For the VBF  $H \rightarrow inv.$  signal events, two leading jets in opposite hemispheres are expected in the final state, with large dijet mass. Furthermore, these jets are expected to have large rapidity separation ( $\Delta\eta_{jj}$ ) and small azimuthal separation ( $\Delta\phi_{jj}$ ). Therefore, this analysis employs several requirements on  $M_{jj}$ ,  $\Delta\eta_{jj}$  and  $\Delta\phi_{jj}$ , which can be found in Table 3.10.

The main background processes in this search are the  $Z(\nu\nu) + \text{jets}$  and  $W(\ell\nu) + \text{jets}$  processes. The  $Z(\nu\nu) + \text{jets}$  process is an irreducible background and constitutes the largest background in the search. In contrast, the background from  $W(\ell\nu) + \text{jets}$  is suppressed by imposing a veto on events containing one or more loose muons or electrons with  $p_T > 10$  GeV, or hadronically decaying  $\tau$  leptons with  $p_T > 20$  GeV. Events that contain a loose, isolated photon with  $p_T > 15$  GeV and  $|\eta| < 2.5$  are also rejected. This helps to suppress electroweak (EWK) backgrounds in which a photon is radiated from the initial state. To reduce the contamination from top quark backgrounds, events are rejected if they contain a b tagged jet with  $p_T > 20$  GeV and  $|\eta| < 2.4$ . These jets are identified using the DeepCSV algorithm [29, 44], adopting the “medium” working point, which corresponds to correctly identifying a jet originating from a bottom quark with a probability of 80% and misidentifying a jet originating from a charm quark (light-flavor jet) with a probability of 12 (2)%.

Lastly, QCD multijet background with  $\vec{p}_T^{miss}$  arising from mismeasurements of the jet momenta is suppressed by requiring the minimum azimuthal angle between the  $\vec{p}_T^{miss}$

direction and each of the first four leading jets with  $p_T > 30 \text{ GeV}$  and  $|\eta| < 4.7$  to be larger than 0.5 radians.

The selection requirements for the signal region in this analysis are summarized in Table 3.10.

**Table 3.10:** Summary of the signal region selection requirements.  
Leading and subleading jets refer to the highest and second-highest  $p_T$  jets in the event.

Variable	Selection	Target background
Muon (electron) veto	$p_T > 10 \text{ GeV},  \eta  < 2.4(2.5)$	$Z(\ell\ell) + \text{jets}, W(\ell\nu) + \text{jets}$
$\tau$ lepton veto	$p_T > 20 \text{ GeV},  \eta  < 2.3$	$Z(\ell\ell) + \text{jets}, W(\ell\nu) + \text{jets}$
Photon veto	$p_T > 15 \text{ GeV},  \eta  < 2.5$	$\gamma + \text{jets}$
Bottom jet veto	DeepCSV medium $< 0.4941/0.4184$ (2017 / 2018) for all jets with $p_T > 20 \text{ GeV},  \eta  < 2.4$	Top quark
$p_T^{\text{miss}}$	$> 250 \text{ GeV}$	QCD, top quark, $Z(\ell\ell) + \text{jets}$
$\Delta\phi(\vec{p}_{\text{T}}^{\text{jet}}, \vec{p}_{\text{T}}^{\text{miss}})$	$> 0.5 \text{ radians}$	QCD
Two leading jet IDs	POG tight ID, CHF $> 0.1$ , NHF $< 0.8$	Noise
HF-noise rejection	Cuts on HF shape variables, $\sigma_{i\eta i\eta}, \sigma_{i\phi i\phi}$ and HF central strip size	HF noise
$\Delta p_T^{\text{miss}}(\text{PF, Calo}) / \text{recoil}$	$< 0.5$	Noise
Leading AK4 jet $p_T$ and $\eta$	$> 80 \text{ GeV}$ and $ \eta  < 4.7$	All
Subleading AK4 jet $p_T$ and $\eta$	$> 40 \text{ GeV}$ and $ \eta  < 4.7$	All
$M_{jj}$	$> 200 \text{ GeV}$	
$\Delta\eta_{jj}$	$> 1.0$	
$\Delta\phi_{jj}$	$< 1.5$	

It should be noted that the selections listed in Table 3.10 refer to one of the two event selection categories in the analysis, the MET-triggered (MTR) category. In addition to the MTR category, there is another orthogonal event selection category called the VBF-triggered (VTR) category [7]. Events in this category are collected using different HLT paths that require the presence of two energetic jets in the final state, and have  $160 < p_T^{\text{miss}} < 250 \text{ GeV}$ , hence the orthogonality to the MTR category being considered here ( $p_T^{\text{miss}} > 250 \text{ GeV}$ ). For the purposes of this thesis, the VTR category won't be discussed in detail, but the combined results with the VTR category will be mentioned in Sec. 4.

Figs. 3.32, 3.33, and 3.34 show the distribution of the  $p_T^{\text{miss}}$ ,  $M_{jj}$ ,  $\Delta\eta_{jj}$  and  $\Delta\phi_{jj}$  of the VBF jet pair (two highest- $p_T$  jets), the  $p_T$  and  $\eta$  distributions of the leading and subleading jets, and the  $\eta$  distributions of the most central and most forward jets, re-

spectively, for events passing the VBF signal region selection. The same distributions are shown for the 2018 samples in Figs. 3·35, 3·36, and 3·37.

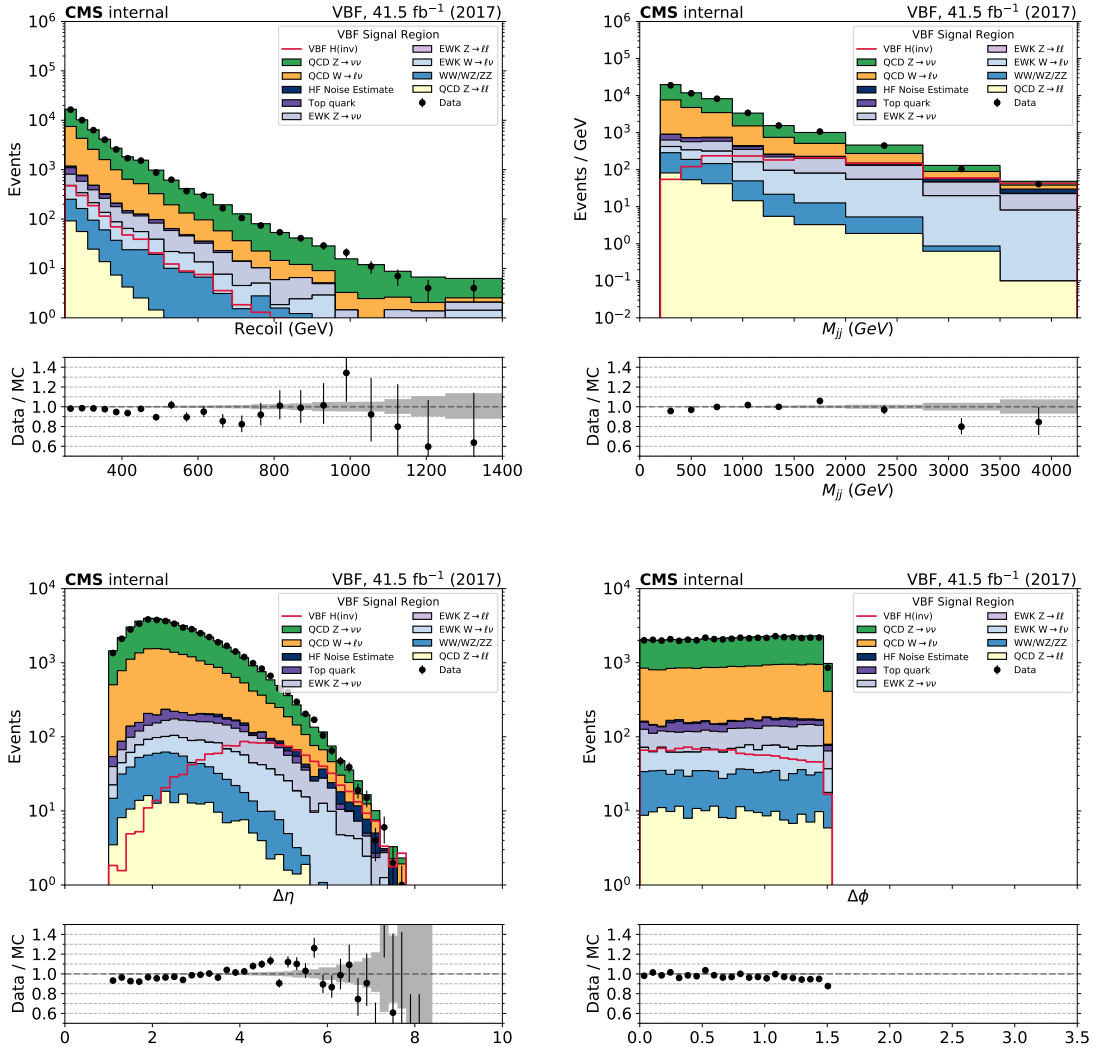


**Figure 3.32:** Recoil distribution,  $M_{jj}$  distribution,  $\Delta\eta_{jj}$  and  $\Delta\phi_{jj}$  distribution in the VBF signal region, using 2017 dataset.

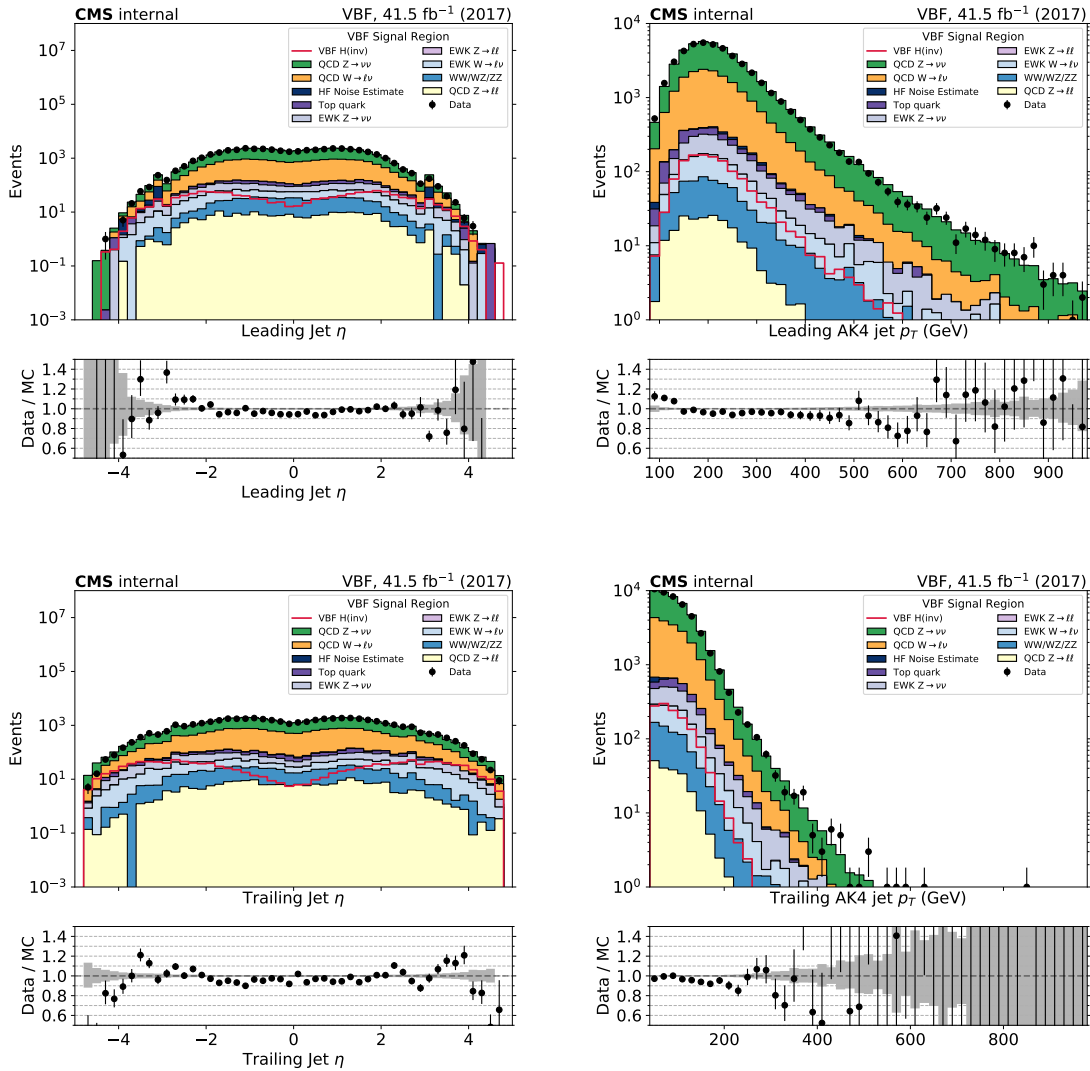


**Figure 3.33:** Leading and subleading jets  $p_T$  and  $\eta$  in the VBF signal region, using 2017 dataset.

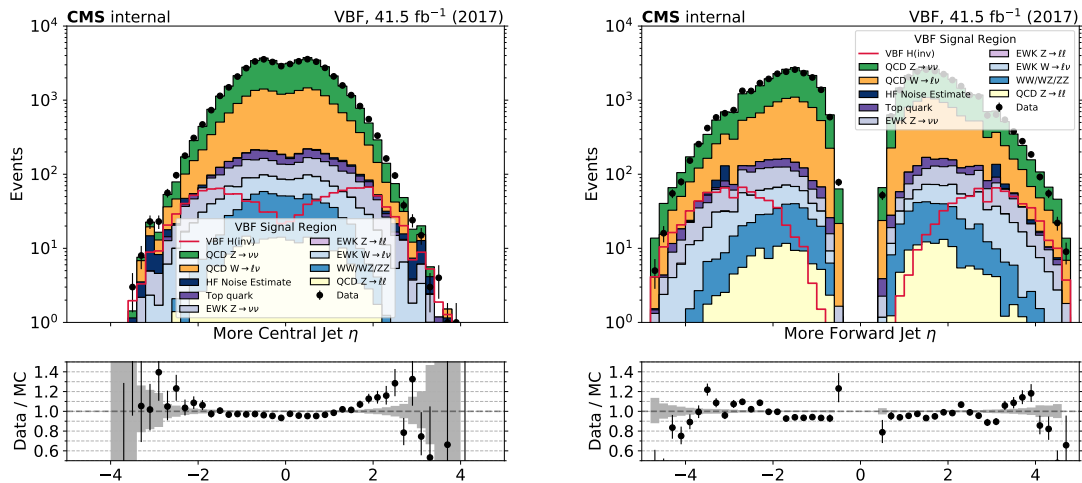


**Figure 3.34:** Most central (left) and most forward jets (right)  $\eta$  of the VBF pair in the VBF signal region, using 2017 dataset.

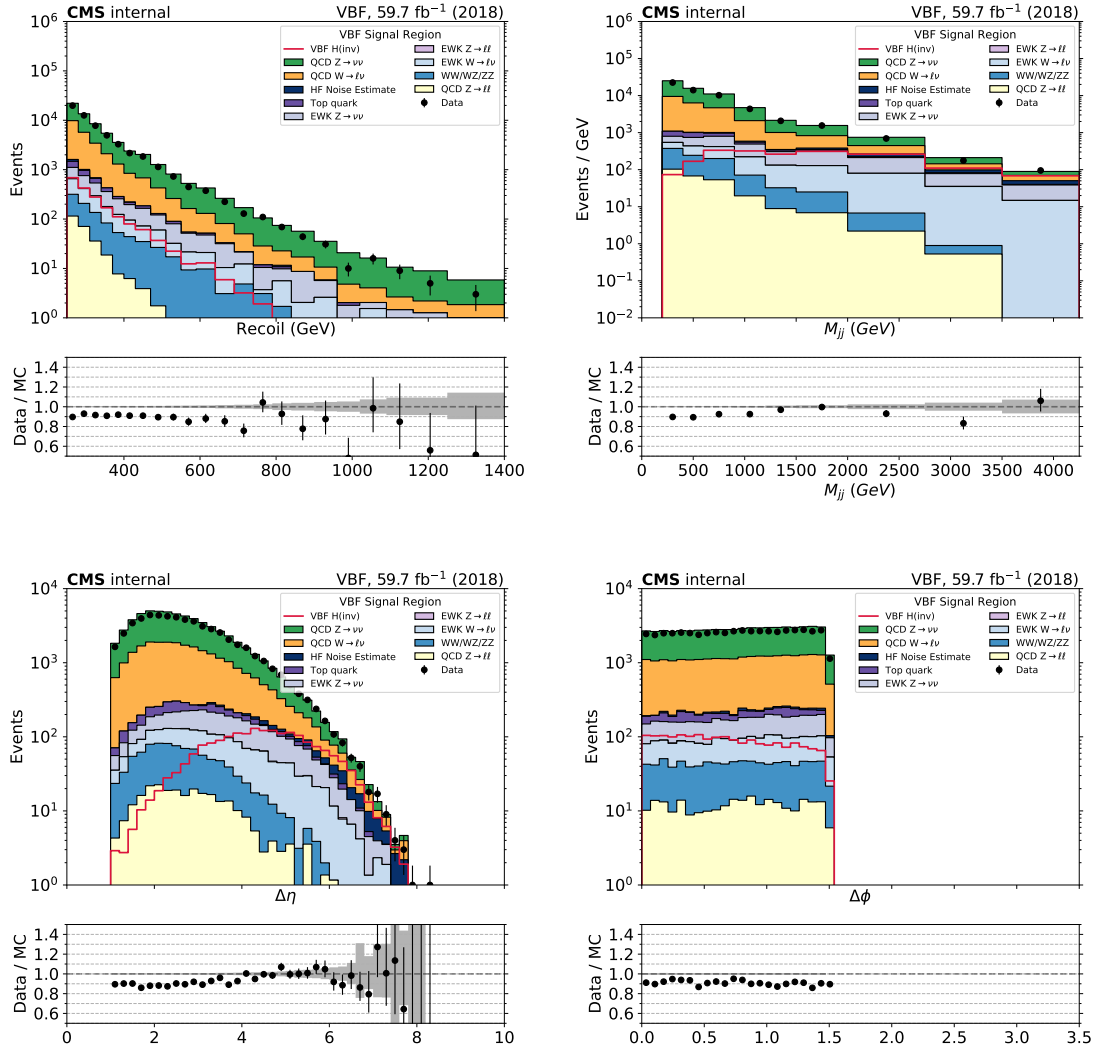


**Figure 3.35:** Recoil distribution,  $M_{jj}$  distribution,  $\Delta\eta_{jj}$  and  $\Delta\phi_{jj}$  distribution in the VBF signal region, using 2018 dataset.

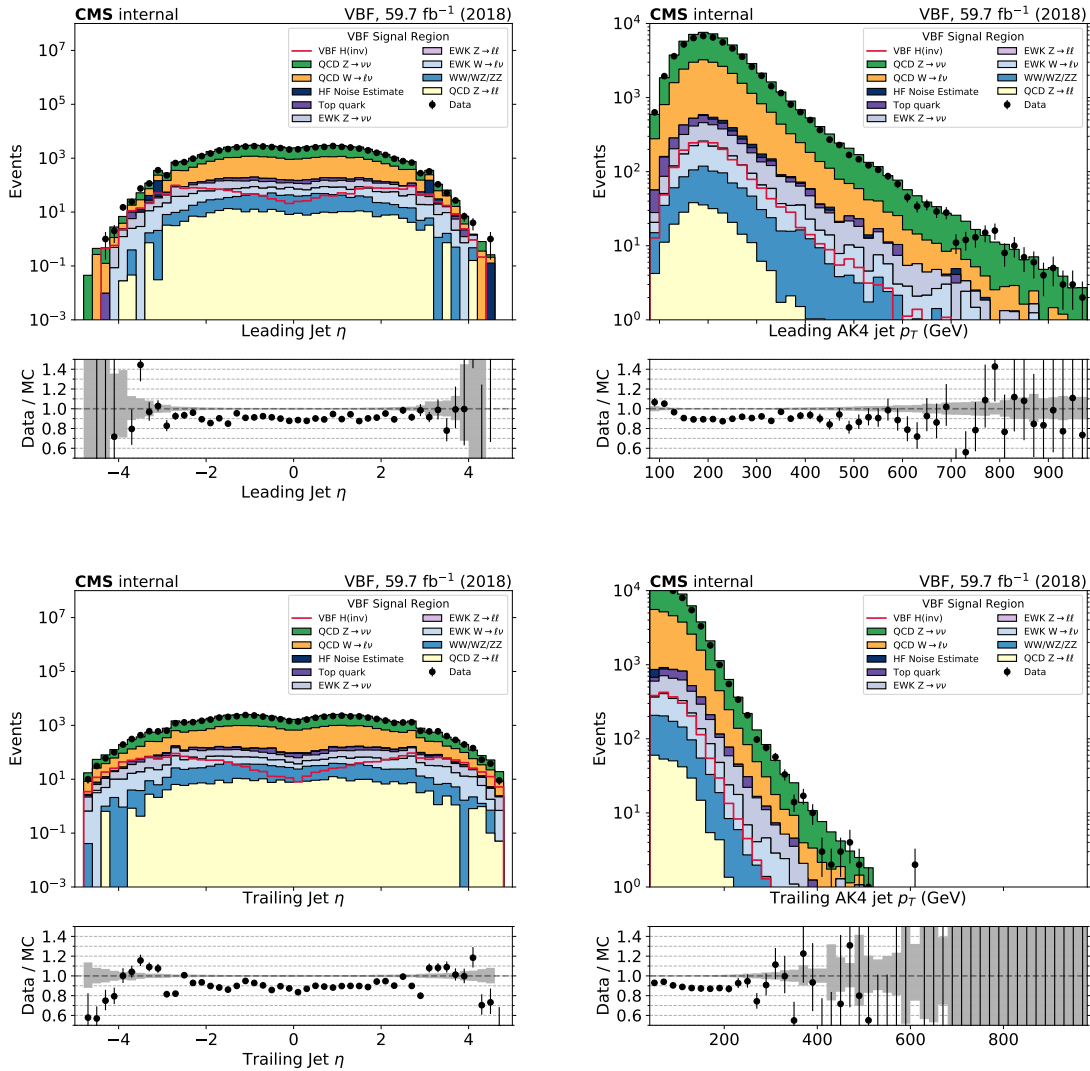


**Figure 3.36:** Leading and subleading jets  $p_T$  and  $\eta$  in the VBF signal region, using 2018 dataset.

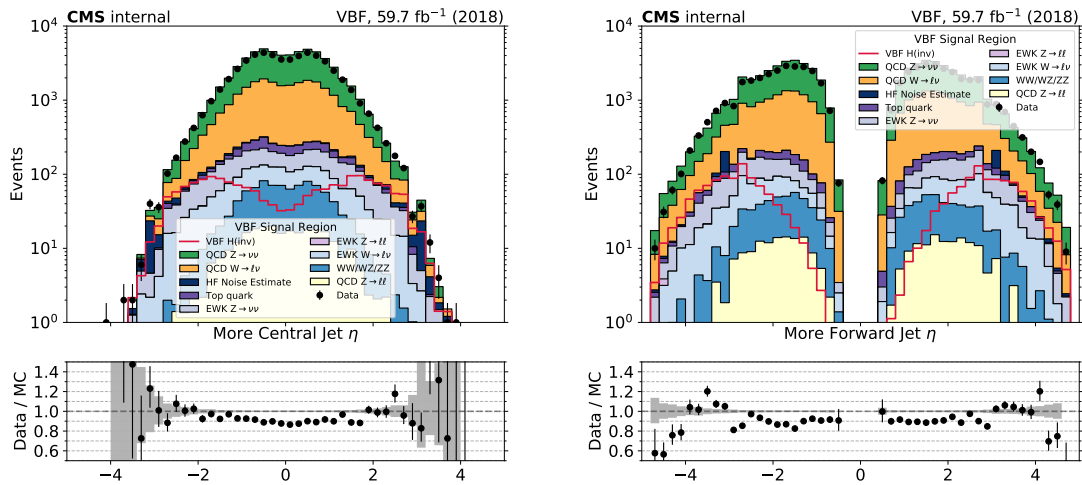


**Figure 3.37:** Most central (left) and most forward jets (right)  $\eta$  of the VBF pair in the VBF signal region, using 2018 dataset.

### 3.4.2 Single Muon Control Region

Single-muon control region events are selected using full signal region criteria of VBF selection with the exception of the muon veto. The  $p_T^{miss}$  requirement is replaced by an identical requirement on the hadronic recoil, which is defined as the sum of  $\vec{p}_T^{miss}$  and the muon  $\vec{p}_T$  (Eq. 3.2), and thus corresponds to the  $p_T$  of the W boson. In the single-muon control region, exactly one tightly identified, isolated muon with  $p_T > 20$  GeV is required. No additional loose muons or electrons with  $p_T > 10$  GeV are allowed in the event.

Figs. 3.38 and 3.40 show the distributions of the recoil,  $M_{jj}$ ,  $\Delta\eta_{jj}$  and  $\Delta\phi_{jj}$  of the two leading AK4 jets for events in the single muon control region for the VBF category in 2017 and 2018 datasets, respectively. Figs. 3.39 and 3.41 show the distributions of the leading muon  $p_T$  and  $\eta$ , for 2017 and 2018, respectively.

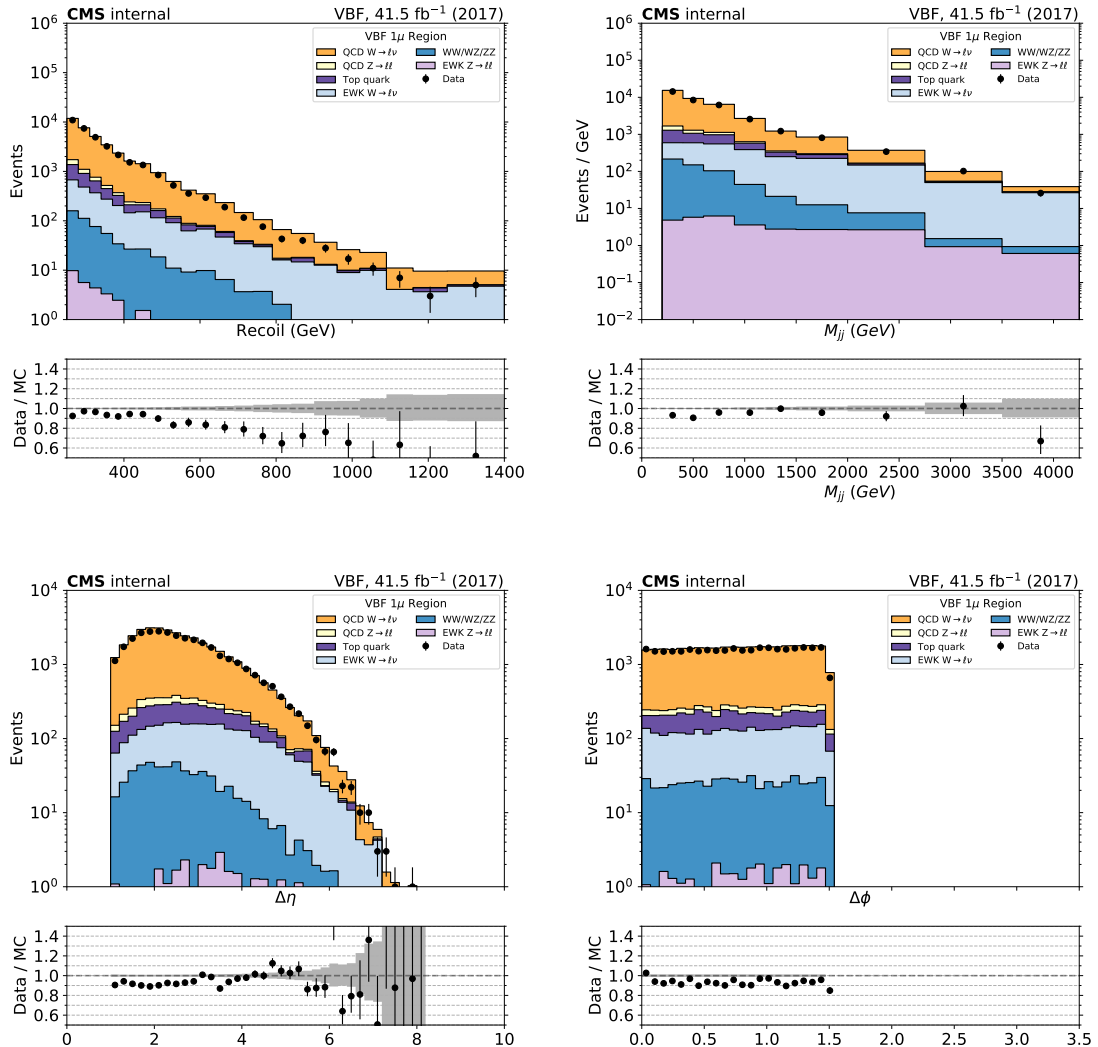


**Figure 3.38:** Comparison between 2017 data and Monte Carlo simulation in the single muon control region for the recoil,  $M_{jj}$  distribution,  $\Delta\eta_{jj}$  and  $\Delta\phi_{jj}$  distributions for the two leading AK4 jets.

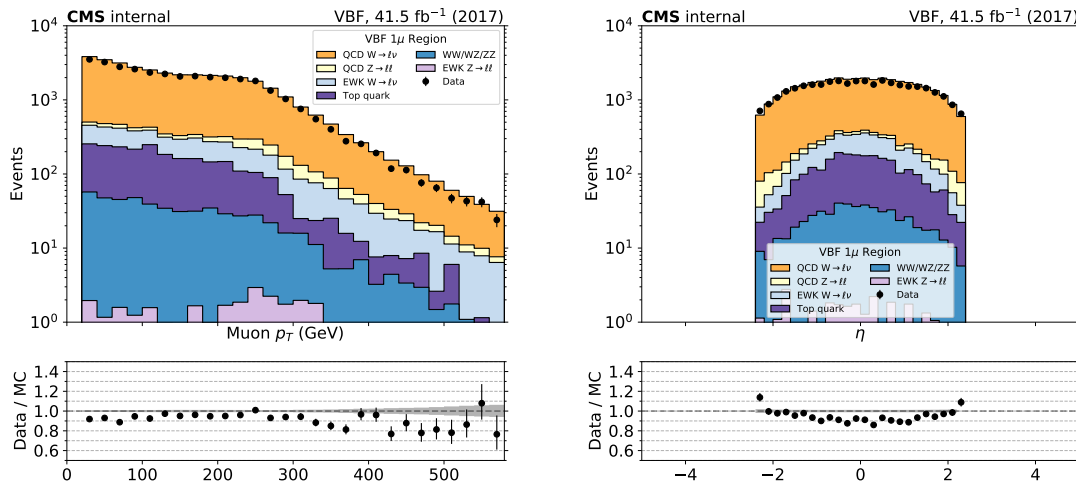


**Figure 3.39:** Comparison between 2017 data and Monte Carlo simulation in the single muon control region for the  $p_T$  and  $\eta$  distribution of the reconstructed muon.

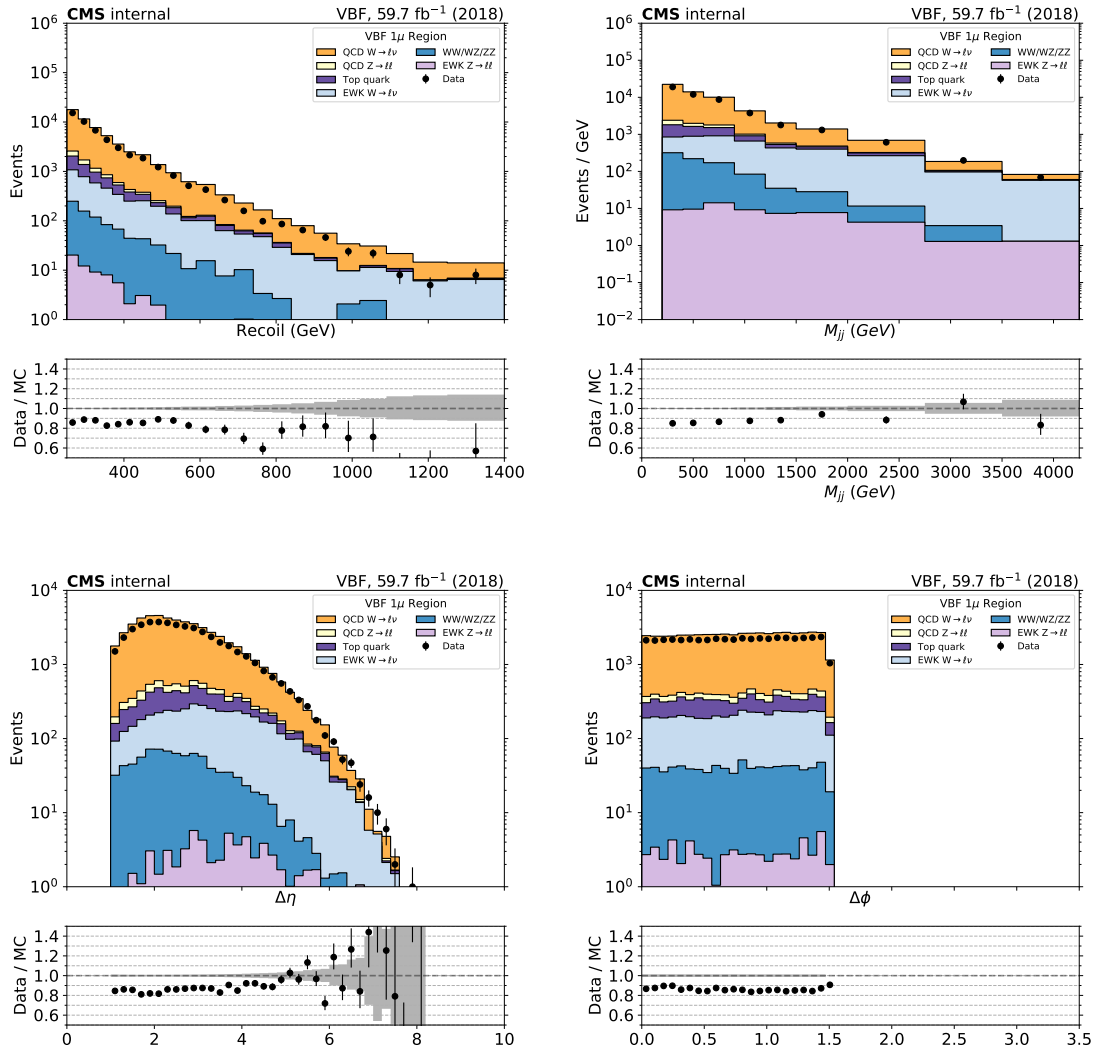


**Figure 3.40:** Comparison between 2018 data and Monte Carlo simulation in the single muon control region for the recoil,  $M_{jj}$  distribution,  $\Delta\eta_{jj}$  and  $\Delta\phi_{jj}$  distributions for the two leading AK4 jets.

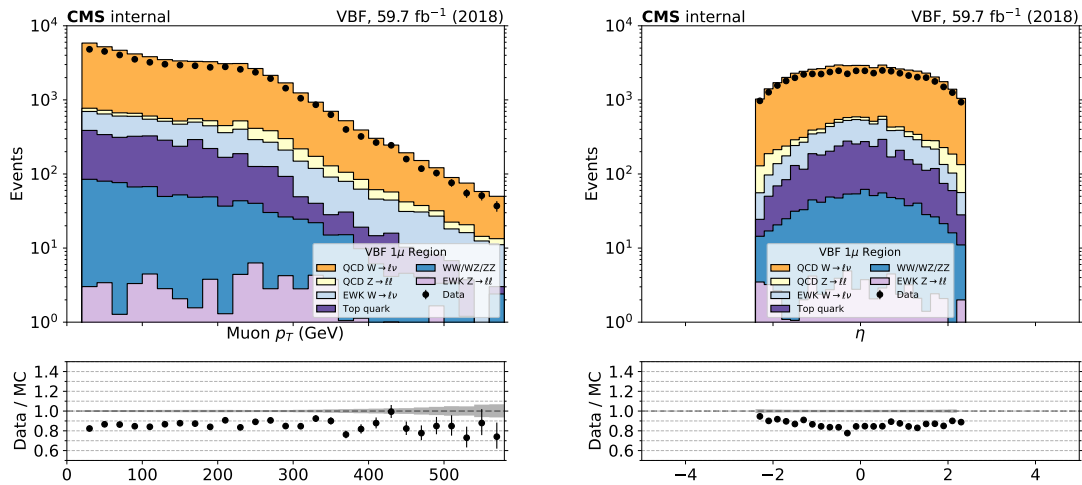


**Figure 3.41:** Comparison between 2018 data and Monte Carlo simulation in the single muon control region for the  $p_T$  and  $\eta$  distribution of the reconstructed muon.

### 3.4.3 Single Electron Control Region

Events for the single-electron control region are collected with the single-electron and photon triggers described in Sec. 3.2.1. Similar to the muon control regions, the  $p_T^{miss}$  requirement is replaced with an identical requirement on the hadronic recoil, which is defined as the sum of  $\vec{p}_T^{miss}$  and the electron  $\vec{p}_T$  (Eq. 3.2), and thus corresponds to the  $p_T$  of the W boson. The events in the single-electron control region are required to contain exactly one tightly identified and isolated electron with  $p_T > 40$  GeV. In addition, the contamination from QCD multijet events in this control region is suppressed by requiring  $p_T^{miss} > 80$  GeV.

Figs. 3.42 and 3.44 show the distributions of the recoil,  $M_{jj}$ ,  $\Delta\eta_{jj}$  and  $\Delta\phi_{jj}$  of the two leading AK4 jets for events in the single-electron control region for the VBF category in 2017 and 2018 datasets, respectively. Figs. 3.43 and 3.45 show the distributions of the leading electron  $p_T$  and  $\eta$ , for 2017 and 2018, respectively.

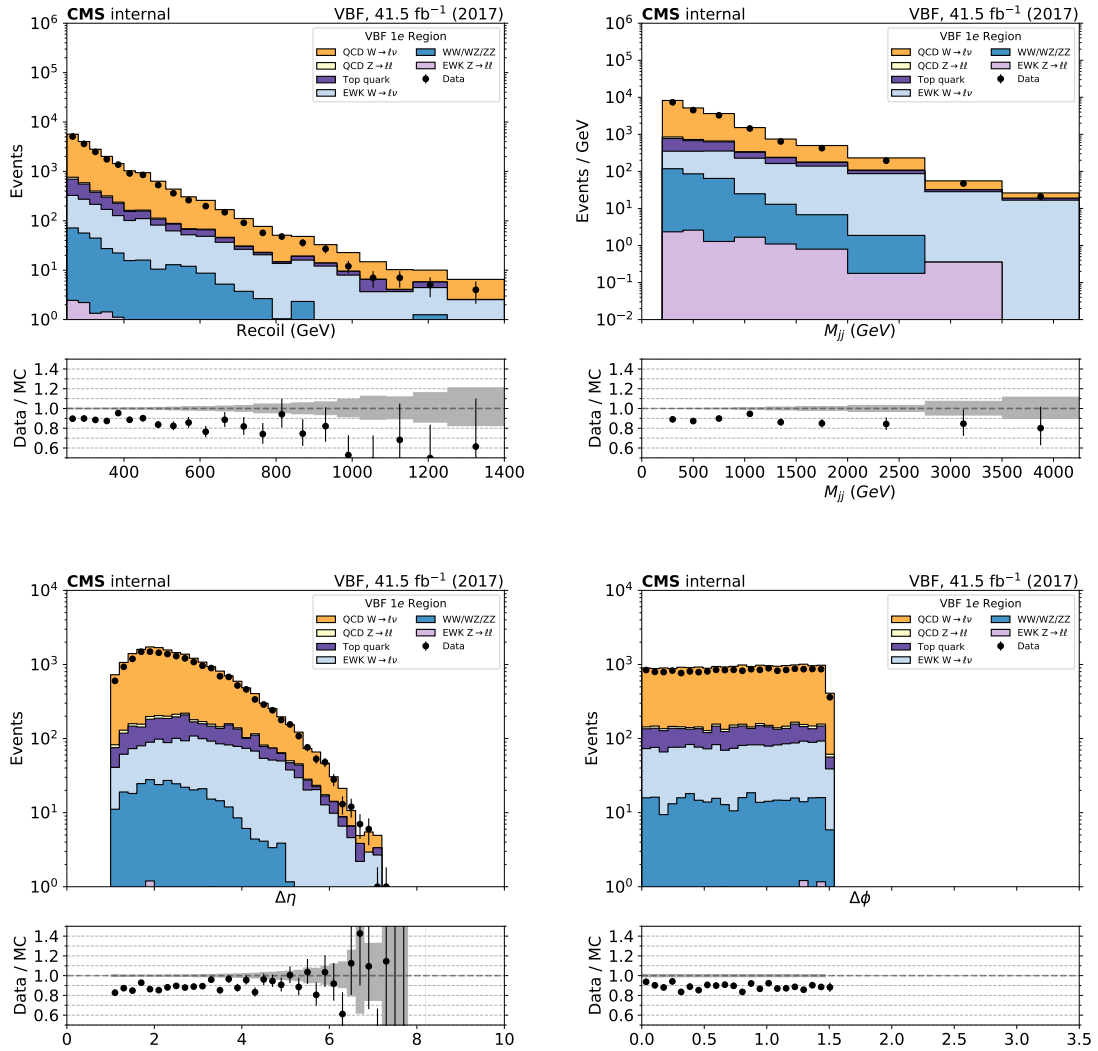


**Figure 3.42:** Comparison between 2017 data and Monte Carlo simulation in the single electron control region for the recoil,  $M_{jj}$  distribution,  $\Delta\eta_{jj}$  and  $\Delta\phi_{jj}$  distributions for the two leading AK4 jets.

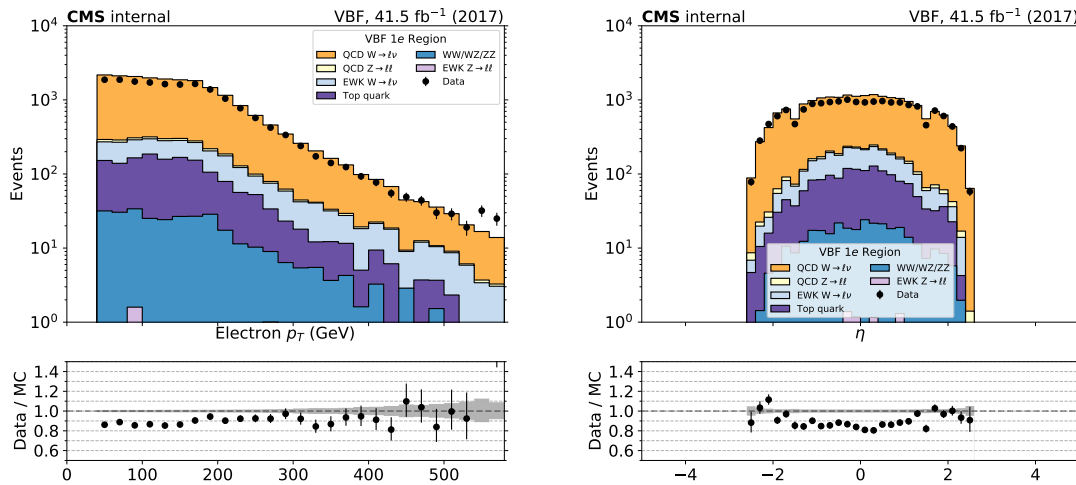


**Figure 3.43:** Comparison between 2017 data and Monte Carlo simulation in the single electron control region for the  $p_T$  and  $\eta$  distribution of the reconstructed electron.

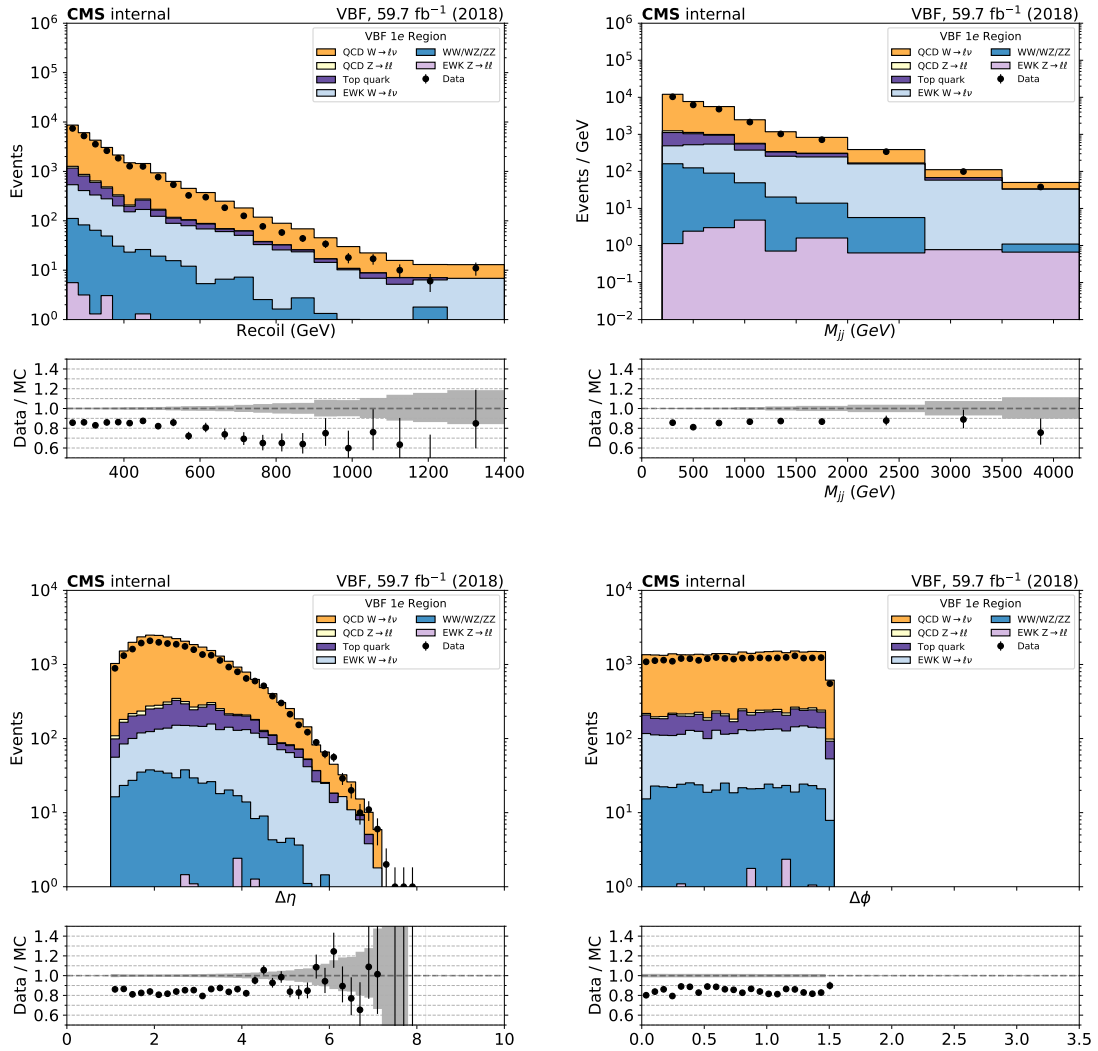


**Figure 3.44:** Comparison between 2018 data and Monte Carlo simulation in the single electron control region for the recoil,  $M_{jj}$  distribution,  $\Delta\eta_{jj}$  and  $\Delta\phi_{jj}$  distributions for the two leading AK4 jets.

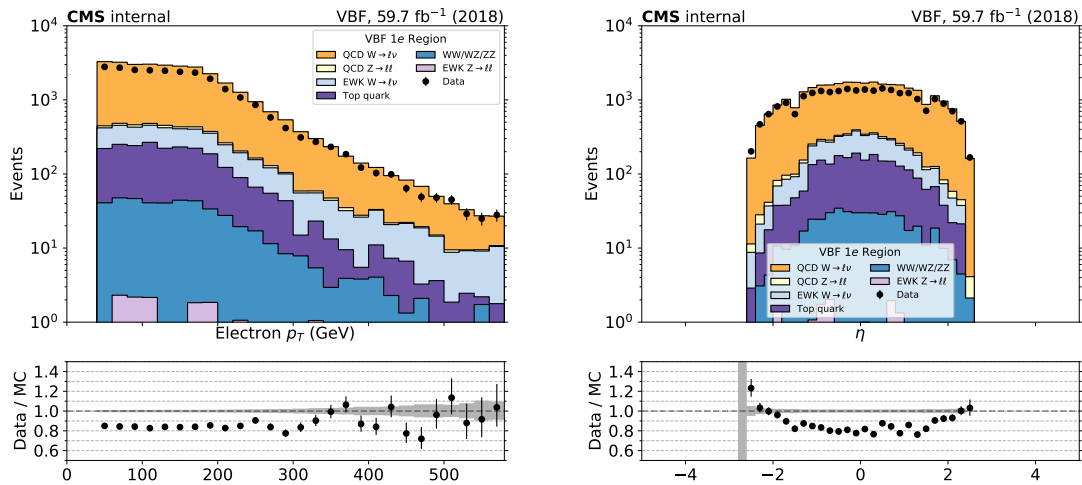


**Figure 3.45:** Comparison between 2018 data and Monte Carlo simulation in the single electron control region for the  $p_T$  and  $\eta$  distribution of the reconstructed electron.

### 3.4.4 Double Muon Control Region

Double-muon control region events are selected using full signal region criteria of VBF category with the exception of the muon veto. In the double-muon control region, events are selected by requiring leading (subleading) muon  $p_T$  greater than 20 (10) GeV and an invariant mass of the two muons is required to be in the range of 60 to 120 GeV, compatible with a  $Z \rightarrow \mu\mu$  decay. At least one of the two muons is required to pass the tight candidate definition, as defined in Sec. 3.1.3. Events are rejected if there is an additional loose muon or electron with  $p_T > 10$  GeV. The SR  $p_T^{miss}$  requirement is replaced with an identical requirement on the hadronic recoil, which is defined as the sum of  $\vec{p}_T^{miss}$  and the muon  $\vec{p}_T$  (Eq. 3.2), and thus corresponds to the distribution of the Z  $p_T$  smeared with the  $p_T^{miss}$  resolution of the detector.

Figs. 3.46 and 3.48 show the distributions of the recoil,  $M_{jj}$ ,  $\Delta\eta_{jj}$  and  $\Delta\phi_{jj}$  of the two leading AK4 jets for events in the double-muon control region for the VBF category in 2017 and 2018 datasets, respectively. Figs. 3.47 and 3.49 show the distributions of the leading muon  $p_T$  and  $\eta$ , as well as the dimuon mass and minimum  $\Delta\phi$  between 4 leading jets and recoil, for 2017 and 2018, respectively.

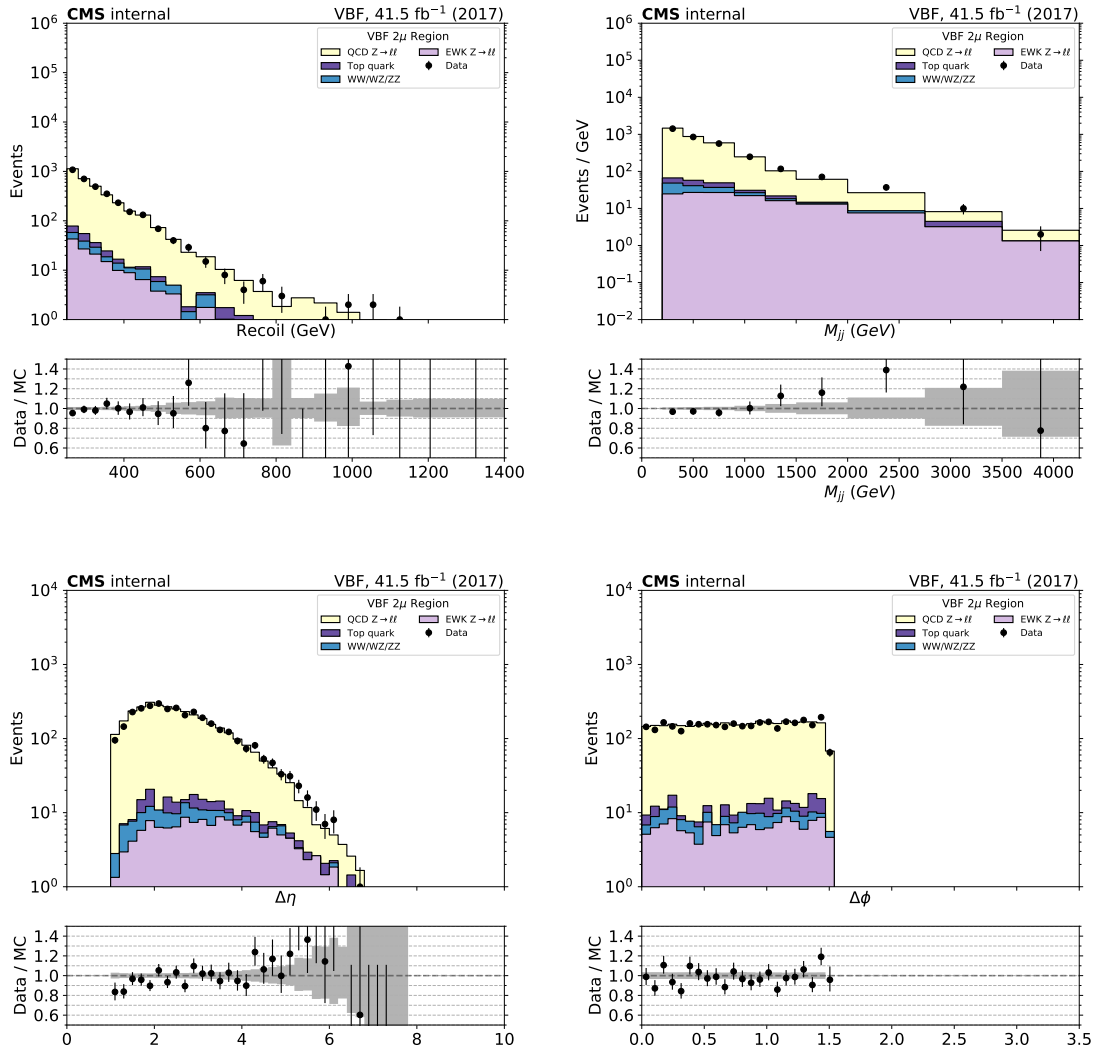


**Figure 3.46:** Comparison between 2017 data and Monte Carlo simulation in the double muon control region for the recoil,  $M_{jj}$  distribution,  $\Delta\eta_{jj}$  and  $\Delta\phi_{jj}$  distributions for the two leading AK4 jets.

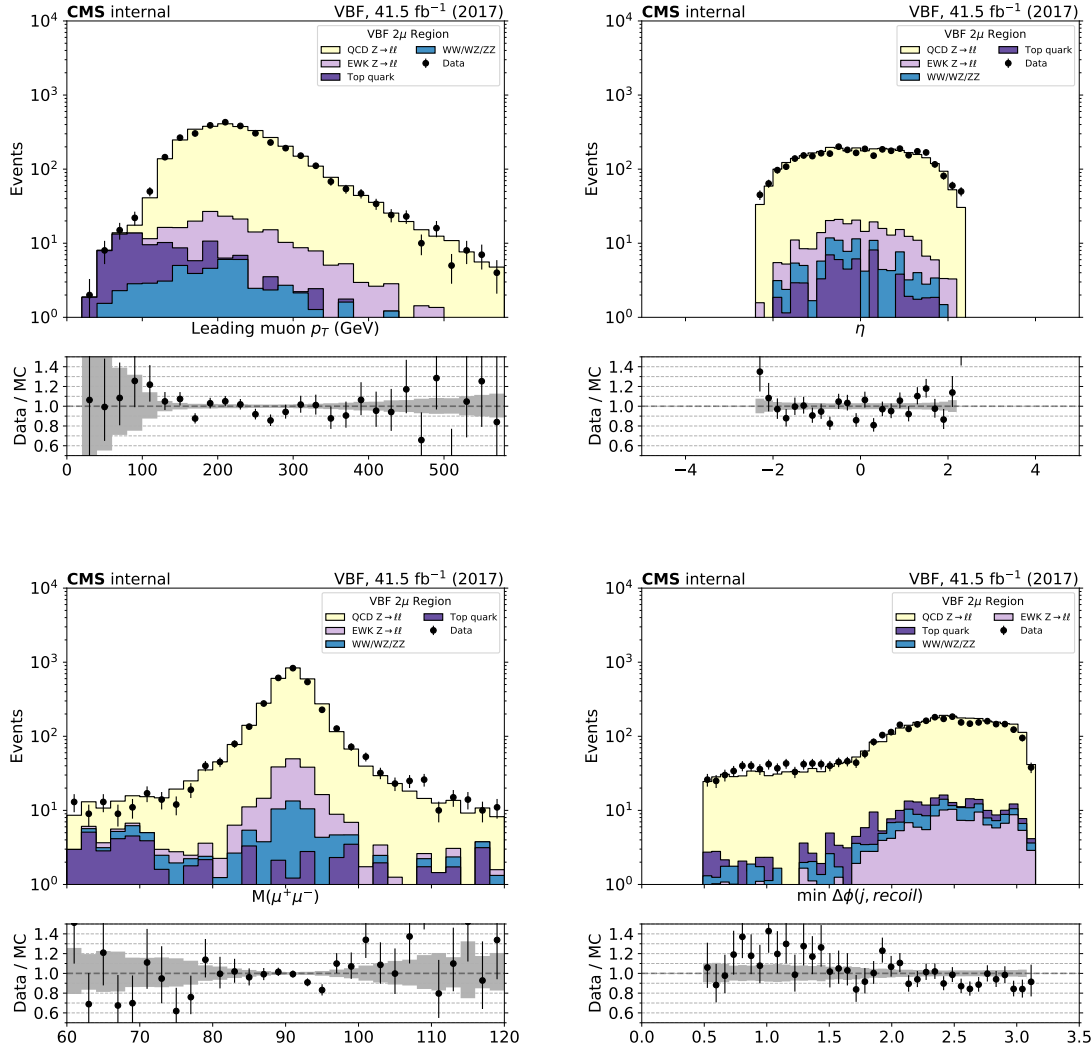


**Figure 3.47:** Comparison between 2017 data and Monte Carlo simulation in the double muon control region for the  $p_T$  and  $\eta$  of the leading muon (top), dimuon mass and minimum  $\Delta\phi$  between 4 leading jets and recoil (bottom).

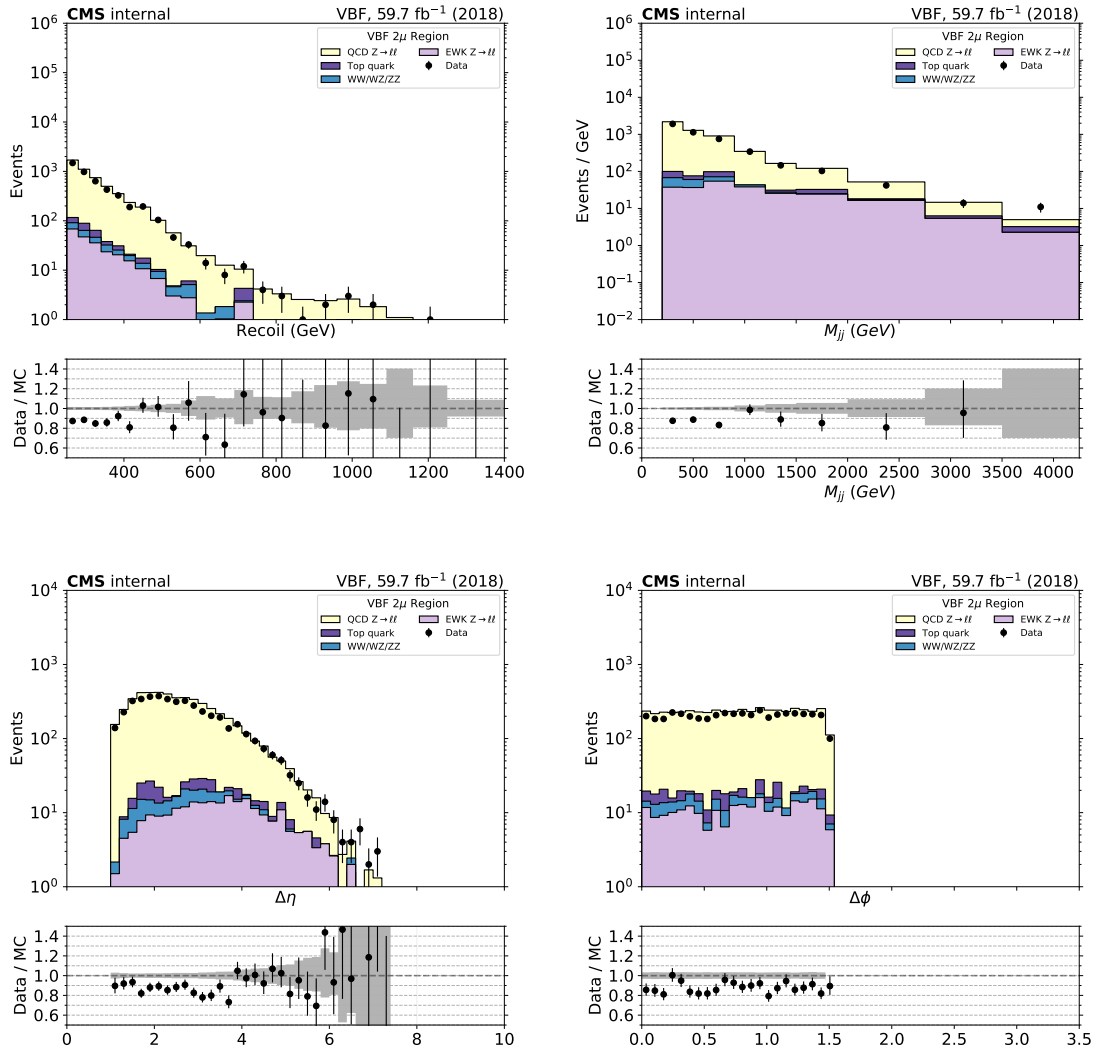


**Figure 3.48:** Comparison between 2018 data and Monte Carlo simulation in the double muon control region for the recoil,  $M_{jj}$  distribution,  $\Delta\eta_{jj}$  and  $\Delta\phi_{jj}$  distributions for the two leading AK4 jets.

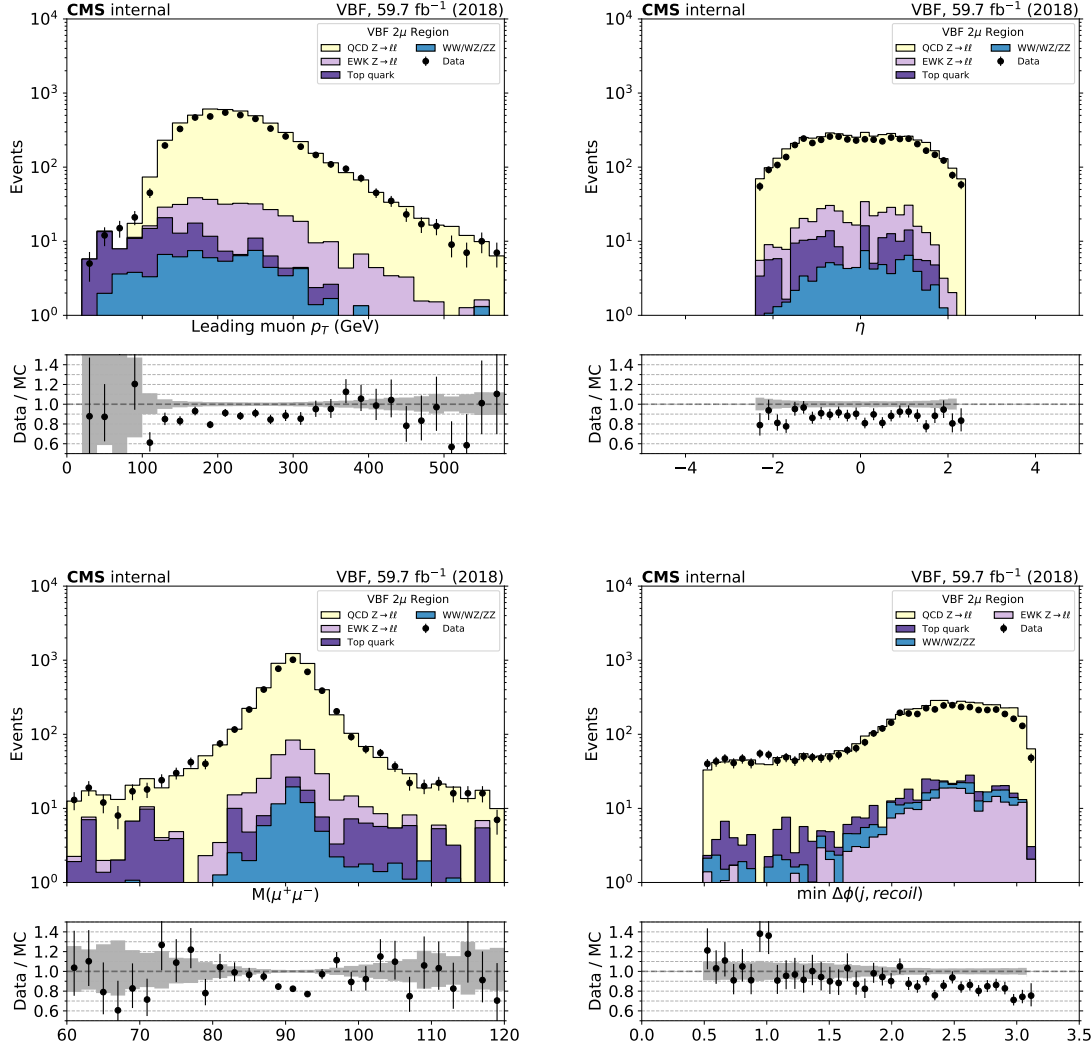


**Figure 3.49:** Comparison between 2018 data and Monte Carlo simulation in the double muon control region for the  $p_T$  and  $\eta$  of the leading muon (top), dimuon mass and minimum  $\Delta\phi$  between 4 leading jets and recoil (bottom).

### 3.4.5 Double Electron Control Region

Events for the double-electron control region are collected with the single-electron and photon triggers described in Sec. 3.2.1. In the offline analysis, events in the dielectron control region are required to contain exactly two oppositely charged electrons with leading (trailing) electron  $p_T$  greater than 40 (10) GeV, with at least one of the two passing the tight candidate definition, as defined in Sec. 3.1.3. Similar to the double muon region, the invariant mass of the electron-positron pair is required to be in the range of 60 to 120 GeV, thus being compatible with a  $Z \rightarrow ee$  decay. The SR  $p_T^{miss}$  requirement is replaced with an identical requirement on the hadronic recoil, which is defined as the sum of  $\vec{p}_T^{miss}$  and the muon  $\vec{p}_\text{T}$  (Eq. 3.2), and thus corresponds to the distribution of the Z  $p_T$  smeared with the  $p_T^{miss}$  resolution.

Figs. 3·50 and 3·52 show the distributions of the recoil,  $M_{jj}$ ,  $\Delta\eta_{jj}$  and  $\Delta\phi_{jj}$  for the two leading AK4 jets for events in the double-electron control region for the VBF category in 2017 and 2018 datasets, respectively. Figs. 3·51 and 3·53 show the distributions of the leading electron  $p_T$  and  $\eta$ , as well as the dielectron mass and minimum  $\Delta\phi$  between 4 leading jets and recoil, for 2017 and 2018, respectively.

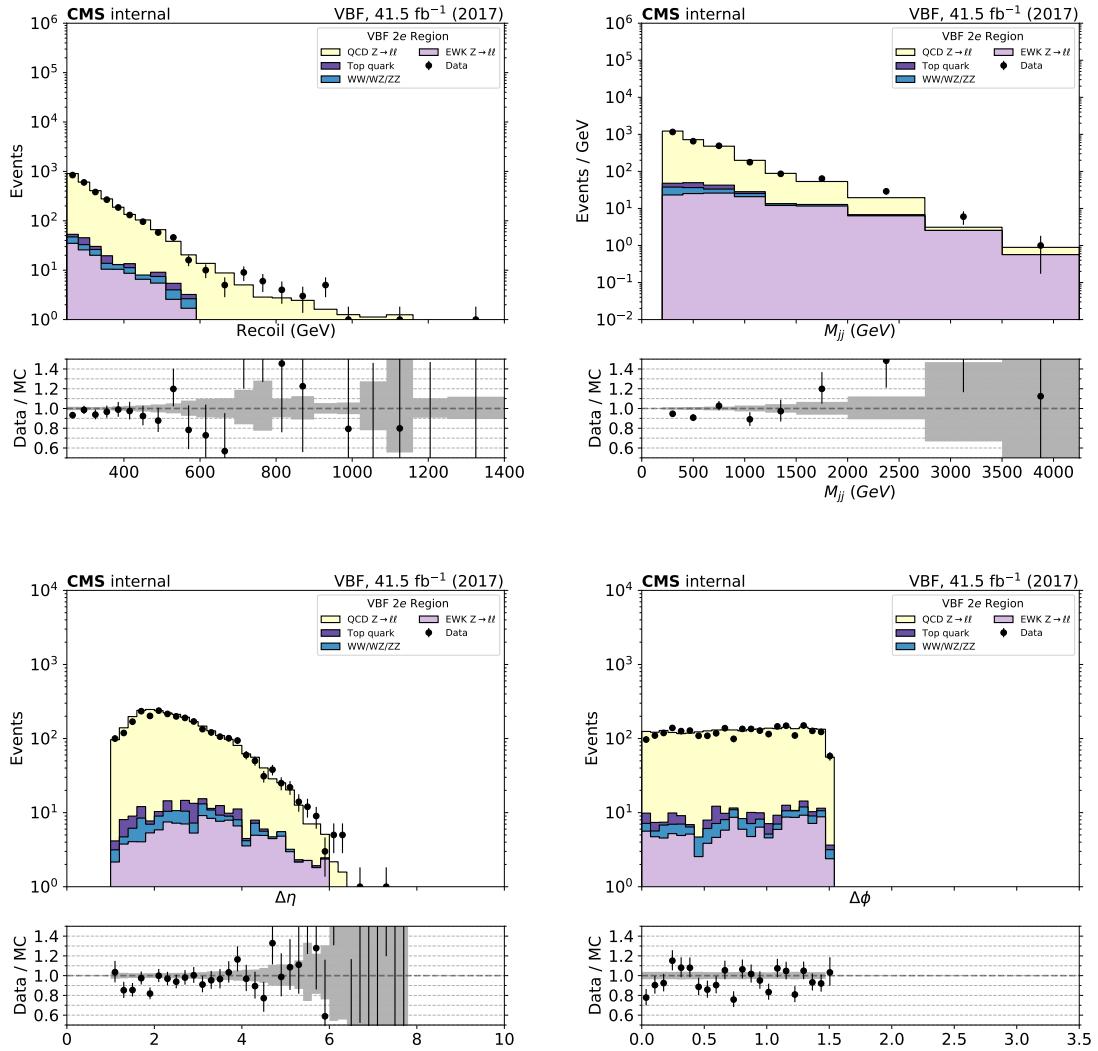


**Figure 3.50:** Comparison between 2017 data and Monte Carlo simulation in the double electron control region for the recoil,  $M_{jj}$  distribution,  $\Delta\eta_{jj}$  and  $\Delta\phi_{jj}$  distributions for the two leading AK4 jets.

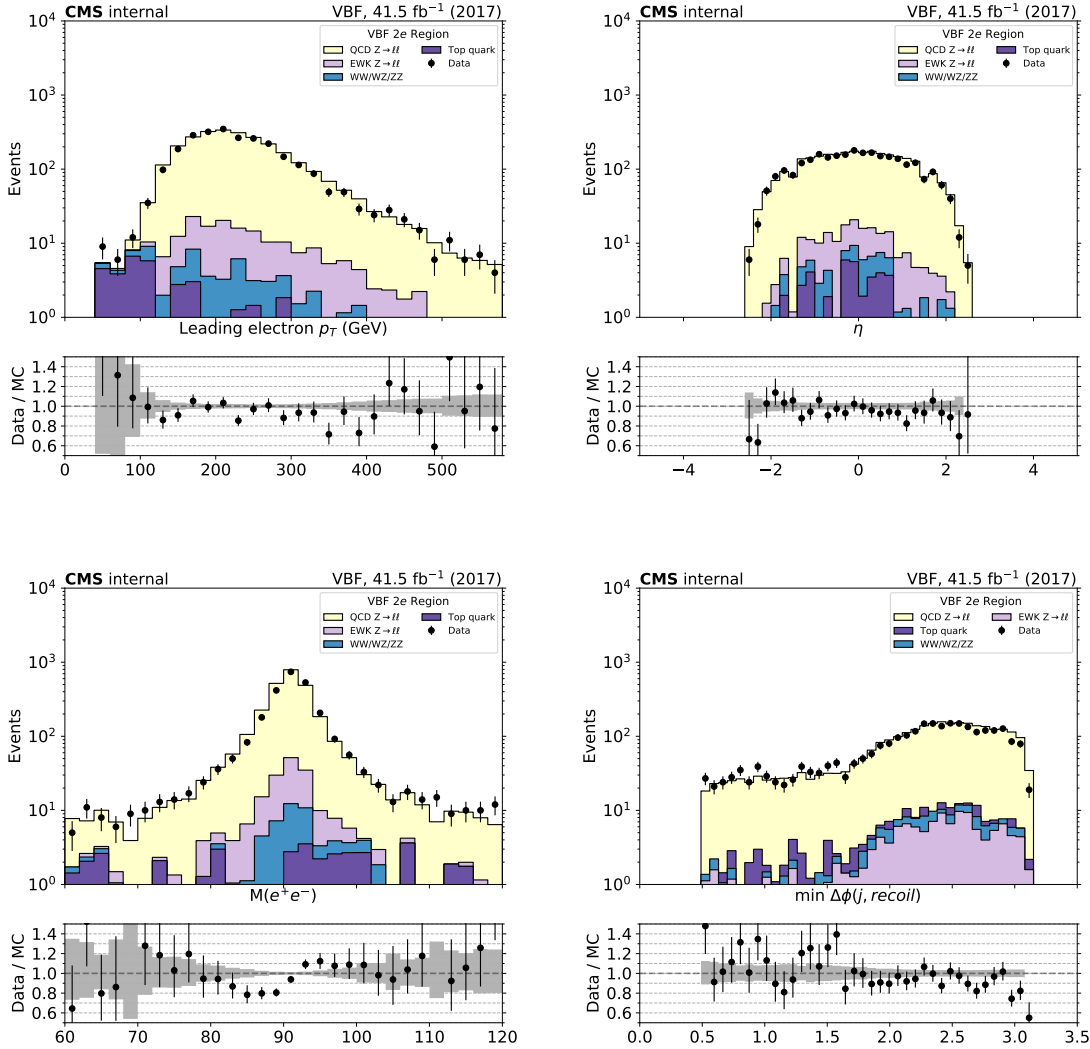


**Figure 3.51:** Comparison between 2017 data and Monte Carlo simulation in the double electron control region for the  $p_T$  and  $\eta$  of the leading electron (top), dielectron mass and minimum  $\Delta\phi$  between 4 leading jets and recoil (bottom).

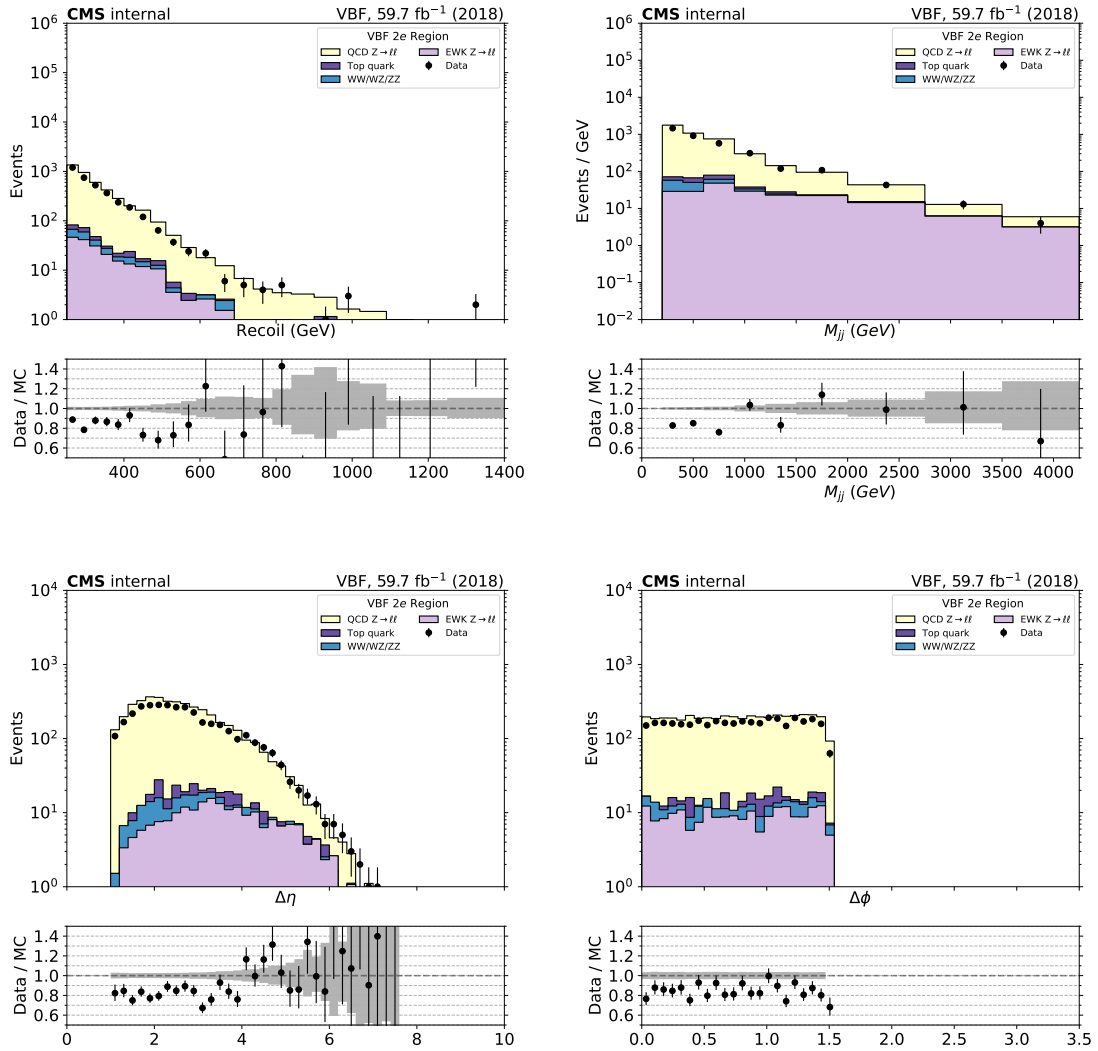


**Figure 3.52:** Comparison between 2018 data and Monte Carlo simulation in the double electron control region for the recoil,  $M_{jj}$  distribution,  $\Delta\eta_{jj}$  and  $\Delta\phi_{jj}$  distributions for the two leading AK4 jets.

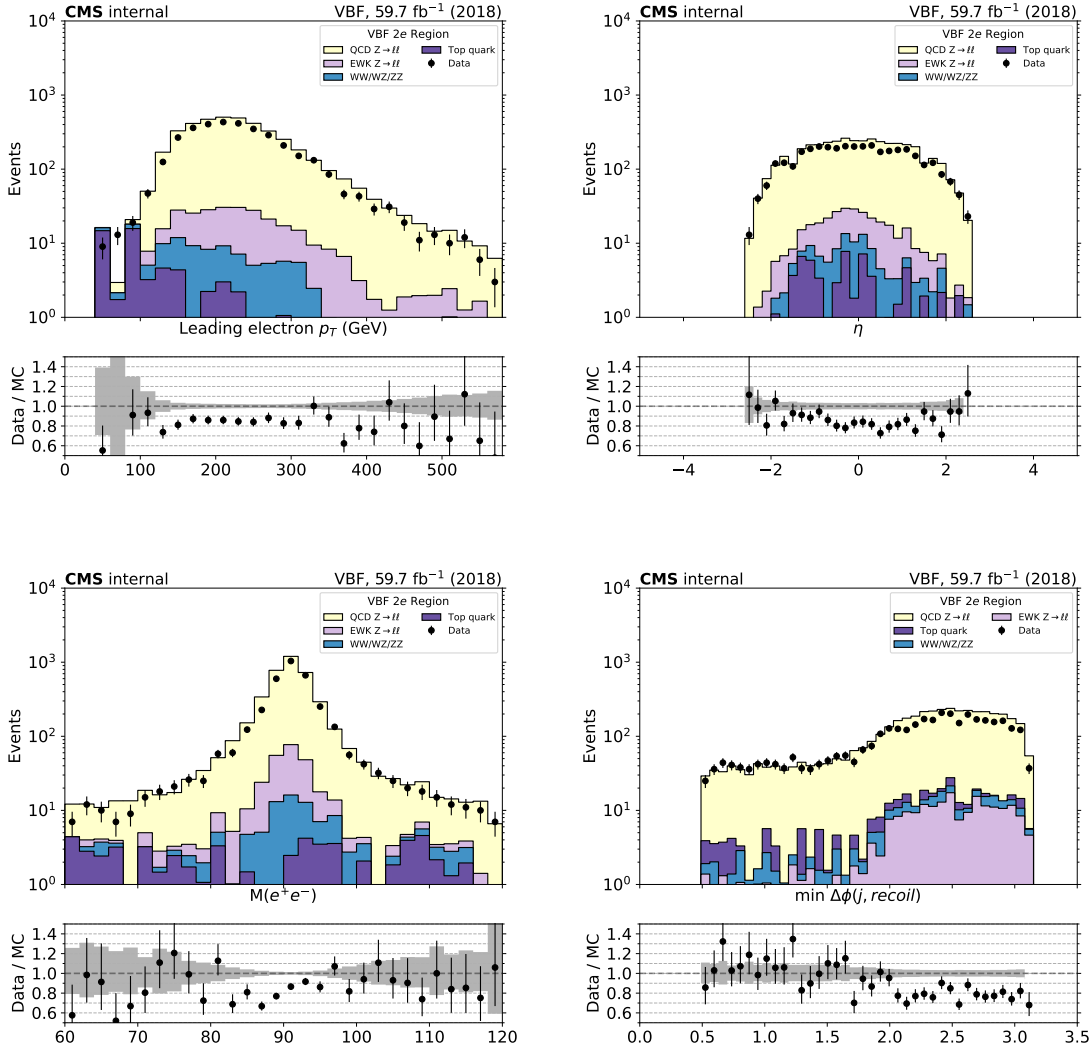


**Figure 3.53:** Comparison between 2018 data and Monte Carlo simulation in the double electron control region for the  $p_T$  and  $\eta$  of the leading electron (top), dielectron mass and minimum  $\Delta\phi$  between 4 leading jets and recoil (bottom).

### 3.4.6 Photon Control Region

To further constrain the  $Z \rightarrow \nu\nu$  background in the signal region, a photon control region is used. At large transverse momenta, the kinematic properties of photon production become similar to those of the  $Z \rightarrow \nu\nu$  process, and can therefore be used to estimate the latter. Events for the control region are selected using a trigger requiring an online photon  $p_T$  of at least 200 GeV. In the offline analysis, photons are required to be located in the barrel part of the detector ( $|\eta| < 1.4442$ ), have transverse momenta of at least 230 GeV to ensure full trigger efficiency, and pass additional identification criteria based on the properties of the associated supercluster in the ECAL, as well as the isolation of the photon relative to nearby energy objects. To be considered for the control region, events must have exactly one such photon, with no additional photons or leptons passing the loose criteria described above. Jets and hadronic recoil are required to pass criteria identical to those imposed in the signal region, where the recoil is defined as the vectorial sum of  $\vec{p}_T^{miss}$  and the photon transverse momentum (Eq. 3.2).

Figs. 3.54 and 3.56 show the distributions of the recoil,  $M_{jj}$ ,  $\Delta\eta_{jj}$  and  $\Delta\phi_{jj}$  distributions of the two leading AK4 jets for events in the photon control region for the VBF category in the 2017 and 2018 datasets, respectively. Similarly, Figs. 3.55 and 3.57 show the distributions of the photon  $p_T$  and  $\eta$ .

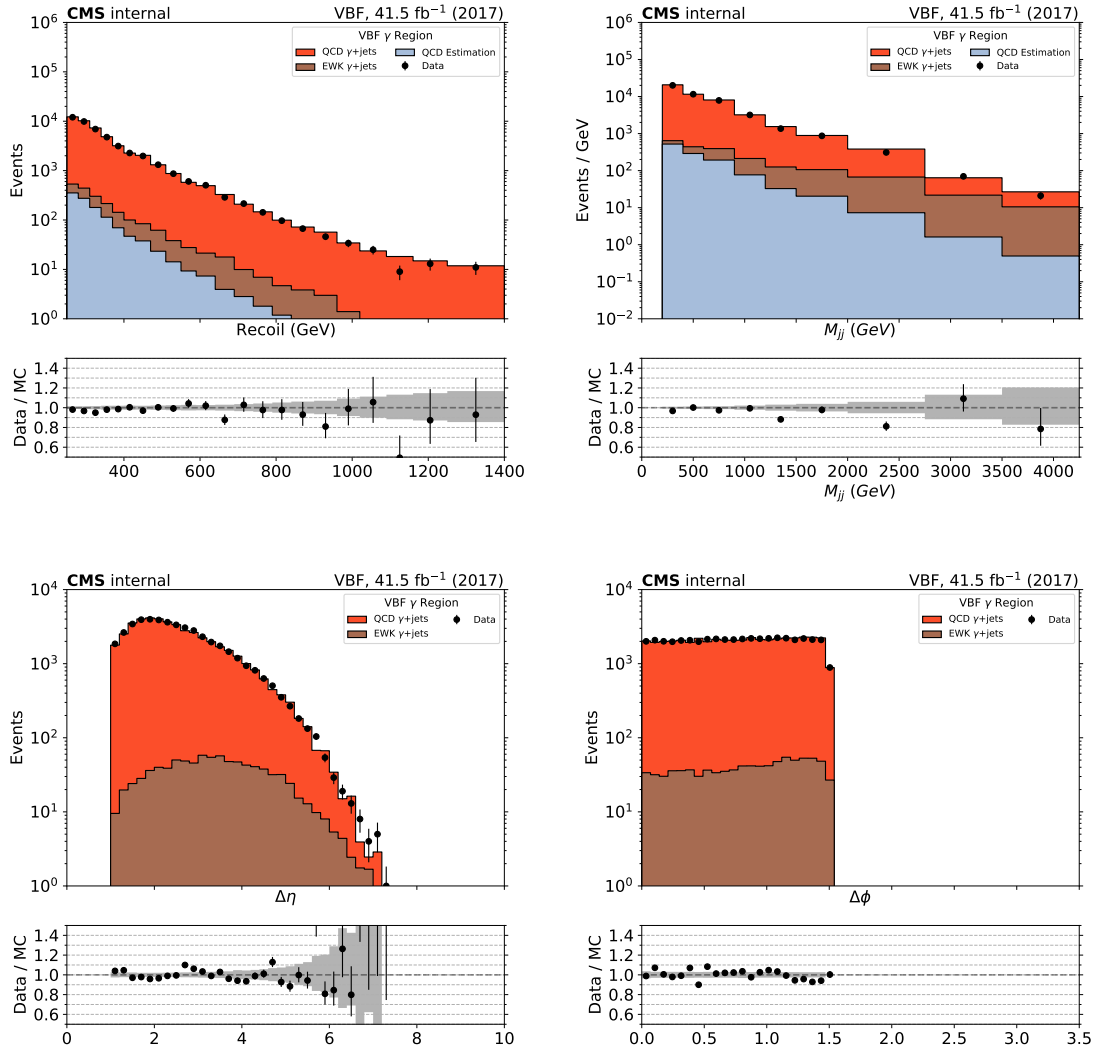


**Figure 3.54:** Comparison between 2017 data and Monte Carlo simulation in the photon control region for the recoil distribution, the  $M_{jj}$  distribution,  $\Delta\eta_{jj}$  distribution and  $\Delta\phi_{jj}$  distribution for the two leading AK4 jets.  $M_{jj}$  and recoil distributions include the QCD estimate calculated from the photon purity measurement, as described in Sec. 3.1.4.

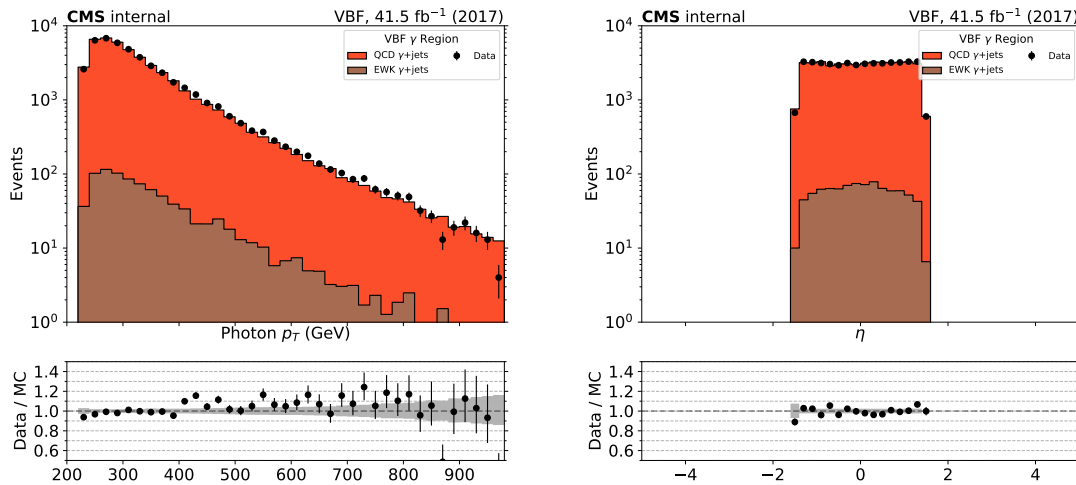


**Figure 3.55:** Comparison between 2017 data and Monte Carlo simulation in the photon control region for the  $p_T$  and  $\eta$  of the leading photon.

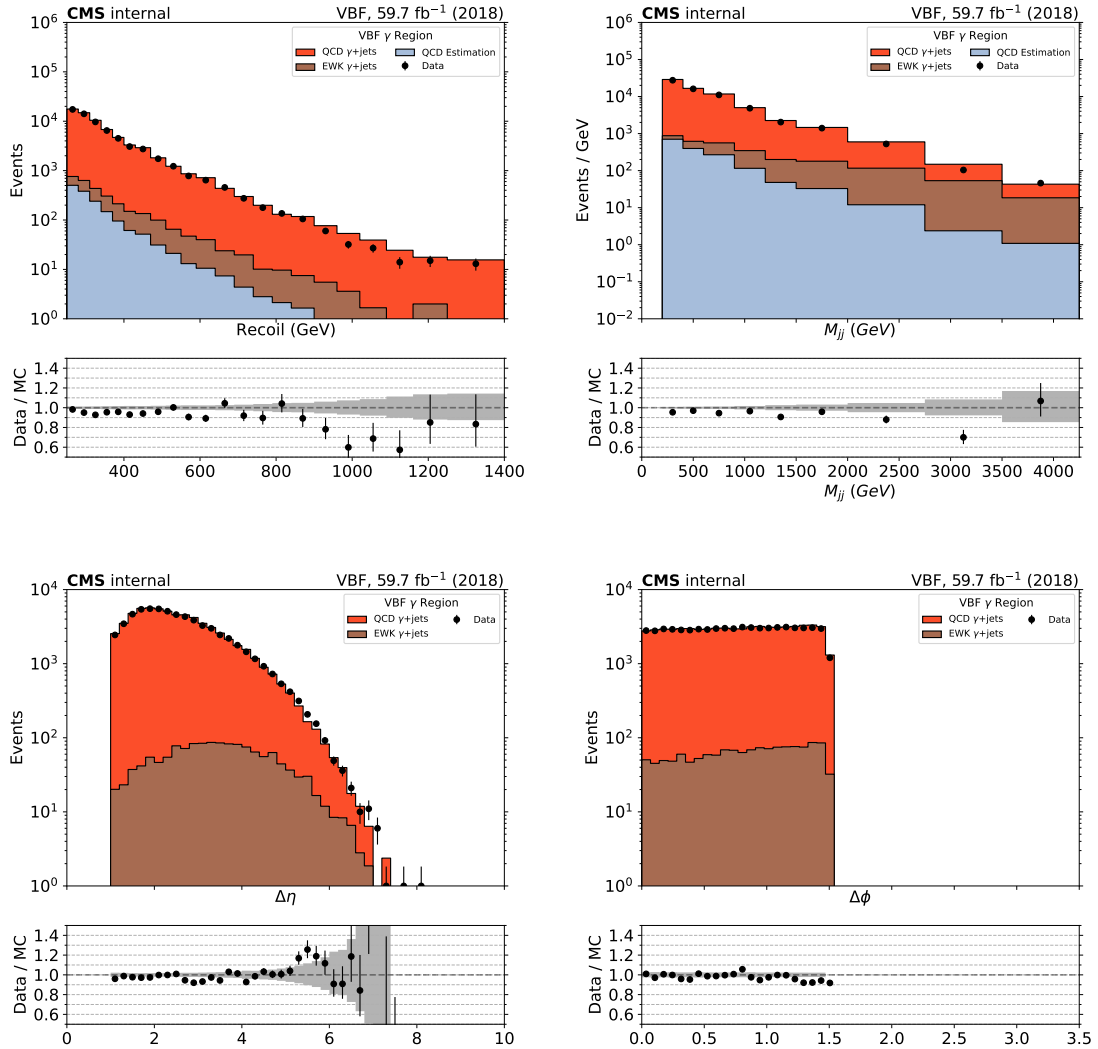


**Figure 3.56:** Comparison between 2018 data and Monte Carlo simulation in the photon control region for the recoil distribution, the  $M_{jj}$  distribution,  $\Delta\eta_{jj}$  distribution and  $\Delta\phi_{jj}$  distribution for the two leading AK4 jets.  $M_{jj}$  and recoil distributions include the QCD estimate calculated from the photon partiy measurement, as described in Sec. 3.1.4.

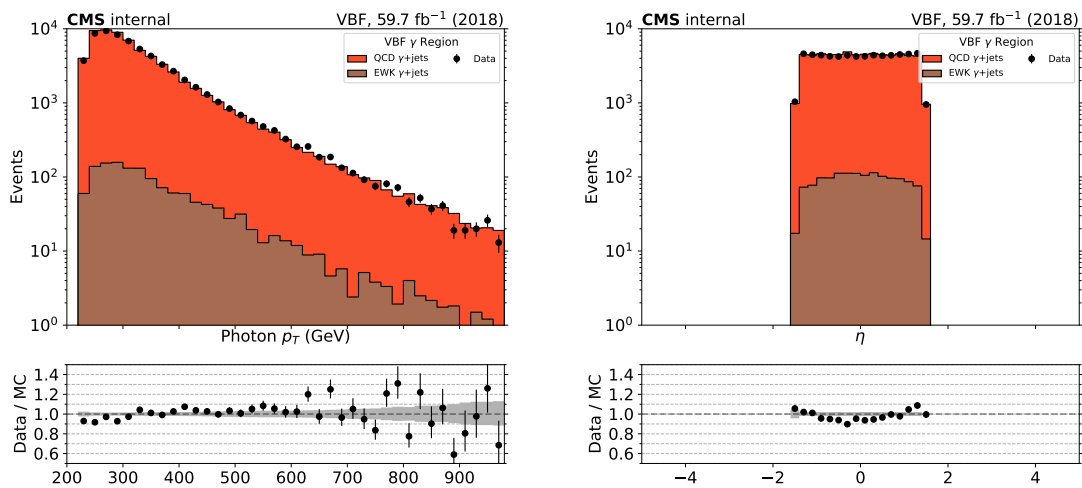


**Figure 3.57:** Comparison between 2018 data and Monte Carlo simulation in the photon control region for the  $p_T$  and  $\eta$  of the leading photon.

### 3.5 Signal extraction strategy

The largest background contributions from  $Z(\nu\nu) + \text{jets}$  and  $W(\ell\nu) + \text{jets}$  processes are estimated using data from five mutually exclusive control regions (CR), which are described in Sec. 3.4. These control regions consist of:

- $W(\mu\nu) + \text{jets}$  region (Sec. 3.4.2)
- $W(e\nu) + \text{jets}$  region (Sec. 3.4.3)
- $Z(\mu\mu) + \text{jets}$  region (Sec. 3.4.4)
- $Z(ee) + \text{jets}$  region (Sec. 3.4.5)
- $\gamma + \text{jets}$  region (Sec. 3.4.6)

$V + \text{jets}$  in the signal region is estimated by performing a simultaneous fit to the data in all signal and control regions, as will be explained in detail in Sec. 3.5.1.

The remaining backgrounds that contribute to the total event yield in the signal region are much smaller than those from  $Z(\nu\nu) + \text{jets}$  and  $W(\ell\nu) + \text{jets}$  processes. These backgrounds include the following:

- QCD multijet events, measured from data using a  $\Delta\phi$  extrapolation method [7].
- Events from forward HCAL (HF) noise, measured from an orthogonal CR as explained in Sec. 3.3.1.
- Top and diboson processes, which are estimated from simulation.

#### 3.5.1 Binned likelihood fit

A binned maximum likelihood fit to the observed data is performed simultaneously across the signal and control regions. For each  $M_{jj}$  bin  $i$  in every region, the expected

yield of events is parametrized as a function of expected strong  $Z(\nu\nu) + \text{jets}$  yields in the signal region, labeled as  $\kappa_i^{\nu\bar{\nu}}$  in the following. This parametrization is done using transfer factors between different  $V + \text{jets}$  processes, as will be explained later in this section. To scale the expected amount of VBF  $H \rightarrow \text{inv.}$  signal (in case of the signal region), a signal strength parameter  $\mu$  is also introduced to the fit, and left freely floating. The resulting likelihood function is shown in Eq. 3.13.

$$\begin{aligned}
\mathcal{L}(\mu, \kappa^{\nu\bar{\nu}}, \boldsymbol{\theta}) = & \prod_i P \left( d_i \middle| B_i(\boldsymbol{\theta}) + Z_i(\kappa_i^{\nu\bar{\nu}}) + W_i(\kappa_i^{\nu\bar{\nu}}, \boldsymbol{\theta}) + \mu S_i(\boldsymbol{\theta}) \right) \\
& \prod_{\text{CR}} \left( \prod_i P \left( d_i^{\text{CR}} \middle| B_i^{\text{CR}}(\boldsymbol{\theta}) + V_i^{\text{CR, strong}}(\kappa_i^{\nu\bar{\nu}}, \boldsymbol{\theta}) + V_i^{\text{CR, VBF}}(\kappa_i^{\nu\bar{\nu}}, \boldsymbol{\theta}) \right) \right) \\
& \prod_j P(\theta_j), \\
Z_i(\kappa_i^{\nu\bar{\nu}}) = & (1 + Z_i^{\frac{\text{VBF}}{\text{strong}}}) \kappa_i^{\nu\bar{\nu}}, \\
W_i(\kappa_i^{\nu\bar{\nu}}, \boldsymbol{\theta}) = & (f_i^{\text{W/Z, strong}}(\boldsymbol{\theta}) + Z_i^{\frac{\text{VBF}}{\text{strong}}} f_i^{\text{W/Z, VBF}}(\boldsymbol{\theta})) \kappa_i^{\nu\bar{\nu}}, \\
V_i^{\text{CR, strong}}(\kappa_i^{\nu\bar{\nu}}, \boldsymbol{\theta}) = & C_i^{\text{CR, strong}}(\boldsymbol{\theta}) R_i^{\text{CR}}(\boldsymbol{\theta}) \kappa_i^{\nu\bar{\nu}}, \\
V_i^{\text{CR, VBF}}(\kappa_i^{\nu\bar{\nu}}, \boldsymbol{\theta}) = & C_i^{\text{CR, VBF}}(\boldsymbol{\theta}) Z_i^{\frac{\text{VBF}}{\text{strong}}} R_i^{\text{CR}}(\boldsymbol{\theta}) \kappa_i^{\nu\bar{\nu}}, 
\end{aligned} \tag{3.13}$$

where  $P(x|y) = y^x e^{-y}/x!$ .  $d_i^{\text{CR}}$  and  $d_i$  are the observed number of events in each bin  $i$  of the  $M_{jj}$  distribution in the CRs and SR, respectively. The index  $i$  runs over the  $M_{jj}$  bins in all regions and data taking years (i.e. 2017 and 2018).

In a given bin,  $V + \text{jets}$  background yields expected in the SR are obtained from transfer factors relating the yields in different CRs to the yields in the SR, denoted as  $R_i^{\text{CR}}(\boldsymbol{\theta})$ . These transfer factors are obtained from simulation. For the single-lepton (dilepton) CRs, the factor  $R_i^{\text{CR}}(\boldsymbol{\theta})$  refers to the ratio of  $W + \text{jets}$  ( $Z + \text{jets}$ ) yields from the corresponding CR to the SR. In the photon CR, it refers to the ratio of  $\gamma + \text{jets}$  to  $Z(\nu\nu) + \text{jets}$  yields.

In addition, transfer factors are defined between the W ( $\gamma$ ) and the Z processes, separately for the VBF and strong productions, denoted as  $f_i^{W/Z,\text{proc}}(\boldsymbol{\theta})$  ( $f_i^{\gamma/Z,\text{proc}}(\boldsymbol{\theta})$ ), with proc denoting the production mode (strong or VBF). Lastly, a transfer factor allows the relation of the VBF production to the strong production for  $Z(\nu\nu) + \text{jets}$ , denoted as  $Z_i^{\frac{\text{VBF}}{\text{strong}}}$ . The factors  $C_i^{\text{CR,strong}}(\boldsymbol{\theta})$  and  $C_i^{\text{CR,VBF}}(\boldsymbol{\theta})$  are dependent on the CR, with:  $C_i^{(ee,\mu\mu),\text{proc}} = 1$ ,  $C_i^{(e,\mu),\text{proc}} = f_i^{W/Z,\text{proc}}(\boldsymbol{\theta})$ ,  $C_i^{\gamma,\text{proc}} = f_i^{\gamma/Z,\text{proc}}(\boldsymbol{\theta})$ .

The contributions from subleading backgrounds in each region are estimated directly from simulation and they are denoted by  $B_i^{\text{CR}}(\boldsymbol{\theta})$  in the CRs, and  $B_i(\boldsymbol{\theta})$  in the SR. Finally, the likelihood also includes a signal term in which  $S_i$  represents the expected signal prediction from the sum of the main Higgs production mechanisms ( $\text{gg}H$ ,  $\text{qq}H$ ,  $VH$ ,  $t\bar{t}H$ ) assuming SM cross sections, while  $\mu = (\sigma_H/\sigma_H^{\text{SM}})\mathcal{B}(H \rightarrow \text{inv})$  denotes the signal strength parameter, also left freely floating.

Systematic uncertainties are modeled as constrained nuisance parameters  $(\boldsymbol{\theta})$ , with a log-normal distribution for those which affect the overall normalisation of a given process, and Gaussian priors for those which directly affect the transfer factors, indicated by  $P(\theta_j)$  in Eq. 3.13.

## Transfer factors

Transfer factors, derived from simulation, are used to link the yields of the  $Z(\ell\ell) + \text{jets}$ ,  $W(\ell\nu) + \text{jets}$  and  $\gamma + \text{jets}$  processes in the control regions with the  $Z(\nu\nu) + \text{jets}$  and  $W(\ell\nu) + \text{jets}$  background estimates in the signal region. These transfer factors are defined as the ratio of expected yields of the target process in the signal region and the process being measured in the control region. As an example:

$$R_i^{Z(\mu\mu),\text{strong}}(\boldsymbol{\theta}) = \frac{N_{i,MC}^{Z \rightarrow \nu\nu}}{N_{i,MC}^{Z \rightarrow \mu^+\mu^-}}(\boldsymbol{\theta}) \quad (3.14)$$

where  $N_i$  is the number of events in bin  $i$  of the  $M_{jj}$  distribution,  $R_i^{Z(\mu\mu),\text{strong}}(\boldsymbol{\theta})$

is the transfer factor between the strong  $Z(\mu\mu) + \text{jets}$  process yields in dimuon control region and strong  $Z(\nu\nu) + \text{jets}$  background in the signal region. The transfer factor in Eq. 3.14 allows us to write the strong  $Z(\mu\mu) + \text{jets}$  yields in dimuon control region as a function of strong  $Z(\nu\nu) + \text{jets}$  yields in the signal region (i.e.  $\kappa_i^{\nu\bar{\nu}}$  in Eq. 3.13):

$$V_i^{Z(\mu\mu),\text{strong}}(\kappa_i^{\nu\bar{\nu}}, \boldsymbol{\theta}) = R_i^{Z(\mu\mu),\text{strong}}(\boldsymbol{\theta}) \kappa_i^{\nu\bar{\nu}} \quad (3.15)$$

Other transfer factors are constructed in a similar manner, so that all  $V_i^{\text{CR,strong}}$  and  $V_i^{\text{CR,VBF}}$  can be written as a function of  $\kappa_i^{\nu\bar{\nu}}$  and the nuisance parameters,  $\boldsymbol{\theta}$ .

Using this transfer factor formalism,  $Z(\nu\nu) + \text{jets}$  background prediction in the signal region is connected to the yields of  $Z(\mu\mu) + \text{jets}$  and  $Z(ee) + \text{jets}$  events in the dilepton control regions. The associated transfer factors account for the differences in the branching ratio of  $Z$  bosons to charged leptons relative to neutrinos and the impact of lepton acceptance and selection efficiencies. In the case of dielectron events, the transfer factor also takes into account the difference in the trigger efficiencies. The resulting constraint on the  $Z(\nu\nu) + \text{jets}$  background from the dilepton control regions is limited by the statistical uncertainty in the dilepton control regions due to the large branching fraction difference of the  $Z$  boson decays to muons and electrons compared to that to neutrinos.

Similarly,  $W(\ell\nu) + \text{jets}$  background prediction in the signal region is connected to the yields of  $W(\mu\nu) + \text{jets}$  and  $W(e\nu) + \text{jets}$  event yields in single-lepton control regions. These transfer factors take into account the impact of lepton acceptances and efficiencies, lepton veto efficiencies, and the difference in the trigger efficiencies in the case of the single-electron control region.

The transfer factors linking  $Z$  and  $W$  processes in control regions are validated by comparing the ratio of data in different control regions to the predicted ratio in simulation. These transfer factors are shown as a function of  $M_{jj}$  in Fig. 3.58, where

the left column shows the results with 2017 data, and the right column shows the 2018 data.

To further constrain the  $Z(\nu\nu) + \text{jets}$  background and to avoid statistical limitations, the  $Z(\nu\nu) + \text{jets}$  process is also linked to the  $\gamma + \text{jets}$  process in the photon CR, using the same transfer factor scheme as for the control regions with two charged leptons. The transfer factor accounts for all differences in triggering and identification between these two regions. Those transfer factors are shown in Fig. 3.59.

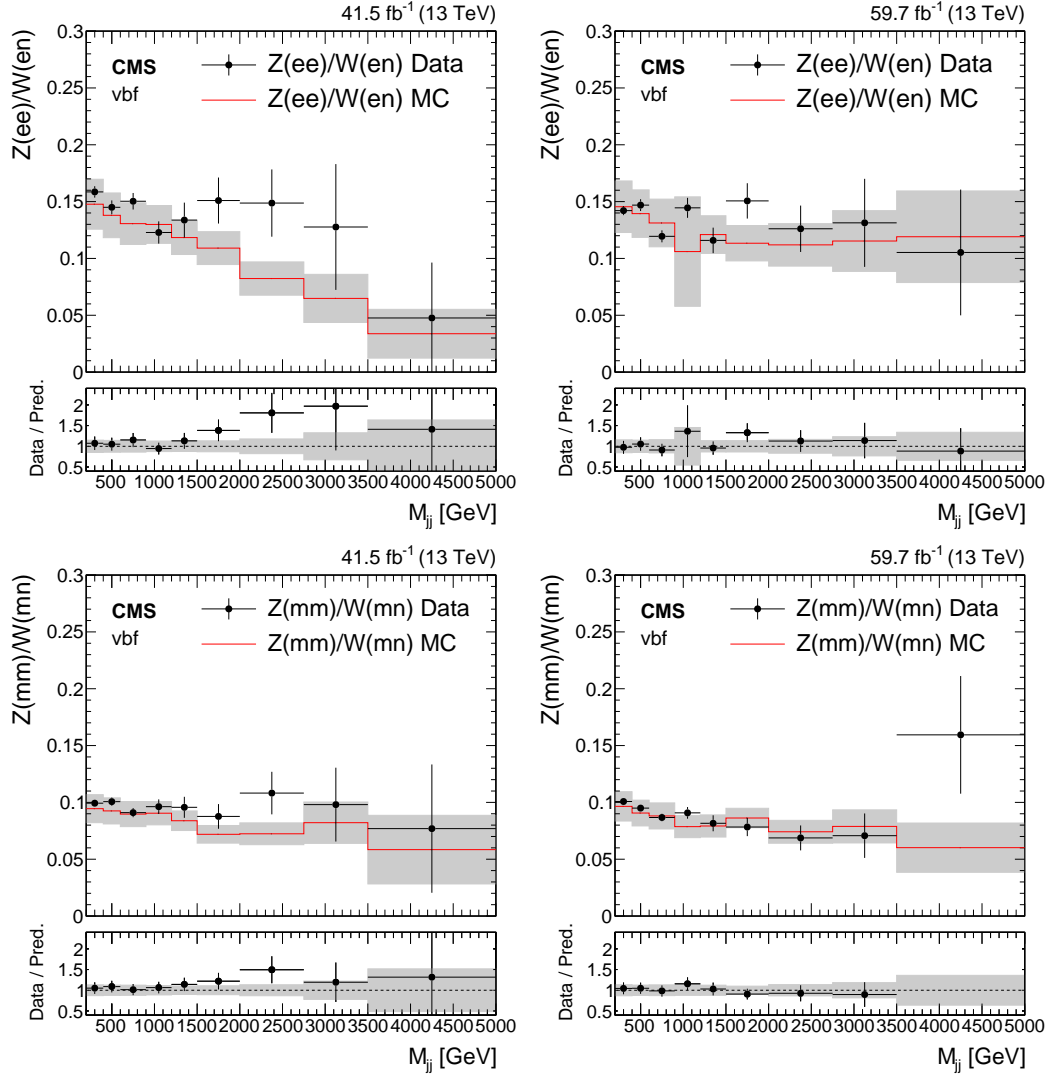


**Figure 3.58:** Transfer factors between  $Z$  and  $W$  control regions as a function of the dijet mass. Results for both 2017 (left) and 2018 (right) datasets are shown. Plots on the top row show the ratios between the electron regions, while the plots on the bottom show the ratios between muon regions. The bands show the theoretical and experimental systematic uncertainties on the ratios.

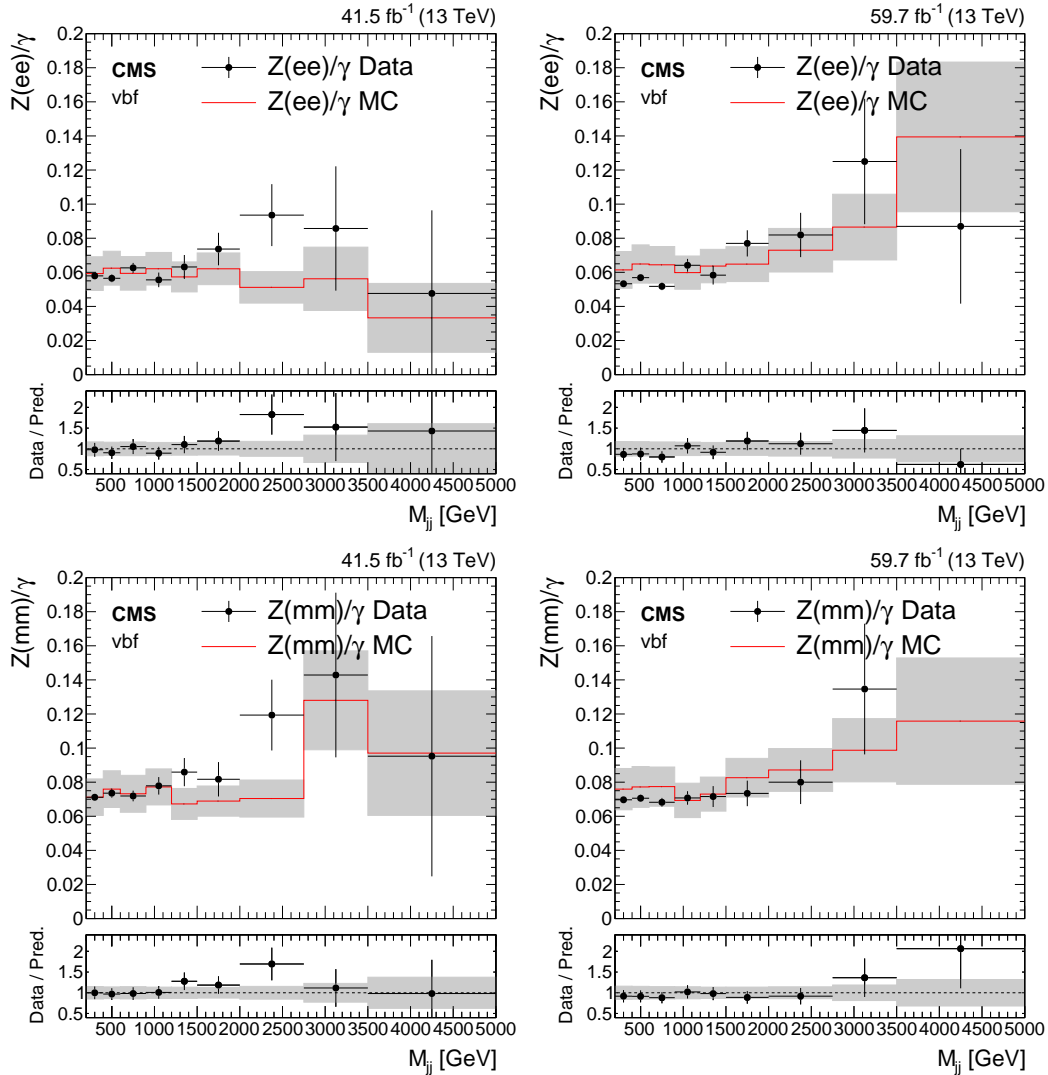


**Figure 3.59:** Transfer factors for  $Z(ee)/\gamma + jet$  (top) and  $Z(mm)/\gamma + jets$  (bottom) processes. Results with 2017 datasets are shown on the left column, and 2018 results are shown on the right column. The bands show the experimental systematic uncertainties on the ratios.

### 3.5.2 Systematic uncertainties

Systematic uncertainties in the transfer factors are modeled as constrained nuisance parameters and include both experimental uncertainties and theoretical uncertainties in  $W + \text{jets}$  to  $Z + \text{jets}$  and  $\gamma + \text{jets}$  to  $Z + \text{jets}$  cross section ratios. Theoretical and experimental uncertainties considered in the analysis are discussed in the following two subsections.

#### Theoretical uncertainties

Theoretical uncertainties in  $W + \text{jets}$ ,  $Z + \text{jets}$  and  $\gamma + \text{jets}$  processes include effects from QCD and EWK higher-order corrections along with the parton distribution function (PDF) modeling uncertainty. One of the uncertainties considered comes from the variations around the central renormalization and factorization scale choice. It is evaluated by taking the differences in the NLO cross section two-dimensionally as a function of boson  $p_T$  and  $M_{jj}$  after changing the renormalization and factorization scales by a factor of two and a factor of one-half with respect to the default value. These constant scale variations mainly affect the overall normalization of the boson  $p_T$  distributions. The PDF uncertainty on the k-factors from the  $p_T/\text{jet}$  binned sample is evaluated using the recommendation from the PDF4LHC authors [45]. This is added in quadrature with uncertainty due to the choice of  $\alpha_s$ . For the photon transfer factor, the procedure is identical with the exception that the uncertainties are estimated one-dimensionally versus boson  $p_T$ .

The scale uncertainties are treated as partially correlated between the  $Z + \text{jets}$  and  $W + \text{jets}$  processes in the following fashion. For a certain scale uncertainty component (e.g. the factorization scale) the  $W/Z$  ratio is evaluated from the  $Z + \text{jets}$  and  $W + \text{jets}$  processes separately and the difference to the nominal calculated. An envelope of the largest uncertainty out of the two processes is taken as the uncertainty on

the ratio. This is done for all of the theoretical uncertainty components on the ratios. It is observed that the contribution from varying the  $W + \text{jets}$  process is the larger uncertainty source, hence taking the envelope equates to taking the  $W + \text{jets}$  uncertainty contribution only and ignoring that from the  $Z$ .

The PDF uncertainties are treated as fully correlated between the  $Z + \text{jets}$  and  $W + \text{jets}$  processes. For up and down variations of the PDF,  $W/Z$  ratio is evaluated by varying the  $W + \text{jets}$  and  $Z + \text{jets}$  processes simultaneously, and the varied  $W/Z$  ratio is calculated accordingly. Both for the scale and PDF uncertainties, a similar correlation scheme is applied while computing the uncertainties for  $\gamma / Z + \text{jets}$  ratio.

The full set of theory uncertainties on the  $W/Z$  and  $\gamma/Z$  ratios are shown in Fig. 3.60. On the top row, the uncertainties for QCD  $W/Z$  ratio (left) and VBF  $W/Z$  ratio (right) are shown. And similarly, on the bottom row, the uncertainties for QCD  $\gamma/Z$  ratio (left) and VBF  $\gamma/Z$  ratio (right) are shown. All uncertainties are shown as a function of the dijet invariant mass,  $M_{jj}$ .

From Fig. 3.60, it can be observed that the dominating theory uncertainty, is the renormalization scale uncertainty, which reaches to around 10% at lower  $M_{jj}$ . It can also be observed that the PDF uncertainties are typically smaller compared to other theoretical uncertainty sources. This is mainly due to them being fully correlated between different  $V + \text{jets}$  processes, resulting in large cancellations in the ratios.

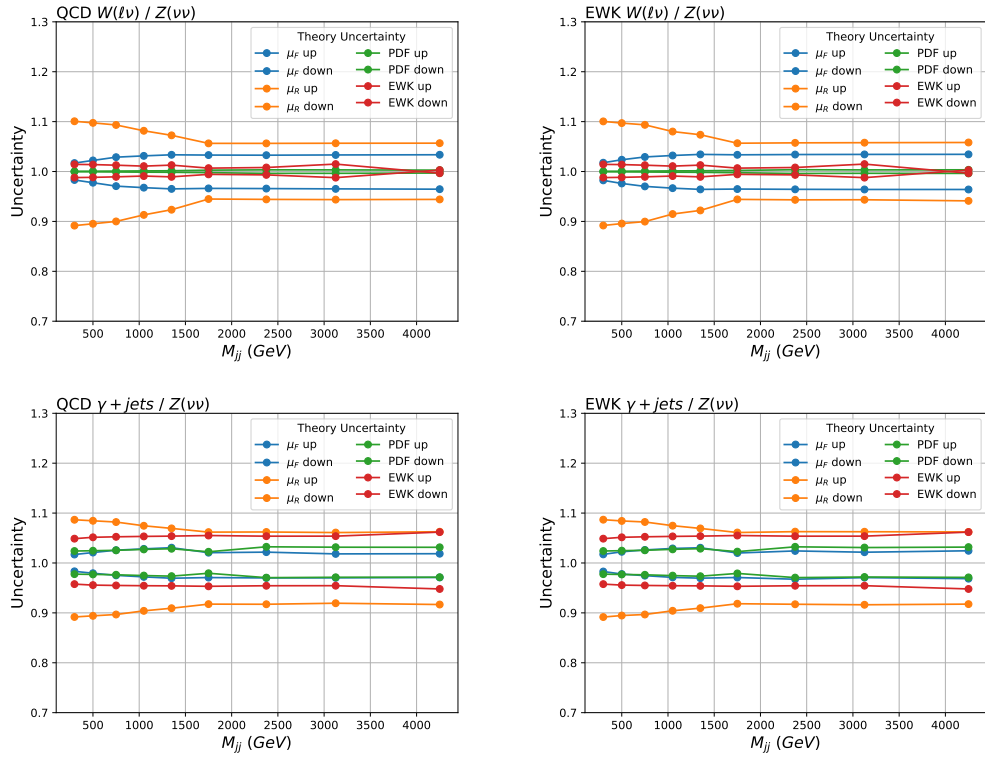


**Figure 3.60:** Theoretical uncertainties on  $W/Z$  (top) and  $\gamma/Z$  (bottom) transfer factors. Uncertainties are calculated as a function of  $M_{jj}$ . Uncertainties for QCD ratios are shown on the left column, while uncertainties for EWK ratios are shown on the right column.

## Experimental uncertainties

Experimental uncertainties include uncertainties on the lepton reconstruction and identification criteria, jet energy scale and resolution, pileup reweighting and prefire reweighting.

Uncertainties on veto weights are applied for electrons, muons, taus and b-jets. For the case of electrons and muons, the uncertainties are split into identification and isolation uncertainties, in accordance with the weight definitions for these objects, as defined in Sec. 3.2.3. These uncertainties are typically not correlated with the kinematics of the two VBF jets, and hence  $M_{jj}$ . Therefore, no significant shape as a function of  $M_{jj}$  is observed for these uncertainties, and flat uncertainties are applied. These uncertainties are summarized in Table. 3.11.

The uncertainty on the prefire reweighting, as explained in Sec. 3.2.6, is computed by varying the prefire weight within its uncertainties, and computing the impact on the  $M_{jj}$  distribution. The variations in the  $M_{jj}$  shape are computed from the VBF  $H \rightarrow \text{inv.}$  signal sample, and the resulting shapes are applied to all  $H \rightarrow \text{inv.}$  samples as a shape uncertainty. For minor backgrounds, a 3% flat uncertainty is applied instead, which is observed to be a good approximation of the uncertainty. Since prefire reweighting is done only on 2017 data, this uncertainty is only applied to 2017 data. The uncertainty on the prefiring weights as a function of  $M_{jj}$  is shown in Fig. 3.61. Similar to the prefire reweighting uncertainty, the uncertainty on pileup reweighting (explained in Sec. 3.2.2) is done by varying the pileup weight within its uncertainties, and computing the impact on the  $M_{jj}$  distribution per process. The uncertainty due to the pileup reweighting is found to be  $O(1\%)$ .

The uncertainty in the modeling of  $p_T^{\text{miss}}$  in simulation [46] is dominated by the uncertainty on the jet energy scale (JES) and resolution (JER). The effect is estimated by varying the  $p_T$  of VBF jets within their uncertainty, propagating the effect to

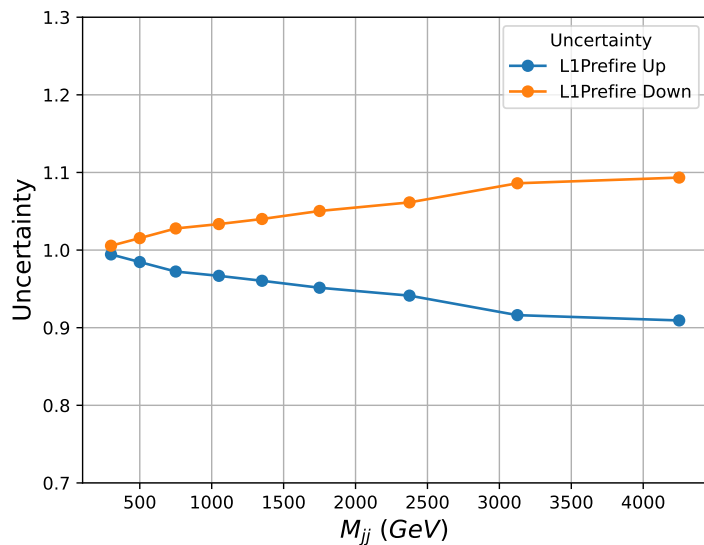


**Figure 3.61:** Uncertainty due to the L1 prefire reweighting as a function of  $M_{jj}$ . The uncertainty is computed from VBF  $H \rightarrow inv.$  signal sample by varying the prefiring weight within its uncertainty. This uncertainty is applied as a shape uncertainty to all  $H \rightarrow inv.$  signals considered in the analysis.

$p_T^{miss}$ , and then performing the full analysis selection based on the varied inputs. For JES uncertainties, this variation is done for 11 sub-sources, where each sub-source is defined in accordance with the correlation scheme defined by JetMET POG, which can be found in [47]. The uncertainties for JES and JER are applied both to the transfer factors, and to the individual processes such as signal processes and minor backgrounds.

In the transfer factors, the majority of the JES and JER uncertainties cancel, but residual non-cancellation is observed. The residual uncertainty remaining in the ratios is found to be within approximately 2%. For the transfer factors, a flat single-bin uncertainty is assigned for each JES and JER uncertainty source for each ratio. All the JES and JER uncertainties for the  $Z(\text{SR})/\text{Z}(\text{CR})$  ( $Z(\mu\mu) + \text{jets}$  and  $Z(ee) + \text{jets}$  channels combined for  $\text{Z}(\text{CR})$ ) ratio are shown in Fig. 3·62. The uncertainties for  $\text{Z}(\text{SR})/\gamma$  are shown in Fig 3·63.

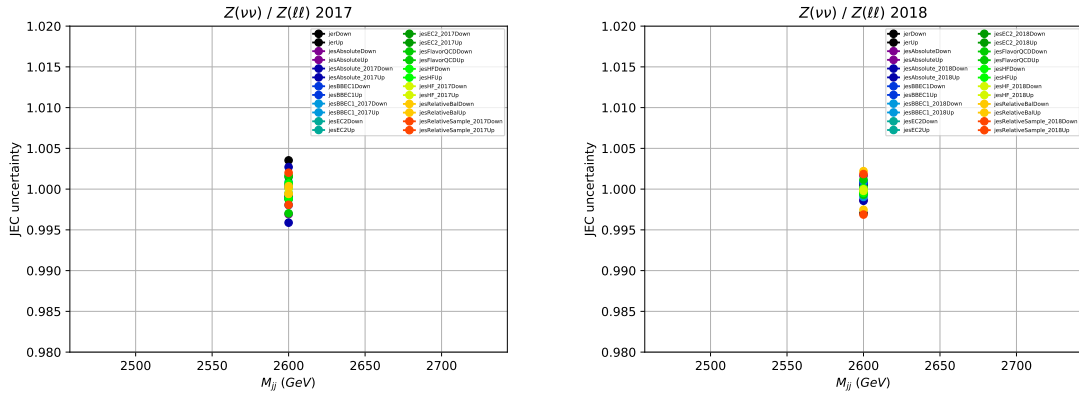


**Figure 3·62:** All single-bin JES/JER uncertainties on QCD  $Z(\text{SR})/\text{Z}(\text{CR})$  ratio for 2017 (left) and 2018 (right). The black dot shows the JER uncertainty, and the others show up and down variation from all 11 JES sub-sources. All jet energy scale and resolution uncertainties cancel to within less than 1%.

JES and JER uncertainties on minor backgrounds and signals are calculated in a very similar way as for the transfer factors. For these, the uncertainties are derived as

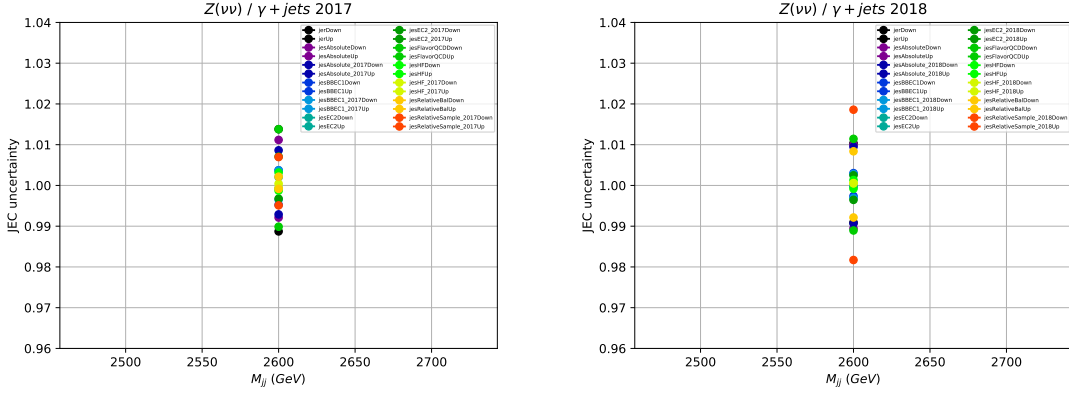


**Figure 3.63:** All single-bin JES/JER uncertainties on QCD Z(SR)/ $\gamma$  ratio for 2017 (left) and 2018 (right). The black dot shows the JER uncertainty, and the others show up and down variation from all 11 JES sub-sources. All jet energy scale and resolution uncertainties cancel within up to 2%.

a function of  $M_{jj}$  for each jet energy uncertainty source. The uncertainties for minor backgrounds (top, diboson) are derived using the strong  $Z(\nu\nu) + \text{jets}$  sample, due to the limited statistics from the minor backgrounds. The uncertainties for  $H \rightarrow \text{inv.}$  signal samples are derived from VBF  $H \rightarrow \text{inv.}$  sample. Most jet energy uncertainty sources are found to be on the order of  $\mathcal{O}(1\%)$ , while the uncertainty coming from the relative corrections are typically found to be the dominating ones, also displaying an increasing shape as a function of  $M_{jj}$ , reaching to  $\mathcal{O}(10\%)$  uncertainty levels at high  $M_{jj}$ .

The most dominating uncertainty source is the “Relative Sample” uncertainty, which is the jet  $\eta$ -dependent uncertainty due to different residual jet energy corrections obtained by measurement from different channels, such as dijet events,  $\gamma + \text{jet}$  events and  $Z + \text{jet}$  events. For these larger uncertainty sources, a second-degree polynomial is fit to smooth out the uncertainty shape. For smaller jet energy uncertainty sources, a line fit is performed instead. For most jet energy uncertainty sources, no significant shape is observed as a function of  $M_{jj}$ . The dominating jet energy uncer-

tainty source, “Relative Sample”, is plotted in Fig. 3.64 for QCD  $Z(\nu\nu) + \text{jets}$  and VBF  $H \rightarrow \text{inv.}$  samples.

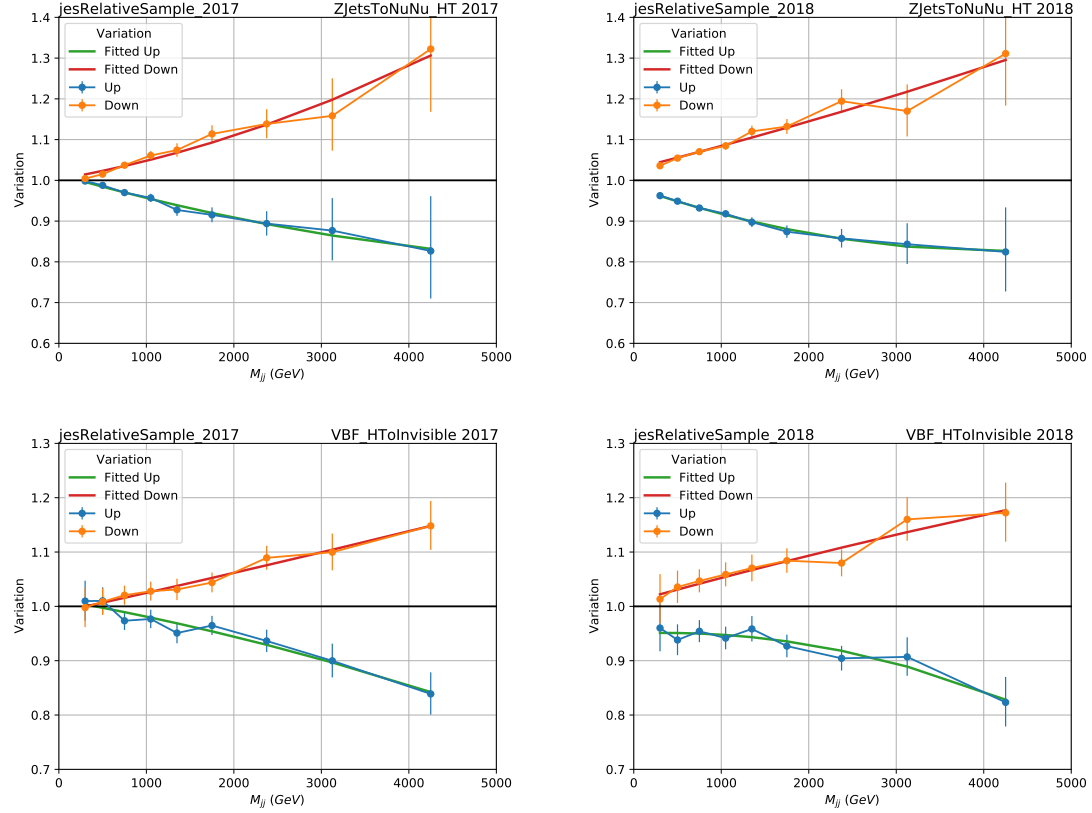


**Figure 3.64:** Relative sample JEC uncertainties calculated with strong  $Z(\nu\nu) + \text{jets}$  (top) and VBF  $H \rightarrow \text{inv.}$  signal (bottom). Left column shows the 2017 results, while the right column shows the 2018 results. The fitted uncertainties, shown in solid lines, are used as the final uncertainty shapes.

As discussed in Sec. 3.3.1, a 20% flat uncertainty is applied to the data-driven HF noise estimate, to take residual differences between data and expected background yields into account.

Uncertainties on trigger efficiency reweighting, as discussed in Sec. 3.2.1, are also applied in the analysis. For the electron, photon and  $p_T^{\text{miss}}$  trigger reweightings, flat uncertainties are applied on the transfer factors. The magnitudes of the flat

uncertainties are 1%, 1% and 2% respectively.

List of all theoretical and experimental uncertainties on transfer factors are shown in Tab. 3.11, together with the transfer factors they are applied on, and their magnitudes.

**Table 3.11:** Experimental and theoretical sources of systematic uncertainties in the  $V + \text{jets}$  transfer factors. The second column highlights on which ratio specifically a given source of uncertainty acts. The subscript SR (CR) refers to the process yield in the SR (corresponding CRs). The impact on  $M_{jj}$  is given in the 3rd column, either as a single value (if no dependence on  $M_{jj}$  is observed) or as a range of impact on low to high  $M_{jj}$  values.

Source of uncertainty	Ratios	Uncertainty vs. $M_{jj}$
Theoretical uncertainties		
Ren. scale $V + \text{jets}$ (VBF)	$Z_{\text{SR}}/W_{\text{SR}}$	5–10%
Ren. scale $V + \text{jets}$ (strong)	$Z_{\text{SR}}/W_{\text{SR}}$	5–10%
Fac. scale $V + \text{jets}$ (VBF)	$Z_{\text{SR}}/W_{\text{SR}}$	1.5%
Fac. scale $V + \text{jets}$ (strong)	$Z_{\text{SR}}/W_{\text{SR}}$	1.3%
PDF $V + \text{jets}$ (VBF)	$Z_{\text{SR}}/W_{\text{SR}}$	0%
PDF $V + \text{jets}$ (strong)	$Z_{\text{SR}}/W_{\text{SR}}$	0%
NLO EW corr. $V + \text{jets}$ (strong)	$Z_{\text{SR}}/W_{\text{SR}}$	0.5%
Ren. scale $\gamma + \text{jets}$ (VBF)	$Z_{\text{SR}}/\gamma_{\text{CR}}$	6–10%
Ren. scale $\gamma + \text{jets}$ (strong)	$Z_{\text{SR}}/\gamma_{\text{CR}}$	6–10%
Fac. scale $\gamma + \text{jets}$ (VBF)	$Z_{\text{SR}}/\gamma_{\text{CR}}$	2.5%
Fac. scale $\gamma + \text{jets}$ (strong)	$Z_{\text{SR}}/\gamma_{\text{CR}}$	2.5%
PDF $\gamma + \text{jets}$ (VBF)	$Z_{\text{SR}}/\gamma_{\text{CR}}$	2.5%
PDF $\gamma + \text{jets}$ (strong)	$Z_{\text{SR}}/\gamma_{\text{CR}}$	2.5%
NLO EW corr. $\gamma + \text{jets}$	$Z_{\text{SR}}/\gamma_{\text{CR}}$	3%
Experimental uncertainties		
Electron reco. eff.	$Z_{\text{CR}}/Z_{\text{SR}}, W_{\text{CR}}/W_{\text{SR}}$	$\approx 0.5\%$ (per lepton)
Electron id. eff.	$Z_{\text{CR}}/Z_{\text{SR}}, W_{\text{CR}}/W_{\text{SR}}$	$\approx 1\%$ (per lepton)
Muon id. eff.	$Z_{\text{CR}}/Z_{\text{SR}}, W_{\text{CR}}/W_{\text{SR}}$	$\approx 0.5\%$ (per lepton)
Muon iso. eff.	$Z_{\text{CR}}/Z_{\text{SR}}, W_{\text{CR}}/W_{\text{SR}}$	$\approx 0.1\%$ (per lepton)
Photon id. eff.	$Z_{\text{SR}}/\gamma$	5%
Electron veto (reco)	$Z_{\text{SR}}/W_{\text{SR}}, W_{\text{CR}}/W_{\text{SR}}$	$\approx 1.5$ (1)% for VBF (strong)
Electron veto (id)	$Z_{\text{SR}}/W_{\text{SR}}, W_{\text{CR}}/W_{\text{SR}}$	$\approx 2.5$ (2)% for VBF (strong)
Muon veto	$Z_{\text{SR}}/W_{\text{SR}}, W_{\text{CR}}/W_{\text{SR}}$	$\approx 0.5\%$
$\tau_h$ veto	$Z_{\text{SR}}/W_{\text{SR}}, W_{\text{CR}}/W_{\text{SR}}$	$\approx 1\%$
Electron trigger	$Z_{\text{CR}}/Z_{\text{SR}}, W_{\text{CR}}/W_{\text{SR}}$	$\approx 1\%$
$p_T^{\text{miss}}$ trigger	$Z_{\text{CR}}/Z_{\text{SR}}, W_{\text{CR}}/W_{\text{SR}}$	$\approx 2\%$
Photon trigger	$Z_{\text{SR}}/\gamma$	1%
JES	$Z_{\text{SR}}/W_{\text{SR}}$	1–2%
	$W_{\text{CR}}/W_{\text{SR}}$	1.0–1.5%
	$Z_{\text{CR}}/Z_{\nu\nu}$	1%
	$Z_{\text{SR}}/\gamma$	3%
JER	$Z_{\text{SR}}/W_{\text{SR}}$	1.0–2.5%
	$W_{\text{CR}}/W_{\text{SR}}$	1.0–1.5%
	$Z_{\text{CR}}/Z_{\text{SR}}$	1%
	$Z_{\text{SR}}/\gamma$	1–4%

## Chapter 4

# Results

### 4.1 Combined likelihood fit

To get the best-fit value of the signal strength  $\mu = (\sigma_H/\sigma_H^{\text{SM}})\mathcal{B}(H \rightarrow \text{inv})$ , a maximum-likelihood fit is performed across all different signal and control regions in the analysis, using the likelihood function given in Eq. 3.13. In this fit, data from 2017 and 2018 are combined. Theoretical uncertainties are treated as correlated between different years, while some experimental uncertainties, such as the jet energy scale uncertainties, are partially correlated between different years, depending on the uncertainty source. The partial correlation scheme is in accordance with the recommendations from the relevant POGs. The theoretical and experimental uncertainties are discussed in depth in Sec. 3.5.2.

Figs. 4·1, 4·2, 4·3 show the results of the 2017+2018 combined fit in all control regions and the signal region of the analysis. Data observed in each region is compared to the background predictions from simulation and data-driven estimates (pre-fit) and background predictions after the fit (post-fit). Overall, it can be observed that post-fit background estimates are in very good agreement with the observed data, and no significant pulls ( $\text{data} - \text{prediction}/\text{uncertainty} > 2\sigma$ ) are observed when fitting the data.

For the signal region plots in Fig. 4·1 (top row), two data-driven multijet background estimates have been shown, which represent the events where  $p_T^{\text{miss}}$  arises from mismeasured jets. The first multijet estimate, labeled as “HF Estimate”, represents

the noise estimation related to events with forward jets in Forward HCAL (HF) detector, where the mismeasured jet is balanced with  $p_T^{miss}$ , therefore  $\Delta\phi(\vec{p}_T^{\text{jet}}, \vec{p}_T^{miss})$  is large. The derivation of this estimate is explained in Sec. 3.3.1.

The second data-driven estimate is labeled as “QCD”, which is an independent estimate of events where the mismeasured jet is aligned with  $p_T^{miss}$ , therefore  $\Delta\phi(\vec{p}_T^{\text{jet}}, \vec{p}_T^{miss})$  is small. This background is estimated from another control region, where the  $\Delta\phi(\vec{p}_T^{\text{jet}}, \vec{p}_T^{miss}) > 0.5$  selection (listed in Table. 3.10) is inverted, as explained in [7].

The observed event yields for each  $M_{jj}$  bin, and the corresponding expected event yields from each background process are summarized in Tables 4.1 and 4.2.

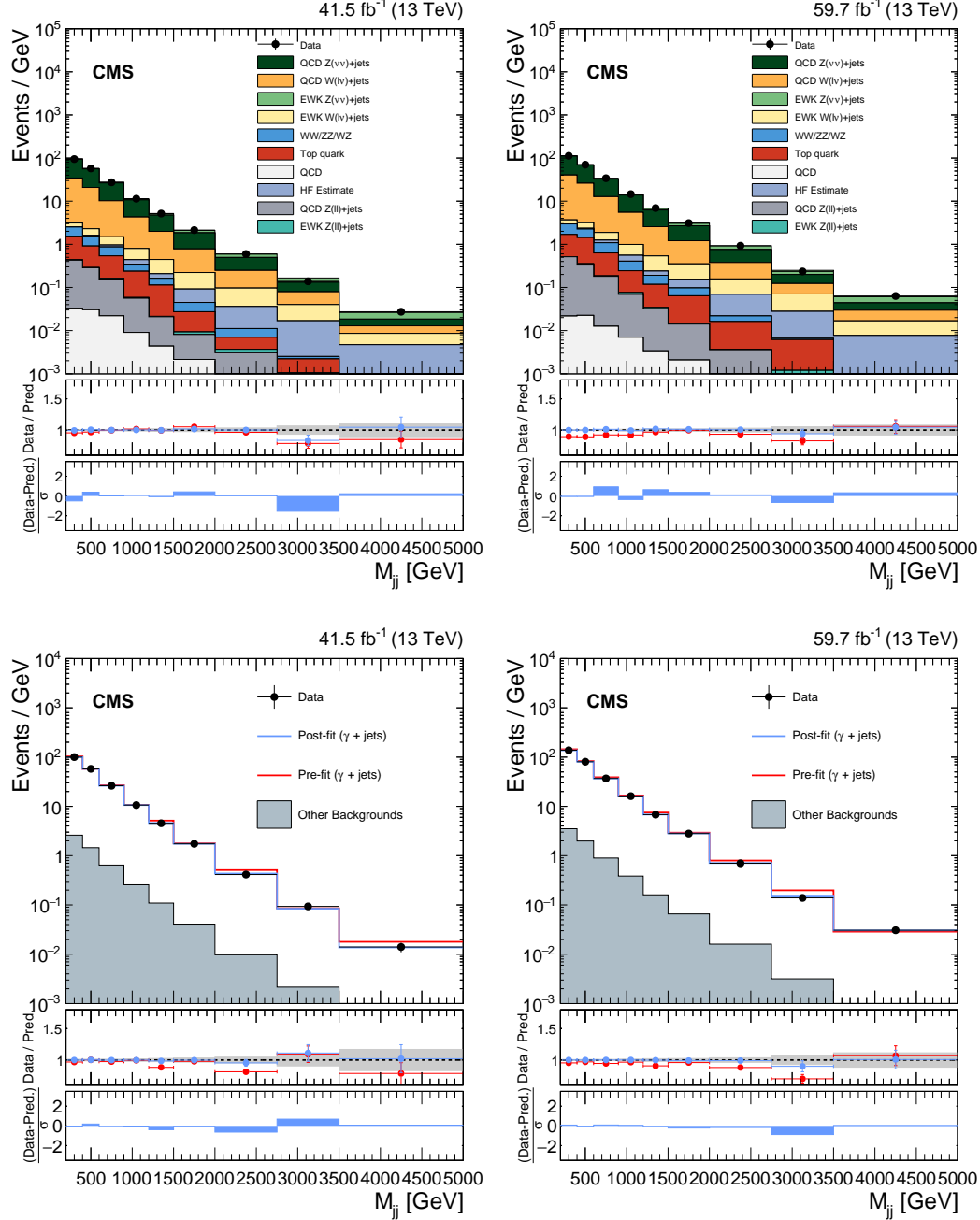


**Figure 4.1:** Comparison between data and background estimation in VBF SR (top) and  $\gamma + \text{jets}$  CR (bottom), before and after the simultaneous fit. The fit includes the data in all CRs and the signal region. The resulting distributions are shown separately for 2017 (left) and 2018 (right). In the ratio pads, ratios of data and background estimation are shown before (red) and after (blue) the fit. The gray band indicates the post-fit uncertainty. Finally, the distribution of the difference between data and post-fit background prediction relative to the quadrature sum of the uncertainties in the prediction and in data is shown in the lowest panel.

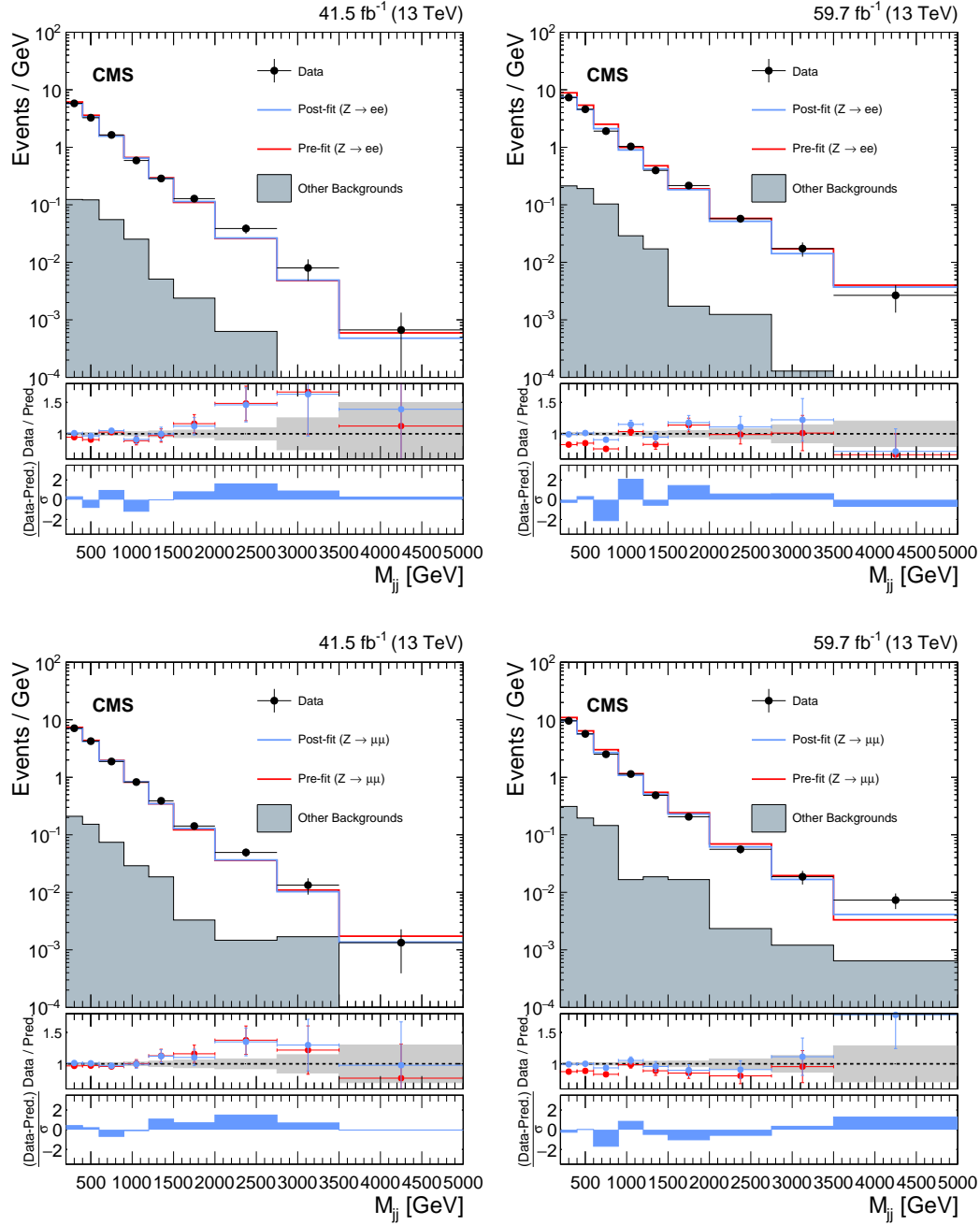


**Figure 4·2:** Same as Fig. 4·1 but with dilepton CRs. The other backgrounds include top quark and diboson processes.

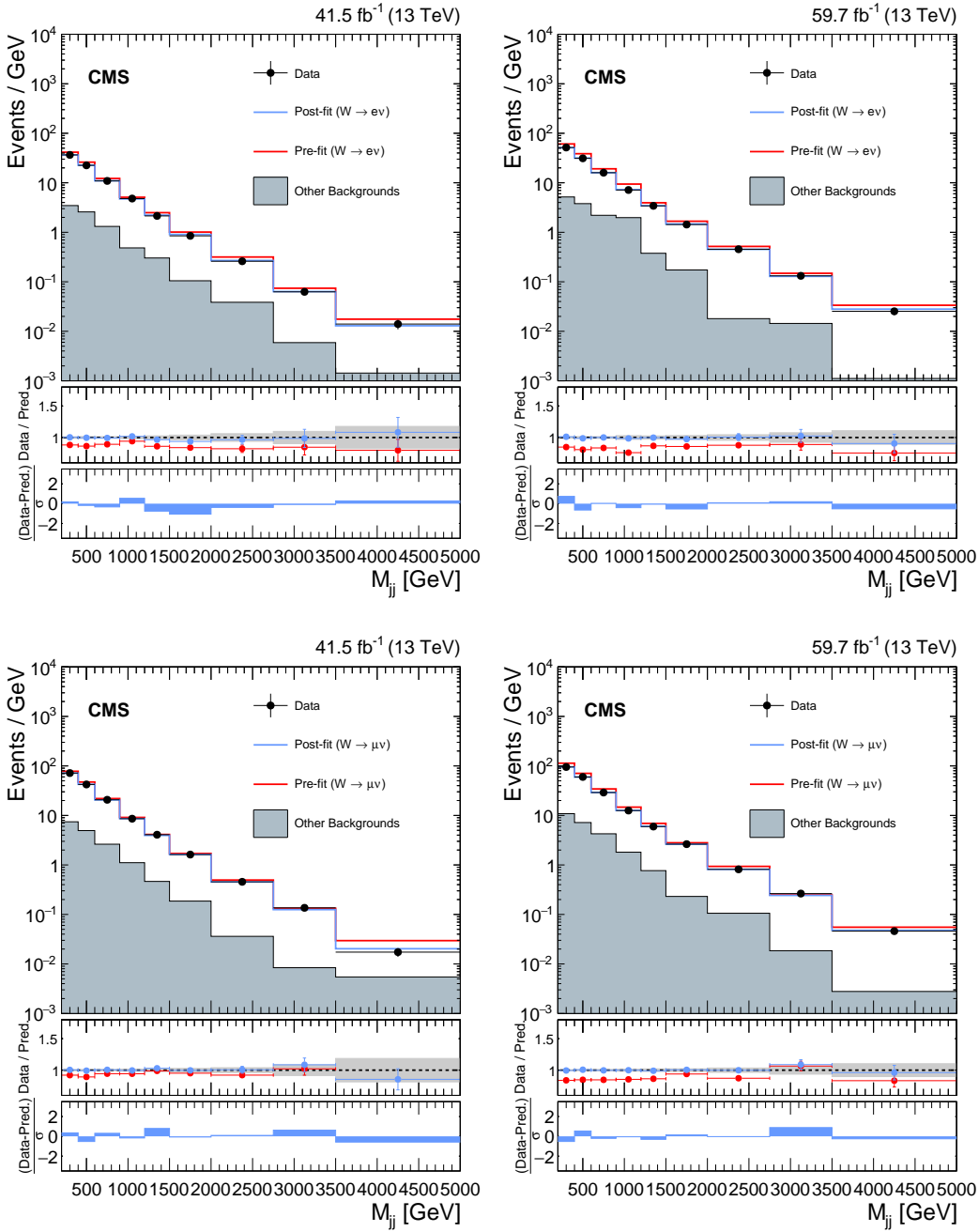


**Figure 4.3:** Same as Fig. 4.1 but with single lepton CRs. The other backgrounds include top quark and diboson processes.

**Table 4.1:** Expected event yields in each  $M_{jj}$  bin for the different background processes in the VBF signal region, with the 2017 samples. The background yields and the corresponding uncertainties are obtained after performing a combined fit across all of the CRs and SR. The expected signal contributions for a Higgs boson, produced in the non-VBF and VBF modes, decaying to invisible particles with a branching fraction of  $\mathcal{B}(H \rightarrow \text{inv.}) = 1$ , and the observed event yields are also reported.

$M_{jj}$ bin range (GeV)	200-400	400-600	600-900	900-1200	1200-1500	1500-2000	2000-2750	2750-3500	>3500
$Z(\nu\nu) + \text{jets (strong)}$	11957.1 $\pm$ 55.5	7022.4 $\pm$ 42.2	4855.8 $\pm$ 34.6	1914.1 $\pm$ 17.6	826.8 $\pm$ 11.4	531.3 $\pm$ 8.5	183.5 $\pm$ 4.7	39.6 $\pm$ 4.1	8.3 $\pm$ 0.9
$Z(\nu\nu) + \text{jets (VBF)}$	202.5 $\pm$ 4.1	222.2 $\pm$ 4.1	272.3 $\pm$ 4.3	197.6 $\pm$ 3.8	127.2 $\pm$ 3.2	126.4 $\pm$ 3.6	74.0 $\pm$ 2.9	25.3 $\pm$ 2.9	11.5 $\pm$ 1.4
$W(\ell\nu) + \text{jets (strong)}$	6247.9 $\pm$ 57.1	3727.1 $\pm$ 36.6	2624.7 $\pm$ 31.6	1052.3 $\pm$ 15.7	450.0 $\pm$ 11.7	285.5 $\pm$ 7.1	116.5 $\pm$ 4.9	27.1 $\pm$ 2.7	5.1 $\pm$ 1.0
$W(\ell\nu) + \text{jets (VBF)}$	122.6 $\pm$ 7.2	137.9 $\pm$ 7.5	161.9 $\pm$ 8.1	109.4 $\pm$ 5.3	72.3 $\pm$ 3.5	65.8 $\pm$ 3.1	45.7 $\pm$ 2.9	17.5 $\pm$ 1.8	5.9 $\pm$ 0.8
$t\bar{t} + \text{single-top}$	237.6 $\pm$ 16.0	135.8 $\pm$ 9.1	124.0 $\pm$ 8.0	60.1 $\pm$ 3.7	30.7 $\pm$ 2.0	9.7 $\pm$ 0.8	2.7 $\pm$ 0.3	0.9 $\pm$ 0.2	0.4 $\pm$ 0.1
Diboson	201.0 $\pm$ 24.8	132.9 $\pm$ 16.0	101.7 $\pm$ 12.2	34.4 $\pm$ 4.2	15.8 $\pm$ 1.9	9.2 $\pm$ 1.2	3.3 $\pm$ 0.5	0.3 $\pm$ 0.0	0.0 $\pm$ 0.0
$Z/\gamma^*(\ell^+\ell^-) + \text{jets}$	86.6 $\pm$ 3.3	54.9 $\pm$ 2.1	44.7 $\pm$ 1.6	15.7 $\pm$ 0.6	6.0 $\pm$ 0.4	4.3 $\pm$ 0.3	2.6 $\pm$ 0.2	0.5 $\pm$ 0.1	0.1 $\pm$ 0.0
Multijet	6.6 $\pm$ 1.5	6.1 $\pm$ 1.4	6.6 $\pm$ 1.5	2.7 $\pm$ 0.6	1.3 $\pm$ 0.3	1.1 $\pm$ 0.2	0.4 $\pm$ 0.1	0.2 $\pm$ 0.0	0.1 $\pm$ 0.0
HF Noise	0.8 $\pm$ 0.1	16.6 $\pm$ 2.1	28.2 $\pm$ 3.6	25.1 $\pm$ 3.2	9.3 $\pm$ 1.2	18.4 $\pm$ 2.3	18.2 $\pm$ 2.3	10.7 $\pm$ 1.4	7.4 $\pm$ 0.9
$ggH(\rightarrow \text{inv.})$	570.5	411.5	338.0	162.8	82.5	61.8	30.4	8.1	3.6
$qqH(\rightarrow \text{inv.})$	56.2	125.7	245.8	244.0	191.2	217.9	156.1	62.6	45.6
$WH(\rightarrow \text{inv.})$	29.7	17.0	11.5	3.9	1.9	0.8	0.5	0.1	0.0
$qqZH(\rightarrow \text{inv.})$	14.0	6.8	4.0	1.2	0.7	0.4	0.4	0.0	0.0
$ggZH(\rightarrow \text{inv.})$	14.0	8.6	5.5	2.3	1.0	0.6	0.3	0.1	0.0
$ttH(\rightarrow \text{inv.})$	3.6	2.6	1.8	0.7	0.3	0.2	0.1	0.0	0.0
Total bkg.	19062.6 $\pm$ 85.4	11455.8 $\pm$ 59.5	8220.0 $\pm$ 50.1	3411.5 $\pm$ 25.4	1539.4 $\pm$ 17.3	1051.6 $\pm$ 12.4	446.9 $\pm$ 8.3	122.0 $\pm$ 6.2	38.9 $\pm$ 2.3
Observed	18945	11500	8218	3419	1549	1068	447	104	41

**Table 4.2:** Expected event yields in each  $M_{jj}$  bin for the different background processes in the VBF signal region, with the 2018 samples. The background yields and the corresponding uncertainties are obtained after performing a combined fit across all of the CRs and SR. The expected signal contributions for a Higgs boson, produced in the non-VBF and VBF modes, decaying to invisible particles with a branching fraction of  $\mathcal{B}(H \rightarrow \text{inv.}) = 1$ , and the observed event yields are also reported.

$M_{jj}$ bin range (GeV)	200-400	400-600	600-900	900-1200	1200-1500	1500-2000	2000-2750	2750-3500	$>3500$
$Z(\nu\nu) + \text{jets (strong)}$	14150.5 ± 61.3	8498.6 ± 45.5	5891.5 ± 34.4	2490.3 ± 18.1	1096.6 ± 12.2	730.4 ± 9.4	278.9 ± 5.8	55.9 ± 2.3	20.5 ± 1.2
$Z(\nu\nu) + \text{jets (VBF)}$	228.8 ± 4.5	276.0 ± 5.1	348.3 ± 5.6	254.4 ± 4.9	167.7 ± 4.3	191.5 ± 4.8	123.3 ± 4.4	36.8 ± 2.1	24.3 ± 1.9
$W(\ell\nu) + \text{jets (strong)}$	7323.4 ± 51.4	4566.3 ± 38.3	3243.7 ± 29.5	1357.2 ± 17.3	603.5 ± 11.1	418.9 ± 8.3	160.2 ± 5.8	38.3 ± 3.0	18.4 ± 2.2
$W(\ell\nu) + \text{jets (VBF)}$	145.4 ± 7.7	163.6 ± 8.4	191.7 ± 9.7	133.5 ± 6.6	90.7 ± 4.7	98.1 ± 5.2	66.2 ± 3.7	31.9 ± 2.6	13.3 ± 1.4
$t\bar{t} + \text{single-top}$	261.3 ± 13.9	234.8 ± 12.6	151.5 ± 8.7	55.2 ± 3.5	28.9 ± 1.9	29.0 ± 2.0	12.2 ± 1.2	4.4 ± 0.4	1.4 ± 0.2
Diboson	264.0 ± 31.4	172.2 ± 20.7	144.5 ± 17.5	51.0 ± 6.2	23.6 ± 3.0	18.2 ± 2.4	4.6 ± 0.6	0.4 ± 0.1	0.0 ± 0.0
$Z/\gamma^*(\ell^+\ell^-) + \text{jets}$	105.7 ± 2.8	71.4 ± 2.0	57.3 ± 1.9	22.6 ± 0.8	10.1 ± 0.4	7.6 ± 0.5	2.3 ± 0.2	0.9 ± 0.1	0.2 ± 0.0
Multijet	4.4 ± 1.3	4.5 ± 1.3	3.8 ± 1.1	2.1 ± 0.6	1.0 ± 0.3	1.0 ± 0.3	0.5 ± 0.2	0.2 ± 0.0	0.1 ± 0.0
HF Noise	0.0 ± 0.0	18.5 ± 2.2	54.4 ± 6.4	45.2 ± 5.3	18.8 ± 2.2	38.0 ± 4.4	44.0 ± 5.1	19.8 ± 2.3	13.4 ± 1.6
$ggH(\rightarrow \text{inv.})$	719.3	534.7	461.5	232.2	119.0	95.1	52.2	15.7	7.2
$qqH(\rightarrow \text{inv.})$	74.3	171.3	340.3	327.8	269.2	321.6	271.1	115.3	72.4
$WH(\rightarrow \text{inv.})$	39.6	22.9	12.6	5.2	1.9	1.1	0.3	0.2	0.1
$q9ZH(\rightarrow \text{inv.})$	18.4	8.5	3.9	1.9	0.4	0.6	0.2	0.0	0.0
$ggZH(\rightarrow \text{inv.})$	17.2	11.2	7.6	3.1	1.2	1.0	0.4	0.1	0.0
$ttH(\rightarrow \text{inv.})$	4.7	3.4	2.6	1.1	0.5	0.4	0.1	0.0	0.0
Total bkg.	22483.4 ± 87.5	14005.9 ± 65.1	10086.6 ± 51.1	4411.4 ± 27.8	2040.8 ± 18.1	1532.7 ± 15.4	692.3 ± 11.4	188.6 ± 5.6	91.7 ± 3.7
Observed	22505	14036	10220	4374	2080	1555	695	176	95

## 4.2 Combinations

This section describes the combination of the results presented in Sec. 4.1 with different analysis categories. Sec. 4.2.1 describes the combination with an orthogonal VBF analysis category called VBF-triggered region (VTR). Sec. 4.2.2 describes the combination with the VBF  $H \rightarrow inv.$  analysis by CMS using 2016 dataset [48].

### 4.2.1 Combination with VTR category

As discussed in Sec. 3.4.1, an orthogonal set of selection categories (compared to selection categories listed in Sec. 3.4) are included in the analysis as well. Events in this category are collected using a different set of VBF triggers (instead of the  $p_{T,no-\mu}^{miss}$  triggers described in Sec. 3.2.1), and target events at a lower  $p_T^{miss}$  range of [160, 250] GeV, hence making the event category orthogonal to what has been discussed so far, with  $p_T^{miss} > 250$  GeV. This category is called the VBF-triggered region (VTR). The VTR category comprises of the signal region,  $Z$  and  $W$  control regions, but it does not have the  $\gamma + jets$  control region due to the lower recoil range it targets (note that  $p_T^\gamma > 200$  GeV is required for the photon triggers in use, as explained in Sec. 3.2.1).

When combining the VTR category with this analysis to do a combined fit to data, likelihood terms from each region in the VTR category are added to the likelihood function shown in Eq. 3.13. The details of VTR event selection, results and the combination are discussed in [7].

### 4.2.2 Combination with 2016 dataset

The results from this analysis are also statistically combined with the results from the CMS experiment with 2016 dataset [48]. Data from 2016 analysis is considered as different event categories, similar to the way which is done when combining 2017 and 2018 datasets.

During the combination, theoretical uncertainties are treated as correlated between different years, while most experimental uncertainties are treated as uncorrelated between 2016 and 2017+2018 categories. The integrated luminosity has been updated for the 2016 dataset to  $36.3\text{ fb}^{-1}$  to reflect the latest improvements [49]. In addition, to be consistent with the treatment of the VBF  $H \rightarrow \text{inv.}$  signal with 2017 and 2018 analyses, the Higgs boson  $p_T$  dependent NLO EWK corrections (described in Sec. 3.2.7) are also applied to the 2016 signal shape.

Fig. 4·4 shows the fit results in the VBF signal region when data from all three years (2016-2018) are combined. Total background estimated from the fit to the data (as described in Sec. 3.5.1) is shown (S+B fit), together with a background estimate from a fit assuming  $\mathcal{B}(H \rightarrow \text{inv}) = 0$  (B-only fit) are shown. In the S+B fit, the best-fit signal strength is computed to be  $\mathcal{B}(H \rightarrow \text{inv}) = 0.086^{+0.054}_{-0.052}$ . Expected event yields from different Higgs production modes are also plotted in Fig. 4·4, each scaled to the best-fit signal strength value of  $\mathcal{B}(H \rightarrow \text{inv}) = 0.086$ .

The impact of each uncertainty source to the total uncertainty on  $\mathcal{B}(H \rightarrow \text{inv})$  is shown in Tab. 4.3. It can be observed that the largest contributions to the uncertainty on determining  $\mathcal{B}(H \rightarrow \text{inv})$  come from the theory uncertainties on  $V+\text{jets}$  transfer factors (e.g. uncertainties on  $\mu_R$ ), together with the statistical uncertainties on the collected data and simulated events.

From Fig. 4·4, it can be observed that no significant excess of data is observed compared to the Standard Model background. Therefore, the results from this analysis are interpreted as an upper bound on  $\mu = (\sigma_H/\sigma_H^{\text{SM}})\mathcal{B}(H \rightarrow \text{inv})$ , the methodology and resulting upper bounds are described in the next section.

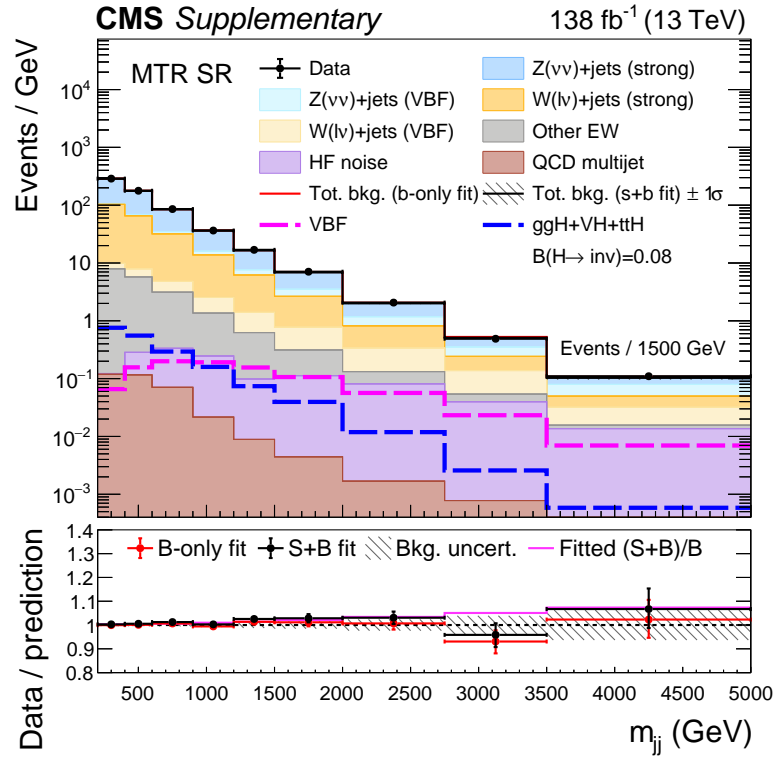


**Figure 4.4:** The observed  $M_{jj}$  distribution in the VBF signal region compared to the postfit backgrounds, with the 2016, 2017, and 2018 datasets. The signal processes are scaled by the fitted value of  $\mathcal{B}(H \rightarrow \text{inv})$ , shown in the legend. The background contributions are estimated from the fit to the data described in Sec. 3.5.1 (S+B fit). Total background estimated from a fit assuming  $\mathcal{B}(H \rightarrow \text{inv}) = 0$  (B-only fit) is also shown. The last bin of each distribution integrates events above the bin threshold divided by the bin width. Figure taken from [7].

**Table 4.3:** Uncertainty breakdown in  $\mathcal{B}(H \rightarrow \text{inv})$ . The sources of uncertainty are separated into different groups. Observed and expected results are quoted for the full combination of 2016, 2017, and 2018 data. The expected results are obtained using an Asimov dataset [2] with  $\mathcal{B}(H \rightarrow \text{inv}) = 0$ .

Group of systematic uncertainties	Observed impact on $\mathcal{B}(H \rightarrow \text{inv})$	Expected impact on $\mathcal{B}(H \rightarrow \text{inv})$
Theory	+0.026 -0.025	$\pm 0.024$
MC event count	+0.024 -0.023	+0.023 -0.024
Triggers	+0.021 -0.022	$\pm 0.021$
Leptons/photons/b	+0.012 -0.011	+0.010 -0.011
QCD multijet mismodelling	$\pm 0.013$	$\pm 0.014$
Jet calibration	+0.010 -0.007	$\pm 0.007$
Int. luminosity/pileup	$\pm 0.005$	+0.004 -0.005
Other systematic uncertainties	+0.013 -0.010	$\pm 0.010$
Stat.	$\pm 0.029$	$\pm 0.030$

## 4.3 Interpretations

### 4.3.1 Invisible branching fraction of SM Higgs boson

Since no statistically significant excess is observed in data compared to estimated SM background, the results are interpreted as upper bounds to  $\mu = (\sigma_H/\sigma_H^{\text{SM}})\mathcal{B}(H \rightarrow \text{inv})$ . Assuming a Standard Model (SM) Higgs boson,  $\mu$  can be interpreted as  $\mathcal{B}(H \rightarrow \text{inv})$ . Observed and expected 95% CL upper limits are computed using an asymptotic approximation of the  $CL_s$  method, which is detailed in Refs. [50, 51].

Observed and expected upper limits on  $\mu = (\sigma_H/\sigma_H^{\text{SM}})\mathcal{B}(H \rightarrow \text{inv})$  at 95% CL are presented in Fig. 4.5. A more detailed breakdown of upper limits coming from different years and categories is also provided in Tab. 3.11.

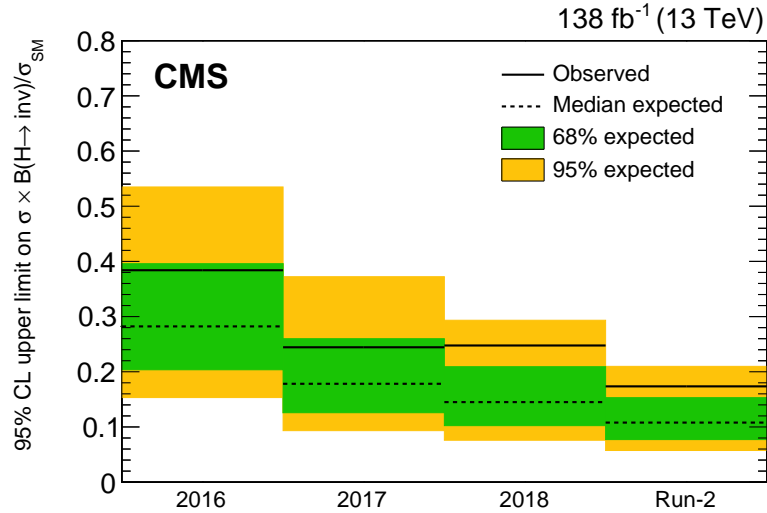


**Figure 4.5:** Observed and expected 95% CL upper limits on  $(\sigma_H/\sigma_H^{\text{SM}})\mathcal{B}(H \rightarrow \text{inv})$  for all three data-taking years, together with the  $1\sigma$  (green) and  $2\sigma$  (yellow) uncertainty bands on the expected upper limits. The combination of 2016–2018 is also shown. These results assume a SM Higgs boson with a mass of 125.38 GeV. Figure taken from [7].

**Table 4.4:** The 95% CL upper limits on  $(\sigma_H/\sigma_H^{\text{SM}})\mathcal{B}(H \rightarrow \text{inv})$ , assuming an SM Higgs boson with a mass of 125.38 GeV. The observed and median expected results are shown, along with the 68% and 95% interquartile ranges for each category and for the combinations.

Category	Observed	Median expected	65% expected	95% expected
2012-2016	0.33	0.21	[0.15,0.29]	[0.11,0.39]
VTR 2017	0.57	0.45	[0.32,0.66]	[0.24,0.94]
VTR 2018	0.44	0.34	[0.24,0.49]	[0.18,0.69]
VTR 2017 2018	0.40	0.28	[0.20,0.40]	[0.15,0.56]
MTR 2017	0.25	0.19	[0.14,0.28]	[0.10,0.40]
MTR 2018	0.24	0.15	[0.11,0.22]	[0.08,0.31]
MTR 2017 2018	0.17	0.13	[0.09,0.18]	[0.07,0.25]
all 2017	0.24	0.18	[0.13,0.26]	[0.09,0.37]
all 2018	0.25	0.15	[0.10,0.21]	[0.08,0.29]
all 2017 2018	0.18	0.12	[0.08,0.17]	[0.06,0.23]
Run2	0.18	0.10	[0.07,0.14]	[0.05,0.20]

### 4.3.2 Upper bound on DM-nucleon interactions

The upper limit on  $\mathcal{B}(H \rightarrow \text{inv})$ , obtained from combining the data taken between 2012 and 2018, is interpreted in the context of Higgs-portal models of DM interactions, in which a stable DM particle couples to the SM Higgs boson. The interaction between a DM particle and an atomic nucleus may be mediated by the exchange of a Higgs boson, producing nuclear recoil signatures, such as those investigated by direct-detection experiments.

If the mass of the DM particle,  $m_{DM}$ , is smaller than half of the mass of the Higgs boson, the Higgs boson invisible width ( $\Gamma_{\text{inv}}$ ) can be translated, within an effective field theory approach, into a spin-independent DM-nucleon elastic scattering cross section, as outlined in Ref. [52]. This translation is performed assuming that the DM candidate is either a scalar or a Majorana fermion, and both the central value

and the uncertainty of the dimensionless nuclear form-factor  $f_N$  are taken from the recommendations of Ref. [53]. The conversion from  $\mathcal{B}(H \rightarrow \text{inv})$  to  $\Gamma_{\text{inv}}$  uses the relation  $\mathcal{B}(H \rightarrow \text{inv}) = \Gamma_{\text{inv}} / (\Gamma_{\text{SM}} + \Gamma_{\text{inv}})$ , where  $\Gamma_{\text{SM}}$  is set to 4.07 MeV [54]. The assumption of a vector DM candidate is not provided in the context of this analysis, since it requires an extended dark Higgs sector, which may lead to modifications of kinematic distributions assumed for the invisible Higgs boson signal in this analysis.

Fig. 4.6 shows the 90% CL upper limits on the spin-independent DM-nucleon scattering cross section as a function of  $m_{\text{DM}}$ , for both the scalar and the fermion DM scenarios. These limits are computed at 90% CL so that they can be compared with those from direct detection experiments such as Xenon1T [8], Cresst-II [9], CDMSlite [10], LUX [11], Panda-X 4T [12], and DarkSide-50 [13], which provide the strongest constraints in the  $m_{\text{DM}}$  range probed by this search. The collider-based results complement the direct-detection experiments in the range  $m_{\text{DM}}$  smaller than 12 (6) GeV, assuming a fermion (scalar) DM candidate.

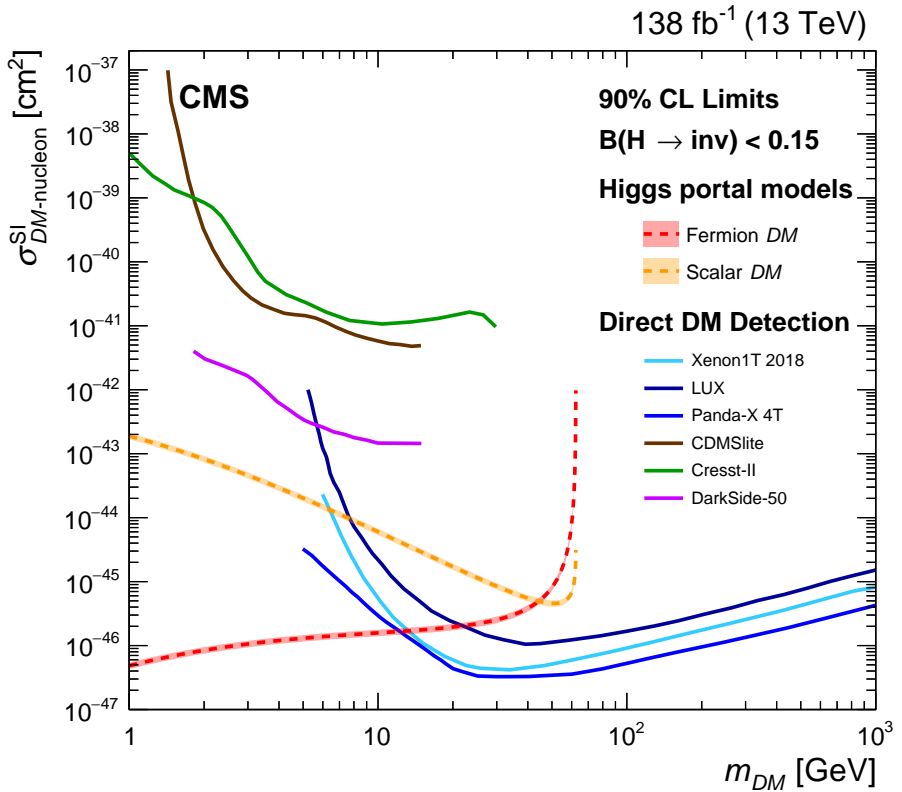


**Figure 4.6:** The 90% CL upper limits on the spin-independent DM-nucleon scattering cross section in Higgs-portal models, assuming a scalar (dashed orange) or fermion (dashed red) DM candidate. Limits are computed as functions of  $m_{DM}$  and are compared to those from the Xenon1T [8], Cresst-II [9], CDMSlite [10], LUX [11], Panda-X 4T [12], and DarkSide-50 [13] experiments, which are shown as solid lines. Figure taken from [7].

## **Chapter 5**

## **Outlook**

# Bibliography

- [1] CMS JME POG. <https://twiki.cern.ch/twiki/bin/view/CMS/MissingETOptionalFiltersRun2>.
- [2] Glen Cowan, Kyle Cranmer, Eilam Gross, and Ofer Vitells. Asymptotic formulae for likelihood-based tests of new physics. *Eur. Phys. J. C*, 71:1554, 2011.
- [3] CERN. Cern accelerator complex. <https://home.cern/science/accelerators/accelerator-complex>.
- [4] CMS Collaboration. Cms detector design. <https://cms.cern/news/cms-detector-design>.
- [5] CMS Collaboration. The CMS phase-1 pixel detector upgrade. *Journal of Instrumentation*, 16(P02027), 2021.
- [6] CMS Collaboration. The CMS experiment at the CERN LHC. *Journal of Instrumentation*, 3(S08004), 2008.
- [7] CMS Collaboration. Search for invisible decays of the Higgs boson produced via vector boson fusion in proton-proton collisions at  $\sqrt{s} = 13$  TeV. *Phys. Rev. D*, 105:092007, May 2022.
- [8] E. Aprile et al. Dark matter search results from a one ton-year exposure of XENON1T. *Phys. Rev. Lett.*, 121:111302, 2018.
- [9] G. Angloher et al. Results on light dark matter particles with a low-threshold CRESST-II detector. *Eur. Phys. J. C*, 76:25, 2016.
- [10] R. Agnese et al. New results from the search for low-mass weakly interacting massive particles with the CDMS low ionization threshold experiment. *Phys. Rev. Lett.*, 116:071301, 2016.
- [11] D. S. Akerib et al. Results from a search for dark matter in the complete LUX exposure. *Phys. Rev. Lett.*, 118:021303, 2017.
- [12] Yue Meng et al. Dark Matter Search Results from the PandaX-4T Commissioning Run. 7 2021.
- [13] P. Agnes et al. Low-mass dark matter search with the DarkSide-50 Experiment. *Phys. Rev. Lett.*, 121:081307, 2018.

- [14] CMS Collaboration. CMS luminosity measurement for the 2018 data-taking period at  $\sqrt{s} = 13 \text{ TeV}$ . <https://cds.cern.ch/record/2676164>, 2019.
- [15] CMS Collaboration. CMS luminosity measurement for the 2017 data-taking period at  $\sqrt{s} = 13 \text{ TeV}$ . <https://cds.cern.ch/record/2621960>, 2018.
- [16] CMS Collaboration. Precision luminosity measurement in proton-proton collisions at  $\sqrt{s} = 13 \text{ TeV}$  in 2015 and 2016 at CMS. *European Physical Journal C*, 81(800) (2021), 2021.
- [17] CMS Collaboration. Performance of the CMS Level-1 trigger in proton-proton collisions at  $\sqrt{s} = 13 \text{ TeV}$ . *Journal of Instrumentation*, 15(P10017), 2020.
- [18] CMS Collaboration. The CMS trigger system. *Journal of Instrumentation*, 12(P01020), 2017.
- [19] CMS Collaboration. Electron and photon reconstruction and identification with the CMS experiment at the CERN LHC. *Journal of Instrumentation*, 16(P05014), 2021.
- [20] CMS Collaboration. Performance of the CMS muon detector and muon reconstruction with proton-proton collisions at  $\sqrt{s} = 13 \text{ TeV}$ . *Journal of Instrumentation*, 13(P06015), 2018.
- [21] CMS Collaboration. Description and performance of track and primary-vertex reconstruction with the CMS tracker. *Journal of Instrumentation*, 9(P10009), 2014.
- [22] CMS Collaboration. Particle-flow reconstruction and global event description with the CMS detector. *Journal of Instrumentation*, 12(P10003), 2017.
- [23] CMS Collaboration. Technical proposal for the phase-II upgrade of the CMS detector. <http://cds.cern.ch/record/2020886>, 2015.
- [24] Matteo Cacciari, Gavin P. Salam, and Gregory Soyez. The anti- $k_t$  jet clustering algorithm. *JHEP*, 04:063, 2008.
- [25] Vardan Khachatryan et al. Jet energy scale and resolution in the CMS experiment in pp collisions at 8 TeV. *JINST*, 12:P02014, 2017.
- [26] CMS JetMET POG. <https://twiki.cern.ch/twiki/bin/view/CMS/JECDATAmc>.
- [27] CMS JME POG. Jet identification for the 13 TeV UL data. <https://twiki.cern.ch/twiki/bin/view/CMS/JetID13TeVUL>.

- [28] CMS JME POG. Jet identification in high pile-up environment. <https://twiki.cern.ch/twiki/bin/viewauth/CMS/PileupJetID>.
- [29] A. M. Sirunyan et al. Identification of heavy-flavour jets with the CMS detector in pp collisions at 13 TeV. *JINST*, 13(05):P05011, 2018.
- [30] CMS Muon POG. [https://twiki.cern.ch/twiki/bin/view/CMS/SWGuideMuonIdRun2#Loose\\\_\\\_Muon](https://twiki.cern.ch/twiki/bin/view/CMS/SWGuideMuonIdRun2#Loose\_\_Muon).
- [31] CMS Muon POG. [https://twiki.cern.ch/twiki/bin/view/CMS/SWGuideMuonIdRun2#Tight\\\_\\\_Muon](https://twiki.cern.ch/twiki/bin/view/CMS/SWGuideMuonIdRun2#Tight\_\_Muon).
- [32] CMS Collaboration. Performance of the DeepTau algorithm for the discrimination of taus against jets, electron, and muons. CMS Physics Analysis Summary, CMS-DP-2019-033, 2019.
- [33] CMS Tau POG. [https://twiki.cern.ch/twiki/bin/view/CMS/TauIDRecommendation13TeV#Measurement\\_in\\_Z\\_tautau\\_events](https://twiki.cern.ch/twiki/bin/view/CMS/TauIDRecommendation13TeV#Measurement_in_Z_tautau_events).
- [34] Vardan Khachatryan et al. Performance of photon reconstruction and identification with the CMS detector in proton-proton collisions at  $\sqrt{s} = 8$  TeV. *JINST*, 10:P08010, 2015.
- [35] CMS EGamma POG. [https://twiki.cern.ch/twiki/bin/viewauth/CMS/CutBasedPhotonIdentificationRun2#SPRING15\\\_selections\\\_bunch\\\_crossi](https://twiki.cern.ch/twiki/bin/viewauth/CMS/CutBasedPhotonIdentificationRun2#SPRING15\_selections\_bunch\_crossi).
- [36] CMS Lumi POG. [https://twiki.cern.ch/twiki/bin/view/CMS/PileupJSONFileforData#Pileup\\_JSON\\_Files\\_For\\_Run\\_II](https://twiki.cern.ch/twiki/bin/view/CMS/PileupJSONFileforData#Pileup_JSON_Files_For_Run_II).
- [37] CMS Muon POG. <https://twiki.cern.ch/twiki/bin/view/CMS/MuonReferenceSelectionAndCalibrationsRun2>.
- [38] CMS JME POG. Reweighting recipe to emulate Level 1 ECAL prefiring. <https://twiki.cern.ch/twiki/bin/viewauth/CMS/L1ECALPrefiringWeightRecipe>.
- [39] Prefiring correction implementation in NanoAOD-Tools. <https://github.com/cms-nanoAOD/nanoAOD-tools/blob/master/python/postprocessing/modules/common/PrefireCorr.py>.
- [40] J. M. Lindert et al. Precise predictions for V+jets dark matter backgrounds. 2017.
- [41] Search for VBF Higgs boson decays to invisible particles with 2016 dataset, 2017. CMS Analysis Note : AN-17-267.

- [42] A Monte Carlo generator for the production of Higgs bosons attached to weak bosons (HAWK).
- [43] Albert M Sirunyan et al. Performance of missing transverse momentum reconstruction in proton-proton collisions at  $\sqrt{s} = 13$  TeV using the CMS detector. *Submitted to: JINST*, 2019.
- [44] Piergilio Lenzi, Christopher A. Palmer, Joshuha Thomas-Wilsker, et al. Performance of flavour tagging algorithms at 13 tev with 2018 data. CMS Note 2018/323, 2019.
- [45] Jon Butterworth et al. PDF4LHC recommendations for LHC Run II. *Journal of Physics G: Nuclear and Particle Physics*, 43(023001), 2016.
- [46] Vardan Khachatryan et al. Performance of the CMS missing transverse momentum reconstruction in pp data at  $\sqrt{s} = 8$  TeV. *JINST*, 10:P02006, 2015.
- [47] CMS JME. [https://twiki.cern.ch/twiki/bin/view/CMS/JECUncertaintySources#Run\\_2\\_reduced\\_set\\_of\\_uncertainty](https://twiki.cern.ch/twiki/bin/view/CMS/JECUncertaintySources#Run_2_reduced_set_of_uncertainty).
- [48] CMS Collaboration. Search for invisible decays of a Higgs boson produced through vector boson fusion in proton-proton collisions at  $\sqrt{s} = 13$  TeV. *Physics Letters B*, 793, 2019.
- [49] Albert M Sirunyan et al. Precision luminosity measurement in proton-proton collisions at  $\sqrt{s} = 13$  TeV in 2015 and 2016 at CMS. *Eur. Phys. J. C*, 81:800, 2021.
- [50] Thomas Junk. Confidence level computation for combining searches with small statistics. *Nucl. Instrum. Meth. A*, 434:435, 1999.
- [51] A. L. Read. Presentation of search results: the  $cl_s$  technique. *J. Phys. G*, 28:2693, 2002.
- [52] Abdelhak Djouadi, Oleg Lebedev, Yann Mambrini, and Jeremie Quevillon. Implications of LHC searches for Higgs–portal dark matter. *Phys. Lett. B*, 709:65, 2012.
- [53] Martin Hoferichter, Philipp Klos, Javier Menéndez, and Achim Schwenk. Improved limits for Higgs-portal dark matter from LHC searches. *Phys. Rev. Lett.*, 119:181803, 2017.
- [54] LHC Higgs Cross Section Working Group. Handbook of LHC Higgs cross sections: 3. Higgs properties. 2013.

# CURRICULUM VITAE

**ALP AKPINAR**